

**The Design of an Experimental Model for the 3D Characterization of Airflow
in Counterflow Cooling Towers**

by

Elizabeth Jane Clare

A thesis submitted in partial fulfillment of the requirements for the degree of

Master of Science

Department of Mechanical Engineering

University of Alberta

©Elizabeth Jane Clare, 2020

Abstract

The complexities and inherent 3D nature of airflow within cooling towers is often neglected in cooling tower analysis, and studies that attempt to investigate such air flow patterns are generally invalidated with regard to the 3D flows they attempt to simulate. This work outlines the design and construction of a lab-scale cooling tower model intended to collect airflow data in 3D for the purpose of investigating the complex flows generated by different features and components, both individually and collectively. Further, this lab-scale model is also capable of thermal and static pressure loss measurements traditionally utilized in 0D and 1D characterization of fill and other cooling tower components.

The data presented in this work focuses on the model's 3D airflow capabilities. A manually positioned pitot tube was used to measure the velocity and static pressure in 25-point arrays at a variety of cross-sections throughout the model cooling tower. These velocity and pressure maps were measured and plotted for the case of an empty tower including no fill, drift eliminator, nozzle, or water. Similar maps were plotted for the case of a full tower including fill, drift eliminator, and nozzle, but no water. In this same dry full-tower configuration, a 25-point pitot tube traverse was also performed across the two inlet faces to reveal the normal velocity and pressure profiles for the inflowing air.

Traverse measurements of velocity and pressure were used to measure the static pressure drop across the fill for a variety of air flow rates and fill heights. Relationships for fill losses were established, but varied from those reported by the manufacturer. Similar tests performed with the fill further away from the inlet yielded different pressure drop results across the fill, indicating that the interaction of various airflow-altering components is significant when the components are in close proximity. The static pressure drop across the drift elim-

inator was also measured, both in standard full-tower configuration and in an arrangement with fill above and below the drift eliminator so as to prevent the local recirculation evident above it in other configurations. Pressure drop measurements throughout the tower were collected under wet conditions using a static tap method rather than the pitot traverse, yielding a similar disagreement with manufacturer data as observed for the dry case. Velocity and pressure maps were plotted above the drift eliminator, illustrating the velocity profile in the plenum chamber.

Keywords: counterflow cooling tower, 3D airflow, static pressure, pressure loss, maldistribution, mechanical draft, fill, drift eliminator

Preface

This thesis is an original work by Elizabeth Clare. No part of this thesis has been previously published.

Acknowledgements

The work described in this thesis forms part of a larger ongoing research project regarding the design of cooling towers at the University of Alberta. I would like to acknowledge the contributions and support of:

- Dr. Marc Secanell and Dr. Morris Flynn for their guidance and support,
- my fellow graduate students for their helpful discussions and assistance,
- International Cooling Tower for their sponsorship of this project and valuable insights,
- the MECE shop technicians who built several sections of the experimental model and provided excellent advice,
- Facilities and Operations who built the fan-ductwork system and steam supply lines for the benefit of our model,
- Brentwood Industries for allowing me access to their detailed product information for comparison with my own results,
- Derrick and my family for their unwavering support, and
- Flapjack for always bringing me peace.

Table of Contents

1	Introduction	1
1.1	Motivation	1
1.2	Background	2
1.3	Types of Cooling Towers	4
1.4	Induced Draft Counterflow Cooling Towers and their Components	6
1.4.1	Fan	7
1.4.2	Drift Eliminators	7
1.4.3	Water Distribution	8
1.4.4	Fill	9
1.4.5	Rain Zone	10
1.4.6	Air Inlet	11
1.5	Maldistribution of Air	11
1.5.1	The Effect of Maldistribution of Air on Performance	11
1.5.2	Design Considerations for Maldistribution of Air	13
1.6	Literature Review	14
1.7	Objectives	16
2	Theory	18
2.1	Merkel Demand Curves	19
2.2	Merkel Supply Curves	25
2.3	Airflow and Static Pressure Loss in OD	26
3	Design of the Experimental Model	28
3.1	Cooling Tower	28
3.2	Water System	31
3.3	Steam Heating System	33
3.4	Air System	36
3.5	Sensors and Data Collection	36

4	Results	40
4.1	Validation of Airflow Readings	40
4.1.1	Pitot Tube Comparison	40
4.1.2	Pitot Tube Asymmetry	44
4.1.3	Differential Pressure Sensor Comparison	45
4.1.4	Sensitivity to Sampling Time	47
4.1.5	Repeatability	50
4.1.6	K-Factor for Averaging Pitot Tube	51
4.2	Velocity and Pressure Maps	56
4.2.1	Empty Tower Maps	56
4.2.2	Full Tower Maps	63
4.2.3	Inlet Maps	68
4.3	Static Pressure Drop	68
4.3.1	Fill	69
4.3.2	Drift Eliminator	74
4.3.3	Static Pressure Loss of Multiple Components	75
4.4	Wet Tower Tests	76
5	Conclusions	80
	References	82
	Appendices	87
A	Merkel Design Example	88
B	Water System Design	91
B.1	Design Objectives	91
B.2	Pump and Valve Selection	91
B.3	NPSH	96
B.4	Basin Drainage	97
B.5	Sump Pump System	99
B.6	Cleanliness	99
C	Steam System Design	100
C.1	System Overview	100
C.2	Component Selection	102
C.2.1	Valve Sizing	103
C.2.2	Steam Traps	106

C.2.3	Condensate Receiver and Pump	109
D	Instrumentation	110
D.1	Instruments	110
E	Error Analysis	112
E.1	Total Pressure	112
E.2	Air Density	113
E.3	Velocity	115
E.4	Static Pressure	116
E.4.1	Static Pressure Maps	116
E.4.2	Static Pressure Taps	117
E.5	Static Pressure Drop	117
E.6	Spatial Coordinates inside the Cooling Tower	118
E.7	Water Flow Rate	120

List of Tables

4.1	Sample deviation from 30 s case for varying sampling time, calculated using (4.3)	50
4.2	Empty tower flow rate and static pressure drop summary	63
4.3	Fill pressure loss constants	70
4.4	Static pressure drop summary for wet fill with two air speeds and two water flow rates	78
B.1	Estimated loss coefficients used for pump sizing	94
B.2	Summary of flow rates for globe valve closure represented by K_v	95
C.1	Effective lengths for steam line design	103
C.2	Mass contributed by different sizes of steam pipe	107
C.3	Surface area inside steam pipe	108
E.1	Summary of components of spatial error	119
E.2	Summary of spatial uncertainties	120

List of Figures

1.1	Schematic of a wet single-cell induced draft counterflow cooling tower	4
1.2	Schematic of a wet single-cell induced draft crossflow cooling tower . . .	5
1.3	Types of wet cooling towers - advantages and disadvantages	6
1.4	A section of Brentwood CF150MAx drift eliminator	8
1.5	Brentwood OF21MA fill - an example of modern low-fouling film fill	10
2.1	Temperature of water and air in a cooling tower	19
2.2	Enthalpy of saturated air film at air-water interface and bulk air in a cooling tower	20
2.3	Control volume for derivation of the Merkel number	21
2.4	Supply and demand Merkel number curves for Appendix A example	26
3.1	Lab-scale cooling tower model	29
3.2	Operating modes for water system	32
3.3	Steam heating system as installed	34
3.4	Steam heating system schematic	35
3.5	Air system schematic	37
3.6	Instruments used in the cooling tower test facility	38
3.7	LabView GUI for collection of sensor data	39
4.1	Traverse locations and their respective labels	41
4.2	5-point Location indices used in Figures 4.3, 4.4 and 4.7, and 25-point location indices used in 4.4, 4.5, and 4.6	42
4.3	Pitot tube and sensor comparison plotted with manufacturer-reported error .	42
4.4	Pitot tube comparison plotted with tested 95% confidence interval	43
4.5	Symmetry comparison of velocity measurements	44
4.6	Symmetry comparison of pressure measurements	45
4.7	Comparison of velocities measured with LMI and Fluke 922 differential pressure sensors	46

4.8	Noise recorded from LMI in velocity and total pressure readings at three locations	48
4.9	Deviation of differential pressure and velocity with respect to mean velocity .	49
4.10	Effect of varying sampling times for pitot tube measurements	49
4.11	Repeatability of pitot tube measurements	51
4.12	Disagreement between STRA and 160F using manufacturer equations	52
4.13	Dwyer STRA averaging pitot tube installed in experimental model	53
4.14	K -factor ($K = 0.628$) fit to experimental data	54
4.15	Fit of 0.628 K -factor to experimental data	55
4.16	Vertical velocity map in a 3D tower: empty tower, 60 Hz	58
4.17	Vertical velocity and static pressure map: empty tower, 60 Hz, $v_{av} = 2.7$ m/s	59
4.18	Vertical velocity and static pressure map: empty tower, 50 Hz, $v_{av} = 2.3$ m/s	60
4.19	Vertical velocity and static pressure map: empty tower, 40 Hz, $v_{av} = 1.8$ m/s	61
4.20	Vertical velocity and static pressure map: empty tower, 30 Hz, $v_{av} = 1.4$ m/s	62
4.21	Vertical velocity map in a 3D tower: full (dry) tower, 60 Hz, $v_{av} = 2.2$ m/s . .	64
4.22	Vertical velocity and static pressure map: full tower, 60 Hz, $v_{av} = 2.2$ m/s . .	65
4.23	Vertical velocity and static pressure map: full tower, 50 Hz, $v_{av} = 1.9$ m/s . .	66
4.24	Vertical velocity and static pressure map: full tower, 40 Hz, $v_{av} = 1.5$ m/s . .	66
4.25	Vertical velocity and static pressure map: full tower, 30 Hz, $v_{av} = 1.2$ m/s . .	67
4.26	Static pressure drop through a full, dry tower at varying air flow rates	67
4.27	Inlet normal velocity and static pressure map: full tower, 60 Hz	68
4.28	Static pressure drop versus air speed for various fill heights	70
4.29	Comparison of pressure drop across fills in standard case, raised case	71
4.30	Velocity maps in the rain zone plane for varying fill height.	73
4.31	Drift eliminator - static pressure drop	74
4.32	Wet tower static pressure taps for two air speeds and two water flow rates .	77
4.33	Vertical velocity and static pressure maps at plenum plane	79
A.1	Supply and demand Merkel number curves for Section A example	90
B.1	Schematic showing the equipment required to supply of hot water to the tower.	92
B.2	Basin and sump system	98
C.1	Steam system sketch: Steam and condensate arrangement	101
C.2	Steam system sketch: Condensate recycle and drain arrangement	101
E.1	Coordinate system for analysis of spatial errors	118
E.2	Uncertainty in spatial error for individual traverse points (mm)	121

List of Symbols

Symbols

A	area, m ² , or approach, °C or K
a	wetted area per unit volume, m ⁻¹
C	an empirical constant, units vary
c_p	specific heat capacity at constant pressure, J/(kg K)
G	air load per unit area, kg/(m ² s)
g	gravitational acceleration, m/s ²
H	height, m
h	transfer coefficient, W/(m ² K) for heat, kg/(m ² s) for mass
i	enthalpy, J/kg
K	dynamic pressure coefficient (dimensionless)
L	water load per unit area, kg/(m ² s)
Le_f	Lewis factor, ratio of heat transfer to mass transfer (dimensionless)
Me	Merkel number (dimensionless)
m	mass flow rate, kg/s
P	pressure, Pa (kPa or psi when indicated)
Q	heat, J
\dot{Q}	rate of heat flow or power, kW
R_p	pressure ratio (system pressure loss: air inlet dynamic pressure)
s	sample deviation
T	temperature, °C or K
v	velocity (of air), m/s
w	humidity, kg/kg
z	vertical distance, m
Δ	a difference
δ	an uncertainty or error
ρ	density, kg/m ³

Subscripts

<i>a</i>	dry air
<i>av</i>	air-vapour mixture (damp air)
<i>c</i>	convective
<i>db</i>	dry bulb temperature
<i>fg</i>	enthalpy difference between liquid and vapour states
<i>fi</i>	fill
<i>i</i>	inlet
<i>m</i>	mass transfer
<i>o</i>	outlet
<i>p</i>	constant pressure or pitot tube
<i>s</i>	saturated air and vapour mixture or static pressure
<i>v</i>	vapour
<i>w</i>	liquid water
<i>wb</i>	wet bulb temperature

Chapter 1

Introduction

1.1 Motivation

In a wide variety of industrial applications, low-grade heat becomes a waste product to be disposed of at the end of the process. Cooling towers were developed as a means to meet this demand for effective, economical, and compact removal of waste heat.

Cooling towers are by no means a new technology - in fact, their use and study began at the turn of the 20th century alongside the first steam-powered electric stations [1]. In assessing and designing cooling towers, it has been industry practice for many years to treat the cooling tower as a black box having a certain cooling performance, quantified by a dimensionless number known as the Merkel number, which is defined in Chapter 2. The underlying methodology was first proposed by Merkel in 1925 [2], but it was translated, refined, and popularized by others years later [1]. Present-day cooling tower design uses the same basis, although modifications and enhancements have been added for additional accuracy or expanded functionality.

Despite its wide acceptance throughout industry, this method of analysis fails to capture the complexity of the physics that govern the transport processes within a cooling tower and does not provide any information regarding the local fluidic, thermodynamic, and psychrometric properties inside the tower. Therefore, even though predicting the performance of a previously-tested configuration is well within the ability of the Merkel method, this 0D method is of little assistance in the development of new configurations and addressing design problems dealing with inherently 2D and 3D phenomena such as flow maldistribution.

Computational fluid dynamics (CFD) tools are more suited to the task of representing these complex flows. Due to the wide range of physical scales that govern the operation of a cooling tower, the thermal performance and airflow resistance of the fill section is generally represented by a 0D or 1D model, even when a 2D or 3D CFD simulation is used to model the flows outside the fill. Unfortunately, there is a lack of experimental data taken in three

dimensions from inside cooling towers with which to validate CFD models used for this purpose.

As a result, to support the development of simulation and design tools for cooling towers at the University of Alberta, the objective of this work is the design and construction of a lab-scale cooling tower from which to take measurements suitable for both “black box” 0D/1D fill performance analysis and for 2D/3D CFD model validation with an emphasis on the resolution of the internal air flow field.

1.2 Background

Rejection of low-grade heat to the environment is a necessity for any power or refrigeration cycle, and the efficiencies of these processes are improved by maintaining a lower discharge temperature. Waste heat removal is likewise required in metallurgical plants, plastic moulding facilities, internal combustion engine applications, and chemical plants or refineries.

The first solution developed for industrial-scale cooling was the use of water from a local river, dam, or ocean as a cooling medium. In such once-through systems, the water is returned back to its original source after taking up the waste heat. This method therefore requires the plant to be built nearby a suitable water source, and in recent times there has been a shortage of such sites. Though not appreciated initially, the once-through approach is also often unsuitable due to the impact of heat pollution on the ecology of the water body, and government regulations have since been put in place to prevent such damage. Once-through cooling has therefore become less common in newly-built facilities.

A solution for locations having no suitable body of water nearby was also developed; a large man-made pond could be created for the circulating water. This pond would cool over time as the combined action of evaporative, convective, and radiative heat transfer dissipated heat into the environment. Cooling ponds are still in use today as a cheap and simple method of cooling, but they are not always suitable because of the large areas required for the ponds, on the scale of 5000 to 15,000 m² per megawatt of installed capacity [3].

To improve upon this approach and lessen the associated footprint, spray systems were added to the cooling ponds; these allow the hot water to cool significantly as a spray of droplets before reaching the pond. Spray systems improve the efficacy of the ponds, allowing spray ponds to utilize a smaller footprint than the standard cooling pond. Spray ponds are still in use today in certain applications. However, the performance of such systems varies with local weather conditions, and they are limited in terms of temperature control, approach (cold water temperature minus ambient wet bulb temperature), compactness, and reliable wintertime operation [4]. Furthermore, the spray can be blown away from the pond by wind, rendering the surrounding area unsuitable for other purposes [5], particularly if the water is

brackish or contains trace chemicals such as rust inhibitors.

By confining the spray to an enclosed structure, adding packing media to slow water flow and maximize air-water interfacial area, and including a fan or tall stack to achieve consistent flow of air regardless of local wind patterns, great improvements were made in thermal efficiency, weather-independent operation, and footprint. These advances ultimately lead to the technology known today as wet or evaporative cooling towers [5, 6].

As the first cooling towers were built, attempts were made (with varying degrees of success) to develop a sound model for cooling tower theory by which to predict performance. The researchers of cooling tower industry and academia were relatively unaware of each others' respective practices, and for many years cooling tower manufacturers used their own empirical rating charts with no theoretical basis. Rather than calculating a fill height required for a certain performance, cooling towers were manufactured in predefined sizes and arrangements, and the water and air loading were varied according to empirical charts and relations to achieve the design cooling load [1].

Merkel developed the first theory based on enthalpy potential as a driving force, effectively combining the effects of mass and energy transfer [2]. This clever solution was a vast improvement over the theories proposed previously. Unfortunately, he suffered an untimely death shortly after the publication of his cooling tower theory, and the theory went largely unnoticed outside of Germany until it was rediscovered by Nottage in 1938. The theory was adapted and translated for the American Society of Heating and Ventilating Engineers Guide in 1941 [1]. Thereafter, the Merkel theory was adopted by the cooling tower industry, and is still the most common method of cooling tower design and analysis used today.

In using this method to design a cooling tower, each relevant component of the tower is characterized with respect to the Merkel number and to airflow resistance. These individual effects can thereafter be combined to produce a design that achieves the desired cooling with a specific water loading and air flow rate, or with a specific height of fill, fill serving as the primary heat exchange medium. (See Chapter 2 for an in-depth derivation of the Merkel equations, and see Appendix A for an example in which fill height is determined.) Using Merkel's method can provide useful results in terms of fill quantity and air and water loading, but Merkel's equations are of limited usefulness in examining the 3D effects within a cooling tower, such as nozzle selection and arrangement, support structure, internal baffles, and maldistribution of water and air. Section 1.5 discusses the importance of 3D airflow phenomena in greater detail.

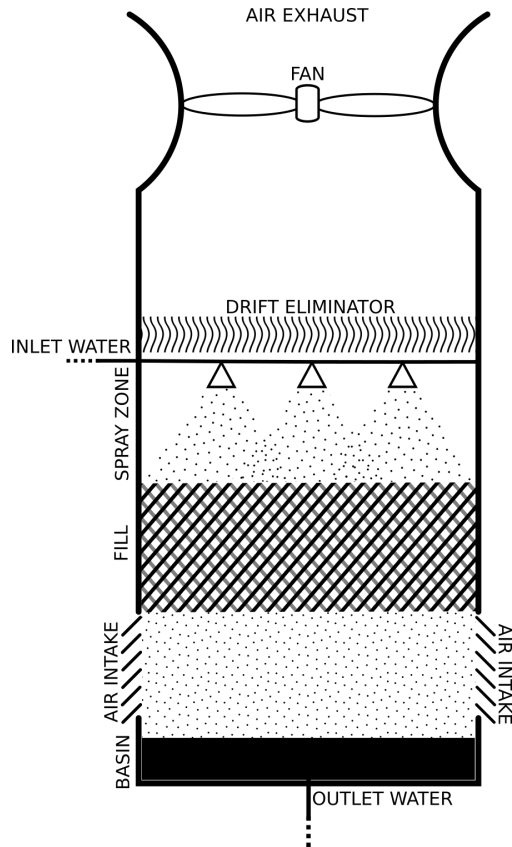


Figure 1.1 – Schematic of a wet single-cell induced draft counterflow cooling tower

1.3 Types of Cooling Towers

In order to facilitate the desired rejection of waste heat to the environment, most modern cooling towers follow the same fundamental design. The hot water enters the tower, and is sprayed over a fill, ultimately collecting in a basin at the tower base. Counter- or cross-flowing air is introduced into the tower through the bottom or sides, flowing through the wetted fill and removing heat and water vapour from the descending water. Counterflow towers have air inlets placed below the fill such that air flows through the fill vertically as shown in Figure 1.1. Crossflow towers are built so that the inflowing air comes in through the sides of the tower, flowing horizontally through the fill to the center of the tower as shown in Figure 1.2. In both cooling tower types, the air is ultimately discharged through the top of the tower, often resulting in a visible plume as vapour from the damp, warm exhaust air condenses in the cooler ambient air. A variety of additions and modifications can be made to these basic designs in order to meet various design goals for a cooling tower. The most advantageous cooling tower design for a certain application depends upon a long list of factors, including water load, heat load, area and height requirements, capital costs, operating costs, regulatory requirements, availability and cost of make-up water, availability

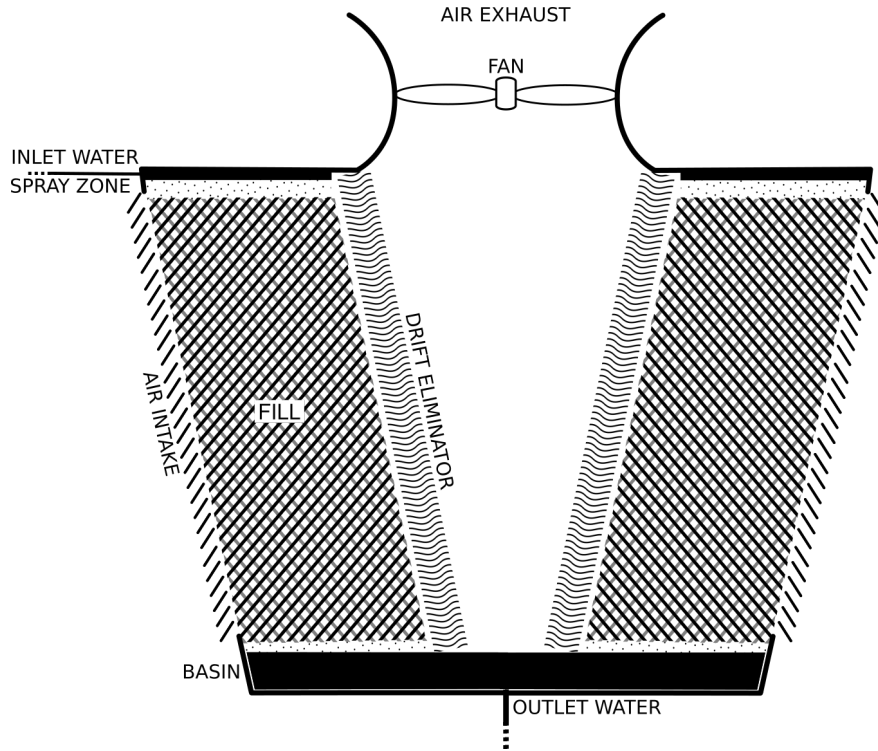


Figure 1.2 – Schematic of a wet single-cell induced draft crossflow cooling tower

and cost of disposing of blowdown water, local weather patterns, tendency for recirculation, and the icing, visibility and aesthetic implications of the plume.

The iconic hyperbolic cooling tower is a natural draft cooling tower - one whose airflow is induced by buoyancy alone. Mechanical draft cooling towers, by contrast, use one or more fans to drive air flow. These fans can be installed so as to either blow air into the inlet side (forced draft) or to pull air up through the tower from the outlet by suction (induced draft). Both natural and mechanical draft towers can have their fill media arranged in either counterflow or crossflow configurations. Multiple cooling tower “cells” can be built together as a single unit to cool greater heat or water loads.

Each arrangement has its own strengths and weaknesses, and is suited for different applications. Figure 1.3 summarizes the major advantages and disadvantages of each of the discussed tower types [6–8]. Dry cooling towers and hybrid dry/wet cooling towers also exist, but will not be addressed in this work. Cooling tower placement, orientation, and the arrangement of cooling tower cells in multi-cell towers will likewise not be addressed here.

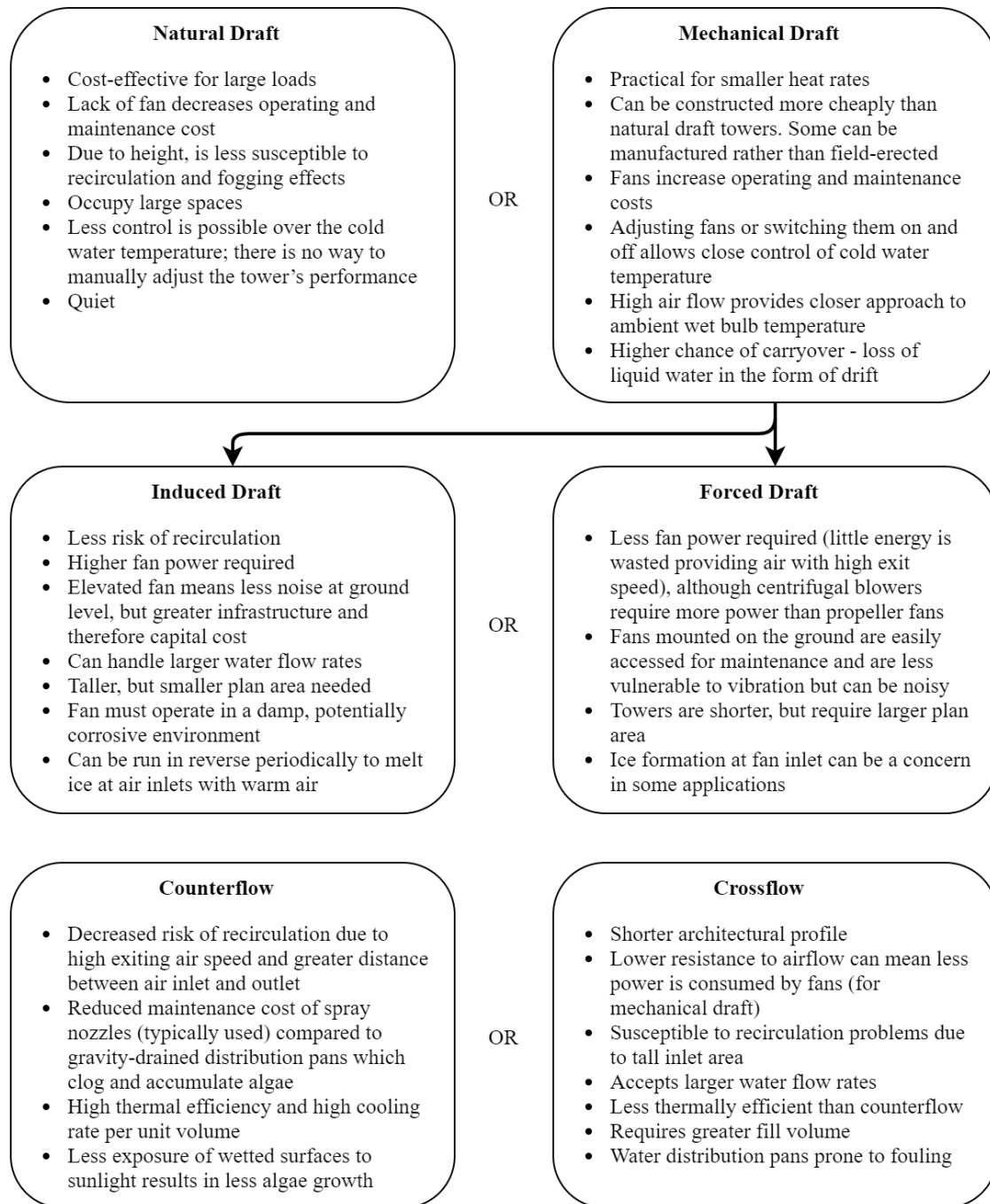


Figure 1.3 – Types of wet cooling towers - advantages and disadvantages

1.4 Induced Draft Counterflow Cooling Towers and their Components

This thesis will focus specifically on counterflow induced draft wet cooling towers. These towers achieve the best performance in terms of approach of the cold water temperature to

the air wet bulb temperature. This is due to the advantageous counterflow layout in which the hottest water comes into contact with the warmest air and the coolest water comes into contact with the coolest air (as shown in Figure 1.1). This thermal advantage combined with a resistance to exterior recirculation effects make induced draft counterflow towers the most efficient cooling towers available in terms of cooling achieved per unit volume of the tower. The use of fans to increase airflow allows for improved heat and mass transfer, enabling closer approaches; this can be a valuable advantage, especially in warm or humid climates. Today, induced draft cooling towers are employed more often than forced draft towers [9], and are used in applications as small as 15 gpm and as large as 700,000 gpm [10].

The basic components of an induced draft counterflow cooling tower are the fan, drift eliminator, water distribution system, fill, rain zone, air inlet, and basin, illustrated in Figure 1.1. Each of these components is described briefly below in Sections 1.4.1 through 1.4.6.

1.4.1 Fan

Mechanical draft cooling tower designs make use of fans to drive airflow. Induced draft towers include a fan at the air outlet, drawing the air up through the tower by suction. Such fans can be more difficult to maintain, and must be able to operate reliably in consistently damp conditions, but the high speed at which the exhaust air travels from the exit leads to reduced risk of recirculation [10]. Recirculation occurs when the warm, damp air exiting the cooling tower is drawn back to the air intake. Because a cooling tower's performance is dependent upon the wet bulb temperature of the entering air, cooling performance can suffer dramatically in this situation [10].

Either axial or centrifugal fans can be used in induced draft cooling towers, although propeller-type axial-flow fans are most common for reasons of cost and availability [9]. Fans are also selected for noise, static pressure, or energy usage design needs [4]. Large propeller fans are often made with variable-pitch blades for adjustable airflow. On/off cycling, two-speed motors, and variable frequency drives may also be used to control airflow and, by extension, the rate of heat removal from the process water.

1.4.2 Drift Eliminators

As the warm, damp air exits through the top of the tower, small liquid water droplets can become entrained in the airflow; these liquid droplets are often referred to as carryover or drift. If this drift escapes into the atmosphere, several problems can arise:

1. Water is lost in excess of that needed to achieve cooling, leading to increased makeup water requirements for the cooling tower,



Figure 1.4 – A section of Brentwood CF150MAx drift eliminator

2. Chemical additives [10] and salt [11] can be released, contaminating the surrounding environment, and
3. Bacteria which tend to propagate in the warm, humid environment inside a cooling tower can be released into the outside air, leading to potentially deadly illness such as Legionellosis [12].

Therefore, it is necessary to remove drift from the exhaust air stream. This is often done with a drift eliminator, which causes the exiting air to make sudden changes in direction two or more times [10]. Instead of following the air flow through these sudden turns, droplets larger than a certain size are forced by inertia to impact the walls of the drift eliminator, ultimately dripping back down onto the fill. These devices are installed downstream (in terms of airflow) of the spray zone, as shown in Figure 1.1.

Drift eliminators are ideally designed to remove the maximum quantity of drift while creating a minimal pressure drop for the fan to overcome. These two design goals are at odds, but compromises have been struck in a variety of designs. Modern cooling towers incorporating drift eliminators have very low drift rates, seldom exceeding 0.008% for small towers and typically meeting 0.001% of the circulating water rate for large towers [10].

1.4.3 Water Distribution

Different varieties of fill are designed to be used with different water loads. A water load that is too low results in poor water distribution over the fill, while a water load that is too high will flood the fill and impede the flow of air. Ideally the water distribution system is designed to spread the hot water evenly over the fill, while requiring the least amount of pumping head. In the case of maldistribution, flooded areas underperform due to lessened

evaporation, while areas that are too dry underperform (in spite of lower water temperatures achieved there) [1, 13]. A small amount of maldistribution will not significantly alter a tower's performance, but greater non-uniformities have a notable effect [14].

Gravity-fed water distribution systems are most common with crossflow towers. Such systems use a hot water distribution basin placed above the fill. These can be built as a system of troughs, perforated pipes, or perforated pans [9]. Gravity-fed water systems are more easily inspected and maintained, but do not generally contribute significantly to heat transfer and can become clogged with algae if the hot water basin is not covered [10].

Counterflow towers, by contrast, are usually built with an array of spray nozzles. These nozzles create sprays of various geometries, and are selected and arranged so as to distribute water evenly across the entire fill cross section. Up to 15% of cooling can occur in the spray zone, before the water even enters the fill [15]. Spray nozzle systems contribute to heat transfer, and are not prone to algae formation, but are more difficult to maintain and require higher pumping heads [10].

1.4.4 Fill

The fill is a medium installed into a cooling tower to achieve two effects: a) increase the residence time of the water, and b) increase the area of the air-water interface. This way, the fill accomplishes up to 90% of the total cooling in the tower [16]. The two main varieties are splash and film fill.

Splash fill breaks the descending water down into small droplets as they impact an array of splash bars which can be made in various geometries. This fill type has the advantage of being insensitive to fouling and producing a smaller static pressure drop, which can reduce the fan power needed to drive airflow. Splash fill is also less sensitive to air and water maldistribution [4, 17]. Water loading per unit volume must be kept moderately low when using splash fill, which means that larger towers are needed to house them, and larger pumps are needed to reach the increased height. Splash fill also tends to produce more carryover, requiring more stringent drift removal measures [15]. Materials such as treated wood lath, fiber-reinforced plastic, PVC coated wire grids, polypropylene, PVC, stainless steel, or aluminum are typically used as splash bars [10].

When using film fill, the descending water flows over the fill in a thin layer. Typically, the fill is made out of thin sheets of PVC plastic [3, 4, 10], although a film flow regime has also been achieved with other types of plastic, asbestos sheeting, grids of timber slats, resin impregnated cardboard, metal, or ceramics [9, 15]. Film-type fill has the advantage of higher cooling efficiency per unit of fill volume, but it is generally more vulnerable to performance loss due to maldistribution of water and air [10, 15, 17]. Film fills generally



Figure 1.5 – Brentwood OF21MA fill - an example of modern low-fouling film fill

suffer performance degradation from fouling - silt, scale, algae, and slime can build up on the fill's surface, restricting the free area through which air and water can flow freely [10, 15]. Manufacturers have also created film fill designs which are less sensitive to the effects of fouling. These anti-fouling fills are designed to encourage higher velocity (and therefore shear stress) in the water film, preventing buildup from accumulating on the fill walls. This usually means allowing the water to flow down through vertical channels.

Spray towers operate with no fill at all. These are used where the exiting water temperature is high, and where fouling effects are too extreme to consider the use of a fill [10].

1.4.5 Rain Zone

When considering a counterflow cooling tower, after the water passes through the fill, the water drops down into the basin below. Between the fill and the basin there is an area where this water falls as droplets (or jets), interacting with the inlet air. This region is commonly called the rain zone, and is often responsible for 10-20% of overall heat transfer [15]. Splash fills result in rain zone droplets with a Sauter mean diameter of 3 to 4 mm, while a film fill produces droplets of 5 to 6 mm [15], the Sauter mean diameter being the diameter of a drop with the same ratio of volume to surface area as the entire spray.

1.4.6 Air Inlet

The inlet to the cooling tower could be located on one, two, three, or all four faces of the tower, depending on the placement of the tower relative to external obstructions [4]. The inlet area is designed to maintain a desired average velocity. Louvers are placed at the air inlets to direct air into the tower and encourage even air distribution through the fill [3], while simultaneously preventing circulating water from escaping the tower, especially when using splash fill or for a crossflow tower [10]. Louvers can also be adjusted so as to be more open or more closed, introducing another means to control airflow. Air dams or air inlet guides are also included on some cooling towers; these appear as a small fin around the top outer edge of the air inlet. These air dams prevent regions of stagnant, recirculating air in the rain zone [17, 18], but have not been widely investigated in academic literature.

1.5 Maldistribution of Air

1.5.1 The Effect of Maldistribution of Air on Performance

Although cooling tower design is generally performed using the 0D approach explained in Sections 2.1 and 2.2, cooling towers include various features which result in 3D flow phenomena which can have a significant and adverse effect on cooling performance. The Merkel method and other related methods assume that water and air are evenly distributed throughout the cross-section of the cooling tower at all times. When these distributions are made nonuniform, overall cooling performance decreases even if, locally and in select areas, enhanced heat transfer may result.

A simplified example from Baker [1] will be used to demonstrate the effect of uneven air distribution. While operating conditions and air flow remain constant, approach is generally proportional to the mass flow rate of water, i.e.,

$$A \propto L, \tag{1.1}$$

where A is the approach, i.e., the difference between water outlet temperature and air inlet wet bulb temperature, and L is the water loading per unit area. At a water loading of 100% of the design water loading, the approach is 100% of the design approach. If the water loading increases by 20% in half of the tower and decreases by 20% in the other half, the approach would likewise increase 20% and decrease 20% in the overloaded and underloaded halves, respectively. The approach of the entire tower could be found by averaging the approach weighted by the mass flow rate of water, i.e.,

$$\frac{120\% \text{ flow} \times 120\% \text{ approach} + 80\% \text{ flow} \times 80\% \text{ approach}}{200\% \text{ flow}} = 104\% \text{ approach.}$$

Although performance increases in the underloaded section and decreases in the overloaded section, the two effects do not cancel out entirely, and the result is an increase in approach: a degradation of cooling performance.

In considering possible maldistributions of air, Baker [1] asserts that at constant operating conditions, to maintain constant cooling performance, the mass flow rates of water and air must be maintained at the ratio

$$L \propto G^n, \quad (1.2)$$

where n varies between 0.9 and 1.1 but is 0.93 on average, and can be determined experimentally. A value of 0.93 will be used in this example. Instead of varying water loading by 20% in two halves of the cooling tower, air flow will be varied by 20%. In an area which has 20% too much air, water flow would have to be increased by 18.5% to maintain constant performance ($1.20^{0.93} = 1.185$). However, water flow is not being increased to match the air flow, so the water flow can be considered to be $100\%/118.5\% = 84.4\%$ of what it should be to maintain constant performance. Therefore, the approach in this region will be 15.6% lower than the design approach, and in the region with 20% less air the approach will be 23.1% higher. Averaged by water mass flow rate, this yields an overall approach of 104%, very similar to that obtained when varying water loading by the same extent.

However, the analysis above is not entirely correct because it does not take into account that the fan will always be operating at a constant power output, and that power varies with the cube of the air flow rate:

$$\frac{1.20^3 + 0.80^3}{2} = 112\% \text{ power.}$$

To keep fan power constant while the air flow rate is varied by 20% in the two sections, the air flow rates can be solved using

$$\frac{G_1^3 + G_2^3}{2} = 100\%, \quad (1.3)$$

where G_1 and G_2 are the normalized high and low air loadings, respectively. Because G_1 is 120% of the design value and G_2 is 80%, the two flow rates must relate by

$$G_1 = 1.5G_2. \quad (1.4)$$

From this system of two equations, the air flow rates are found to be 115% in the overloaded region and 77% in the underloaded region, resulting in an overall air flow rate of 96% of the original design value. This demonstrates one of the problems of air maldistribution - when distribution is poor, a lesser air flow rate is achieved overall, and less air is available for heat exchange.

Because no relationship for approach with respect to air loading is provided, air loading must again be converted to equivalent to water flow rates, (i.e., treating a lack of airflow as an overloading of water and an overloading of air as a lack of water). Using (1.2), it can be shown that an air flow rate of 77% corresponds to a water flow rate of 78.4% to maintain constant performance in that area of the cooling tower, but the water flow rate is not being adjusted to suit the air flow, so this region of lessened airflow is treated instead as being overloaded with water by 27.5% ($100\%/78.4\% = 127.5\%$). Likewise, an air flow rate of 115% should be matched by a water flow rate of 113.9% to maintain constant performance, but the true water flow rate will be 87.8% of that ($100\%/113.9\% = 87.8\%$). Using (1.1), these water loadings correspond to approaches of 127.5% and 87.8% respectively, and when weighed by mass flow rate of water, the overall approach is determined:

$$\frac{100\% \text{ flow} \times 127.5\% \text{ approach} + 100\% \text{ flow} \times 87.8\% \text{ approach}}{200\% \text{ flow}} = 108\% \text{ approach.}$$

In this admittedly simple example, the effect of maldistribution of air on the cooling tower’s approach is demonstrated to be double that of water. The decreases in overall air flow rate and cooling performance are also shown to be a consequence of poor air distribution, despite local increases in select regions of the tower.

1.5.2 Design Considerations for Maldistribution of Air

Film fills only allow for redistribution of air (and water) parallel to the fill sheets, and so are more vulnerable to the effects of maldistribution than splash fills. Furthermore, film fills are shorter and more dense than splash fill, so air and water have less travel time and less opportunity to equalize as they pass through the tower [17]. Maldistribution of air is addressed in cooling tower design by considering the following factors:

- Depending on the geometry of the inlet area, significant areas of stagnant, recirculating air can form inside the tower immediately adjacent to the inlet’s top edge. If these stagnant air zones penetrate into the fill, these portions of the fill will accomplish little or no cooling [17]. The inlet geometry can be altered to decrease the size of these stagnant zones, e.g. by application of air dams which allow air to enter the inlet at an angle closer to the horizontal [17, 18].
- Wakes formed downstream of structural elements in the area of the air inlet can cast a “shadow” over large areas of fill, decreasing air flow in those regions and hampering cooling [17]. These should be avoided wherever possible.

- To further improve distribution of air in the rain zone, air flow vanes or flow straighteners can be strategically placed so as to direct air smoothly and evenly into the fill above [19, 20].
- An increase in pressure ratio, i.e., the ratio of system pressure drop to velocity pressure at the average inlet velocity, encourages the entering air to spread out evenly as it enters the fill. A pressure ratio of 5 or more is recommended by the Cooling Tower Institute [17, 18].
- Poor distribution of air flow can also occur in the fill if the fan cylinder is too small or if the plenum chamber itself is too short. Rules of thumb or more complex empirical relationships are used to size these elements appropriately [17].

The traditional Merkel method of analysis does not take such factors into account. Often, to address air distribution, industry rules of thumb are used to arrive at designs which will yield reasonable performance. An alternative approach is to implement a decrease in “effective area” in fill regions partially blocked with stagnant air as part of a Merkel analysis [18]. Additionally, CFD simulations can be used to examine the implications of different cooling tower designs on air distribution. Experimental data specific to airflow inside a cooling tower is very sparse - to improve upon any of these methods, further experimental data regarding both air flow and cooling performance are required. Whereas providing data to this effect is the major goal of this thesis, it is necessary, before summarizing the research methodology, to first highlight key foundational studies (experimental or numerical). These studies are briefly reviewed in the following section.

1.6 Literature Review

Although this work is an experimental investigation of airflow inside a cooling tower, the majority of studies regarding the effect of various geometrical features on the behaviour of airflow inside cooling towers have been conducted using CFD. Lindahl and Bugler [17] used FLUENT to study the effect of air inlet guides on the streamlines of incoming air with special attention to internal recirculation zones. In that paper, they also investigated the effect of pressure ratio on the uniformity of air distribution. Although they mention accompanying physical experiments, few details are provided regarding the model or procedure that were used. Milosavljevic and Heikkilä [19] conducted simulations in Fluent/UNS to assess the effect of inlet geometry of a forced draft cooling tower on the distribution of air over the fill, using various distances between the diffuser and the fill and, for two tests, a flow straightener and a bell-shaped air spreader. Physical experiments were performed to characterize fill

performance using a 1D model, but not to validate the CFD results. Klimanek et al. [20] used Fluent to assess the distribution of air across the fill of a mechanical draft cooling tower including turning vanes in the rain zone. Further, ANSYS workbench was used to adjust the placement of the vanes to optimize the distribution of air. Klimanek et al. [20] did not go so far as to confirm whether this distribution of vanes would lead to optimal thermal performance or to verify the results experimentally. Reuter and Kröger [18] used Fluent to investigate the effect of inlet geometry on the flow patterns, loss coefficients, and effective flow diameter in circular natural draft cooling towers. These results were compared against velocity profiles, loss coefficients, and effective flow diameters from experiments. The model was then used to investigate particular variables of inlet geometry and establish relationships for their resulting effects.

Despite the typical practice of validating CFD simulations against many data points and parameters, Klimanek [21] observed that CFD simulations of cooling towers are typically only validated against 0D performance metrics such as cold water temperature. Indeed, Majumdar et al.'s CFD model (VERA2D) [22], Benton and Waldrop's quasi-2D model [23], Hawlader and Liu's 2D model [24], Williamson et al.'s axisymmetric model [25], and even Klimanek et al.'s axisymmetric model [16] were all validated against either the outlet water temperature or the range (total water temperature drop) measured from field tests of full-scale cooling towers. Some CFD models have not been validated against experimental data at all; for example, Al-Waked and Behnia presented a 3D CFD model and compared its results against the design conditions of a proposed natural draft cooling tower [26].

The only validation of a CFD simulation of a cooling tower against multiple points in 3D space seems to be that of Reuter and Kröger [18]. This model in ANSYS Fluent was compared against data from an experimental model of a sector of a cooling tower in a wind tunnel, including pitot tube-anemometer readings across the (air-wise) downstream side of the fill. The fill was represented by plate-finned radiator cores sandwiched with perforated plates. Static pressure downstream of the fill was measured with a static pressure tap in the "shell" wall coupled with a manometer relative to atmosphere. Inlet geometry could be freely altered, including the shape of inlet edges (rounded or square) and inlet height. This experimental model was meant specifically for characterizing inlet airflow effects; it was not built to investigate other sections of a cooling tower, nor was it built for use with water. Oosthuizen [27] provides additional information on this experimental model. The fill resistance to airflow was adjusted by installing different combinations of heat exchanger and perforated plates. He also described an alternative configuration for this same model to represent rectangular cooling towers. The effective area experiments were performed visually by introducing a string into the flow field and observing where circulating air was present through the transparent wall of the experimental model.

To consider thermal and water effects, the capabilities of a standard fill performance test must be added. To date, many experimental investigations of cooling towers have been performed specifically for the purpose of determining Merkel number and pressure drop relationships for various fill designs, meant for use with 0D/1D design and analysis. Lowe and Christie [28], Cale [7], Fulkerson [29] and Bell et al. [30] each characterized numerous fill configurations, measuring water flow rate, air flow rate, inlet air psychrometrics, outlet air wet bulb temperature, inlet and outlet water temperature, and pressure drop across the fill (although Fulkerson chose not to measure outlet air properties and EPRI managed to measure dry bulb temperature at the outlet).

In sum, the literature lacks experimental data from a cooling tower facility which can capture these 3D airflow effects as well as the impact on thermal performance once heat and water are introduced. Therefore, this work aims at beginning to fill that void by developing a cooling tower testing facility to measure airflow distributions and thermal performance, focusing especially on resolving the air flow field inside a cooling tower. Taking cues from the model used by Reuter, Kröger [18], and Oosthuizen [27], the experimental model described in this thesis utilizes a manually positioned pitot tube to capture the velocity of air at multiple points. This new model seems to be the first case in which air velocity and pressure are measured at multiple locations within a cooling tower including multiple components, allowing for not only the study of airflow patterns and pressure losses generated by these components individually, but also their interaction. These data could be used to complement and validate CFD simulations meant to study the airflow, pressure drop, and performance effects of particular cooling tower features and geometries. In addition, measured inlet and outlet conditions for air and water could be used to complement the 3D airflow data by demonstrating the effect of airflow-altering features on cooling performance.

1.7 Objectives

In order to enable the creation and verification of 3D simulation and design tools for cooling towers, my work aims to design and build a functional lab-scale induced draft counterflow cooling tower. Performance data from this apparatus should be used to corroborate analysis tools, from the 0D Merkel method and its 1D derivatives, to detailed CFD simulations to be performed by other students as part of the current research initiative. The experimental facility will be designed to allow for the collection of airflow and pressure data from the tower interior. This will provide insight into the 3D air flow phenomena within induced draft counterflow cooling towers, and will further provide a valuable source of validation data for CFD simulations. To this end, the objectives of this work are as follows:

1. Design a laboratory-scale cooling tower test facility capable of representing a typical

range of heat, air, and water loading for a full-scale induced draft counterflow cooling tower, and the measurement tools for the collection of airflow and pressure data in 3D space.

2. Construct said cooling tower facility, complete with tower, water supply, air supply, heat supply, and instrumentation.
3. Calibrate and analyse the uncertainty in the selected sensors.
4. Perform experiments to measure air flow and pressure drop inside the cooling tower at locations of interest for a dry cooling tower and its components, analysing the observed phenomena.
5. Perform experiments to measure pressure drop for a wet cooling tower under various loading conditions, analysing the effect of water loading on pressure drop.

Chapter 2

Theory

The most common and efficient type of cooling tower, a wet cooling tower, makes use of both latent and sensible heat transfer between the circulating water and the ambient air [9]. The advantage of a wet cooling tower over an air-cooled heat exchanger is its ability to exploit evaporative cooling instead of simply relying on the temperature difference between two media.

A portion of the hot liquid water is evaporated, taking up energy from the remaining liquid water and cooling it significantly. This effect can be used to enhance cooling so long as the moisture content of the air is less than saturated at the temperature of the water [15]; even saturated ambient air is still capable of accepting additional moisture if it is warmed by exposure to hot water. The amount of water that is lost by evaporation is small relative to the total water flow rate, but depends upon operating conditions. Typical losses are approximately 1 to 3% of the flow rate of the circulating water [15], or 1% for every 7 K of range (water temperature drop) [4]. In addition to this latent heat loss, the physical contact between the circulating water and ambient air also provides the opportunity for sensible heat transfer to occur. Latent heat transfer dominates in a typical cooling tower, although the exact ratio of latent to sensible heat transfer depends on the operating conditions.

As air and water move through the tower, their respective temperatures can be visualized on a graph such as Figure 2.1. Intuitively, the water cools and the air heats up as they move through the tower and interact with one another. The difference in temperature between the cooled outlet water and the inlet air (wet-bulb) is often referred to as the approach. The approach depends upon the ambient air wet bulb temperature (which varies by season and time of day) and the required cold water temperature. A larger or more efficient tower can achieve a narrower (better) approach, bringing the cold water temperature very close to the inlet air wet bulb temperature. The total temperature drop experienced by the water in the tower is called the range. A cooling tower will be designed for a certain range depending upon the needs of the application.

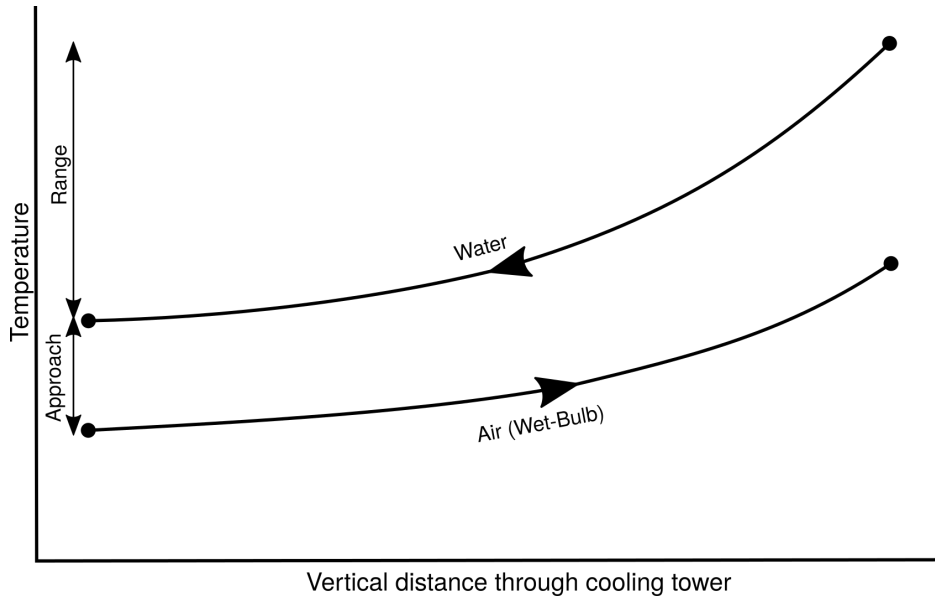


Figure 2.1 – Temperature of water and air in a cooling tower
Adapted from ASHRAE [4]

The same cooling tower installed in two different climates will not be able to accomplish the same amount of heat rejection in both. Higher ambient wet-bulb temperatures are of more concern because cooling is more difficult to achieve in these conditions. Therefore, in cooling tower design, it is necessary to quantify cooling requirements not only in terms of the range required in the circulating water, but also simultaneously in terms of the expected ambient air conditions. The design wet-bulb temperature is selected such that it is exceeded no more than 3 to 5% of the time during summer in an average year [1, 10].

The circulating water is assumed to be constantly surrounded by a film of saturated air, as shown schematically in Figure 2.3 below. Any mass or heat transfer between the air and water also passes through this saturated air film. Therefore, the driving force for the cooling is considered to be the difference in enthalpy between the saturated air film and the upward-flowing air adjacent to it. Conveniently, this enthalpy difference captures both temperature and humidity differences. This driving force varies throughout the tower, and can be visualized conveniently on a psychrometric chart such as Figure 2.2, modified so that enthalpy rather than humidity appears on the vertical axis.

2.1 Merkel Demand Curves

Cooling demand can be quantified for a certain design scenario, which can, in turn, be used to design a cooling tower suitable for that purpose. This section will describe in detail the 0D analysis of cooling demand for a counterflow cooling tower. By contrast, crossflow cooling

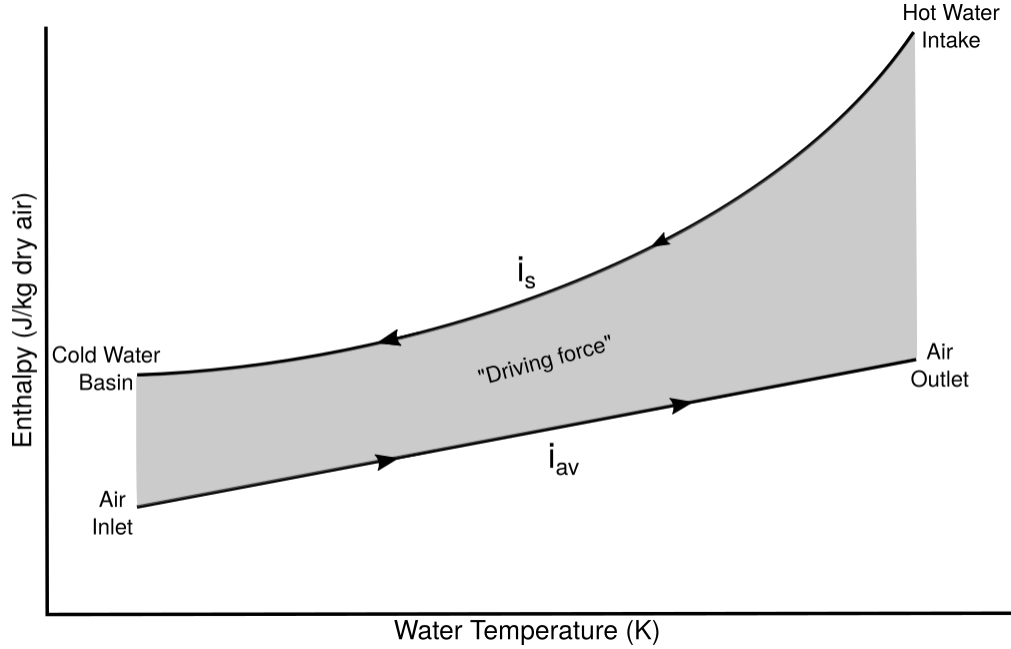


Figure 2.2 – Enthalpy of saturated air film at air-water interface and bulk air in a cooling tower

towers must be analysed numerically in 2D, since the air and water flow perpendicular to one another. The end result, however, is similar: a dimensionless Merkel number representing the difficulty of cooling for a given range, approach, and L/G ratio.

This derivation is based upon that of Kloppers and Kröger [15, 31], but a similar, less detailed derivation can be found in most cooling tower texts [1, 3, 5, 9, 32, 33]. The analysis begins by applying mass and energy balance in Control Volume 1 shown in Figure 2.3. In this control volume, a portion of the down-flowing liquid water is evaporated. The humidity increases in the exiting air as a result, but the amount of dry air remains the same, that is,

$$m_w + dm_w + m_a(1 + w) = m_w + m_a(1 + w + dw), \quad (2.1)$$

where m_w and m_a are the mass flow rates of water and dry air, respectively, in kg/s, and w is humidity in kg/kg. Cancelling terms, this simplifies to

$$dm_w = m_a dw. \quad (2.2)$$

An energy balance in this control volume results in

$$(m_w + dm_w)(i_w + di_w) + m_a i_{av} = m_w i_w + m_a(i_{av} + di_{av}), \quad (2.3)$$

where i_w is the enthalpy of water in J/kg and i_{av} is the enthalpy of the damp bulk air in J/kg of dry air. This energy balance equation can be simplified to

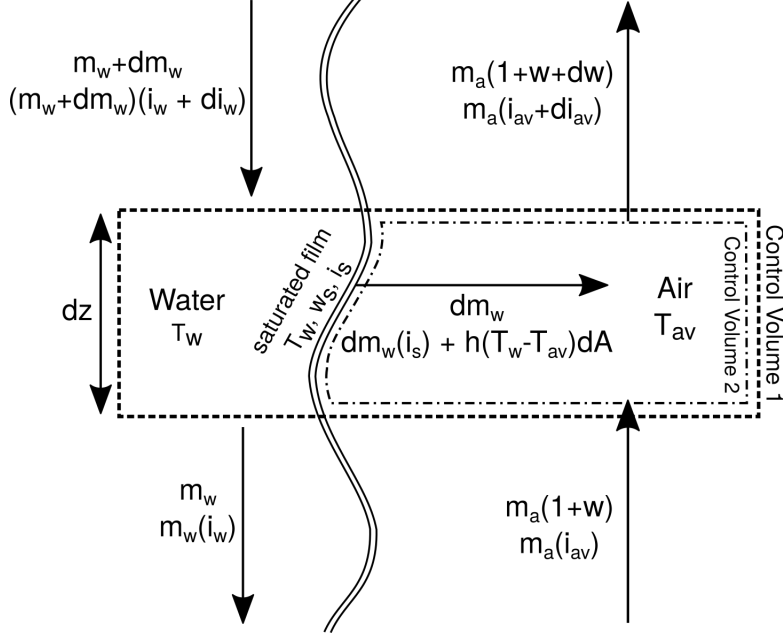


Figure 2.3 – Control volume for derivation of the Merkel number

$$dQ = m_a di_{av} = i_w dm_w + m_w di_w. \quad (2.4)$$

Looking at the energy transfer from the saturated film at the air-water interface to the bulk air (see Control Volume 2 from Figure 2.3), this heat can be broken down into two parts: the transport of vapour from the film, and the convective heat transfer between the bulk air on the film. Total heat transfer is therefore the sum of these, i.e.

$$dQ = dQ_m + dQ_c, \quad (2.5)$$

where Q is total heat transfer, Q_m is heat transfer due to mass transport of the vapour, and Q_c is heat transfer due to convective heat transfer.

Cooling due to mass transfer at the air-water interface can be quantified by multiplying the mass of water undergoing evaporation by the enthalpy of that vapour entering the bulk air stream:

$$dQ_m = i_s dm_w = i_s h_m (w_s - w_{av}) dA, \quad (2.6)$$

where i_s is the enthalpy of the saturated film in J/kg, h_m is the mass transport coefficient in kg/(m²s), w_s and w_{av} are the humidities of the saturated film and bulk air respectively in kg/kg dry air, and A is the interface area in m². By Newton's law of cooling, the convective heat loss between the liquid water and air can be expressed as

$$dQ_c = h(T_w - T_{av})dA, \quad (2.7)$$

where h is the convective heat transfer coefficient in $\text{W}/(\text{m}^2\text{K})$, and T_w and T_{av} are the temperatures of bulk water and bulk air in $^\circ\text{C}$.

Ultimately, it will be most convenient to express Q_c in terms of an enthalpy difference rather than a temperature difference. The enthalpy of the saturated air film is a function of the bulk water temperature and the saturated humidity, and can be broken down into its dry air and water vapour components, i.e.,

$$i_s = c_{pa}T_w + w_s(i_{fg} + c_{pv}T_w), \quad (2.8)$$

where c_{pa} is the specific heat of dry air at constant pressure in $\text{J}/(\text{kg K})$, i_{fg} is the latent enthalpy of evaporation at 0°C in J/kg , and c_{pv} is the specific heat of water vapour at constant pressure in $\text{J}/(\text{kg K})$. These specific heats are assumed to change very little with temperature. For later convenience, (2.8) can be rewritten as

$$i_s = c_{pa}T_w + w_{av}i_v + (w_s - w_{av})i_v, \quad (2.9)$$

where i_v is the enthalpy of the vapour at the bulk water temperature, given by

$$i_v = i_{fg} + c_{pv}T_w. \quad (2.10)$$

The enthalpy of the bulk, damp air in J/kg dry air is then

$$i_{av} = c_{pa}T_{av} + w_{av}(i_{fg} + c_{pv}T_{av}), \quad (2.11)$$

which, for convenience later on, will be written as

$$i_{av} = c_{pa}T_{av} + w_{av}(i_v - c_{pv}(T_w - T_{av})). \quad (2.12)$$

The difference between the film and bulk air enthalpies, the so-called ‘‘driving force’’, is expressed as

$$i_s - i_{av} = [c_{pa}T_w + w_{av}i_v + (w_s - w_{av})i_v] - [c_{pa}T_{av} + w_{av}\{i_v - c_{pv}(T_w - T_{av})\}]. \quad (2.13)$$

Rearrangement yields

$$T_w - T_{av} = \frac{(i_s - i_{av}) - (w_s - w_{av})i_v}{c_{pa} + w_{av}c_{pv}} = \frac{(i_s - i_{av}) - (w_s - w_{av})i_v}{c_{pav}}, \quad (2.14)$$

where c_{pav} is the specific heat of the damp, bulk air in $\text{J}/(\text{kg K})$, considering both its air and vapour components. Substituting this result into (2.7) yields the following relationship between convective heat loss and enthalpy:

$$dQ_c = h \left(\frac{(i_s - i_{av}) - (w_s - w_{av})i_v}{c_{pav}} \right) dA. \quad (2.15)$$

The total heat transfer is, therefore,

$$dQ = h \left(\frac{(i_s - i_{av}) - (w_s - w_{av})i_v}{c_{pav}} \right) dA + i_v h_m (w_s - w_{av}) dA, \quad (2.16)$$

which can be re-expressed as

$$dQ = h_m (\text{Le}_f (i_s - i_{av}) + (1 - \text{Le}_f) i_v (w_s - w_{av})) dA, \quad (2.17)$$

where Le_f is the Lewis factor. Not to be confused with the Lewis number, the Lewis factor compares the rates of heat and mass transfer in an evaporative process [34], and can be written as

$$\text{Le}_f = \frac{h}{c_{pav} h_m}. \quad (2.18)$$

Other analysis methods attempt to quantify the Lewis factor, but using the basic Merkel method, the Lewis factor is assumed to be unity. The justification for this assumption is that momentum dominates diffusive effects in a fully turbulent flow regime; turbulent eddies governing transport do not distinguish between heat and mass, and transport both at roughly equal rates. In reality, the Lewis factor can vary between 0.5 and 1.3, and various researchers have determined Lewis factors which are most accurate for specific cooling tower applications [34]. Using the Merkel assumption of $\text{Le}_f = 1$, (2.17) can be simplified to

$$dQ = h_m (i_s - i_{av}) dA. \quad (2.19)$$

In turn, using 2.4,

$$di_{av} = \frac{1}{m_a} dQ = \frac{h_m}{m_a} (i_s - i_{av}) dA. \quad (2.20)$$

Unfortunately, di_{av} and dA are not convenient for integration; there is no easy way to measure the upper and lower boundaries of enthalpy and interfacial area. From (2.4), making the basic Merkel assumption that evaporative losses of water are negligible,

$$di_{av} = \frac{m_w c_{pw}}{m_a} dT_w. \quad (2.21)$$

The gas-liquid interfacial area per unit volume of fill is denoted as a_{fi} , and the cross-sectional area of the tower as A_{fi} . On purely geometric grounds, dA can therefore be written as

$$dA = a_{fi} A_{fi} dz. \quad (2.22)$$

Combining (2.20), (2.21), and (2.22), and integrating yields

$$\int_0^{H_{fi}} \frac{h_m a_{fi} A_{fi}}{m_w} dz = \int_{T_{wo}}^{T_{wi}} \frac{c_{pw}}{i_s - i_{av}} dT_w. \quad (2.23)$$

This leads to the definition of the demand Merkel number as

$$\text{Me} = \frac{h_m a_{fi} A_{fi} H_{fi}}{m_w} = \int_{T_{wo}}^{T_{wi}} \frac{c_{pw}}{i_s - i_{av}} dT_w. \quad (2.24)$$

For a defined set of operating conditions, including inlet and outlet air conditions and inlet and outlet water temperatures, this dimensionless Merkel number expresses the difficulty of achieving the required cooling. A higher demand Merkel number corresponds to a more difficult cooling scenario. A larger cooling tower (with higher A_{fi} or H_{fi}) or a more efficient fill (a_{fi}) may be needed to meet particularly challenging operating conditions.

Note that a number of simplifying assumptions were made in this derivation:

- Evaporative losses to the mass of water are negligible,
- $\text{Le}_f = 1$; the mass and heat transfer occur at equal rates: $h/h_m c_p = 1$,
- There is no resistance to heat transfer on the water side of the interface shown in Figure 2.3. In other words, the water at each cross-section of the tower has uniform temperature T_w , and the saturated air film at its surface is at the same temperature.
- i_{fg} and c_p are effectively constant, independent of temperature.
- Not knowing the temperature or humidity of the outlet air, the total heat taken up by air could not be calculated from those conditions. For this reason, the Merkel method assumes the air to be fully saturated at outlet.

None of these assumptions are entirely valid, but they provide a reasonable approximation under most circumstances. Other methods have been developed which relax one or more of these assumptions, but the Merkel method still remains the most commonly-used method of cooling tower design due to its simple implementation and reasonably accurate results.

Because (2.24) cannot be solved analytically, a numerical quadrature method is typically used to perform the integration. The Cooling Tower Institute recommends the four-point Chebyshev quadrature method [35], but other methods such as trapezoidal rule can be used instead [3]. Whichever method of quadrature is chosen, in order to reduce error, the same method must be used for calculating the demand Merkel number and the supply Merkel curves, which are described in the following section.

If the demand Merkel number is calculated over a range of L/G ratios, these can be plotted as shown in Figure 2.4, creating a demand curve. As the L/G ratio increases, the Merkel number demanded will increase; if more water needs to be cooled or if less air is available to take up the heat and moisture, the larger or more efficient the cooling tower will need to be to achieve the required cooling load.

2.2 Merkel Supply Curves

To achieve various cooling performance requirements, considering the Merkel method of analysis, there are a number of variables which can be manipulated in the design of the cooling tower.

- Fill type (a_{fi} , affects h_m indirectly by altering the geometry of water-air interface)
- Fill height (H_{fi})
- Water loading per unit area (m_w/A_{fi})
- Air flow (m_{av}), controlled by the fan parameters such as fan speed and blade pitch.

Each combination of these factors will result in a different cooling capability, quantified as a supply Merkel number. Although it was shown above that the Merkel number can be expressed as

$$\text{Me} = \frac{h_m a_{fi} A_{fi} H_{fi}}{m_w}, \quad (2.25)$$

it is unfortunately very difficult to find concrete values for h_m and a_{fi} . For a geometry as complex as a cooling tower fill, both of these must be determined empirically (or perhaps from simulation). Although the product $h_m a_{fi}$ could be found through experimentation, h_m and a_{fi} cannot be determined individually without having access to the interior of the fill area for measurement. The cooling potential of a fill is therefore measured experimentally, and its resulting Merkel number plotted against the water-to-air loading ratio (L/G). A curve is customarily fit to these results, often using a form such as

$$\text{Me} = C_1 (L/G)^{C_2} H_{fi}^{C_3} \quad (2.26)$$

or

$$\text{Me} = C_1 L^{C_2} G^{C_3} H_{fi}^{C_4}, \quad (2.27)$$

where C_i are empirically determined constants.

If the demand and supply Merkel relationships are plotted together on the same graph against L/G , the point of intersection is the design point for that combination of operating and environmental conditions. See Figure 2.4 as an example taken from Appendix A.

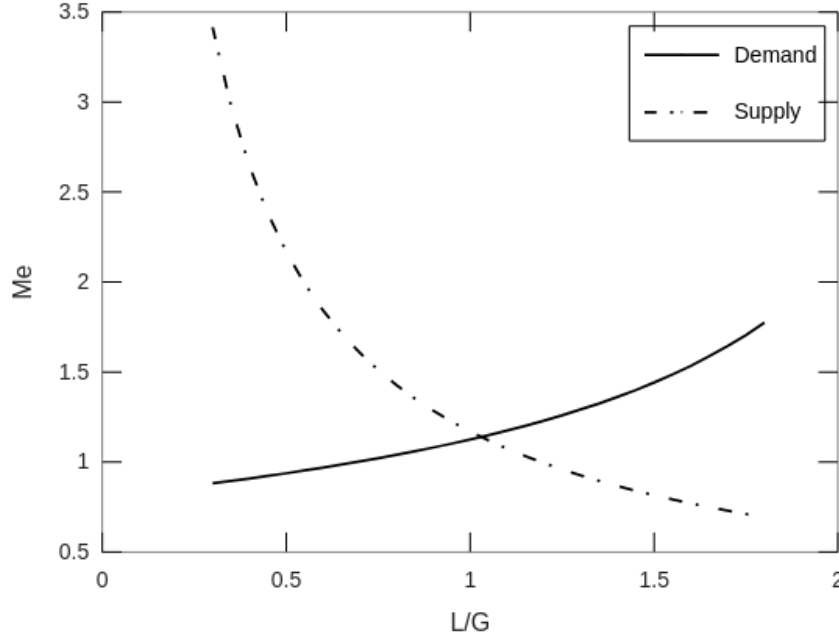


Figure 2.4 – Supply and demand Merkel number curves for Appendix A example

2.3 Airflow and Static Pressure Loss in 0D

For steady, ideal, frictionless flow along a streamline, Bernoulli’s equation states that

$$\frac{\rho v^2}{2} + P_s + \rho g H = \text{constant}, \quad (2.28)$$

where ρ is the density of air, v is the velocity of air, P is static pressure, g is gravitational acceleration, and h is the height of the measured point. For real, non-ideal flows, this relationship can be modified to account for loss of momentum by adding a term to account for friction and dynamic losses in the system, i.e.,

$$\frac{\rho_1 v_1^2}{2} + P_{s1} + \rho_1 g H_1 = \frac{\rho_2 v_2^2}{2} + P_{s2} + \rho_2 g H_2 + \Delta P_{\text{loss}}, \quad (2.29)$$

where the indices 1 and 2 refer to locations upstream and downstream of the component creating the losses, respectively. If ΔP_{loss} is determined empirically, the streamline assumption is unnecessary [36]. In the testing facility described in this thesis, the change in air density should be negligible ($\rho_1 = \rho_2$), and the cross-section above and below the tested section are equal ($v_1 = v_2$). Further, the hydrostatic pressure difference is not included in these measurements; the differential pressure sensor is open to the ambient lab air on one side and connected by flexible tubing to the pitot tube positioned above the fill on the other side. Because the same hydrostatic column of air exists inside and outside the tubing, the pressure difference across the differential pressure sensor does not include hydrostatic pressure. In

other words, as measured, $h_1 = h_2$. Therefore

$$\Delta P_{\text{loss}} = \left(\frac{\rho v_1^2}{2} - \frac{\rho v_2^2}{2} \right) + (P_{s1} - P_{s2}) + (\rho_1 g H_1 - \rho_2 g H_2) \quad (2.30)$$

becomes

$$\Delta P_{\text{loss}} = P_{s1} - P_{s2}. \quad (2.31)$$

The pressure loss created by a certain flow element can be characterized with respect to air velocity, typically done through experimentation as shown in Section 4.3 or using CFD. In these experiments or simulations, the element is usually installed with a long straight section before and after it so as to avoid effects from other system features. This is not the case when the interaction between multiple components is the subject of study.

The pressure loss is often proportional to dynamic pressure. In these cases, the losses for the element are characterized by K , that is,

$$\Delta P_{\text{loss}} = K \frac{\rho v^2}{2}. \quad (2.32)$$

In cooling tower analysis, the sum of the dynamic pressure losses determined for each element in this way can be balanced against the static pressure generated by a fan at the desired air flow rate, providing a basis for fan sizing. In a functioning cooling tower, there is some change in air density as the air gains heat and moisture, therefore additional terms for the new mass and buoyant forces can be added, i.e.,

$$\Delta P_{\text{fan}} - \Delta P_{\text{loss}} - \Delta P_{\text{evap}} + \Delta P_{\text{buoy}} = 0. \quad (2.33)$$

However, ΔP_{fan} and ΔP_{loss} will be the dominant terms for the analysis of a mechanical draft cooling tower. A sound estimate of ΔP_{loss} allows a fan to be selected correctly, achieving the required airflow while avoiding the expense of excessive oversizing.

Chapter 3

Design of the Experimental Model

This chapter will introduce each major component of the experimental model. The design basis for each of these subsystems will be discussed at a high-level. Appendices B, C, and D will respectively describe the detailed design of the water, steam, and data collection systems including calculations, component selection, and layout.

The design objectives for this experimental model were as follows:

- a lab-scale model representing all major features of a full-scale induced draft counter-flow cooling tower in multiple configurations, including probe holes for the collection of 3D measurements,
- a variable supply of water within a range of 2.7 to 8.1 L/m²s,
- a variable supply of air within a range of 1.5 to 3.6 m/s,
- a source of variable heat which could be made available in the laboratory, sufficient to heat the circulating water to 50°C, and
- a data collection system to measure air velocity and pressure, water and air flow rates, ambient air conditions, and water temperature.

Constraints on the design included a maximum available vertical height of approximately 5.6 m, a maximum floor loading of 1460 kg/m², and practical space considerations in the laboratory. The tower's cross section was limited by the maximum feasible heat, water, and air flow rates possible in the laboratory space given the desired loadings listed above.

3.1 Cooling Tower

The experimental model cooling tower utilized in this work is shown in Figure 3.1. All key elements of a full-scale cooling tower are represented: the fill, water distribution system,

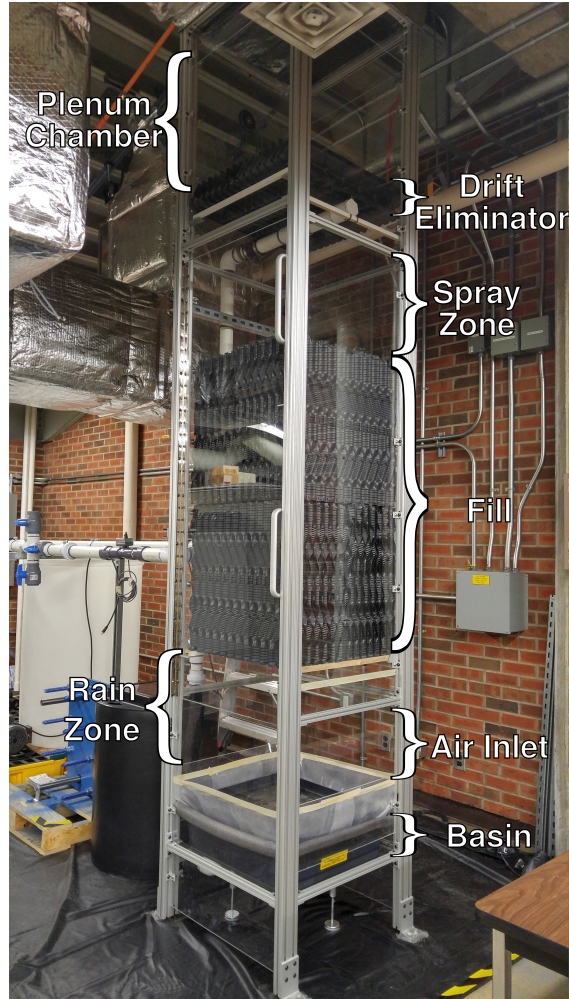


Figure 3.1 – Lab-scale cooling tower model

fan, drift eliminator, and basin. The tower cross-sectional area was limited to 645×645 mm; although the physical space was available to accommodate a larger tower, there was not sufficient space to accommodate the pump, fan, and heating equipment that would be required to operate it. Several experiments in literature have used cooling towers with larger cross-sections [19, 27, 29, 30, 37], while others have used models with a smaller cross-section [38, 39]. Larger experimental models are used to reduce the impact of edge effects and provide maximum accuracy. For counterflow, models having a cross-section of up to $7 \text{ m} \times 7 \text{ m}$ have been recommended [15]. For the smaller tower described in this thesis, alternative measures are taken to minimize edge effects. For example, outlet water measurements are taken from the sampling basin, which collects water which has fallen from the fill above but not water which has run down the cooling tower walls.

The available height in the laboratory limited the total height of the experimental tower to 3.7 m, leaving room above for ductwork. As a consequence, the air inlets, the plenum

chamber, and the spray zone are shorter than in a typical induced draft cooling tower. In order to fully capture the effects of the fill - the most critical component for thermal performance - the model has been designed to accommodate fills as tall as 6 ft in order to match the film-type fill heights used typically in full-scale applications.

To study the performance and behaviour of modern film fills, Brentwood's OF21MA fill was selected as a typical example. Film fills such as this one are intended to strike a balance between thermal performance and fouling resistance. When multiple layers of fill were used, they were stacked in an orientation rotated by 90 degrees; if the sheets of the bottom layer of fill ran left-to-right, the second layer was installed so that the sheets ran back-to-front. This was done so as to allow air and water redistribution in both directions, but also to prevent the formation of a continuous gap through the centerline of the tower where two side-by-side sections of fill meet. Any significant gaps between the installed fill sections and the cooling tower wall were filled with spare, loose sheets of the same type of fill.

The frame of the lab-scale model was built with 8020 aluminum T-slot framing so as to allow for relatively simple repositioning and interchanging of internal and external components. Transparent acrylic sheets of 6 mm thickness were used for the walls of the tower so as to allow visual access, especially for troubleshooting purposes. The transparent walls also allow for photographic study of droplets in the spray or rain zone to be performed in the future if necessary.

Ideally, the water distribution system inside the lab-scale tower should match that used in a full-scale cooling tower. As discussed in Section 1.4.3, water distribution systems come in various designs. Because of the limited cross-sectional area of the lab-scale model, an array of nozzles was not possible. Instead, a single low-pressure spray nozzle was used. This single nozzle can be easily changed out for different nozzle models, and the height of the spray zone can be adjusted to obtain satisfactory spray coverage over the fill cross-section. Only nozzles with sprays which angle downward are suitable for this apparatus; nozzles with significant horizontal sprays result in an excess of wall water which bypasses the fill entirely. The nozzles used successfully in this model include the BETE NC 2065 and C.E. Shepherd counterflow SP nozzle.

A Brentwood CF150MAx drift eliminator is also included as a tower component so as to allow for the characterization of its effects on airflow. The drift eliminator also prevents small liquid droplets from entering the ductwork and fan where they could cause rust.

The basin at the bottom of the tower is used to collect the cooled water and allow it to be returned ultimately to the cold water tank. The basin of this tower has a central "sampling basin" from which temperature measurements are taken, and a larger "drainage basin" which collects water flowing out of the sampling basin as well as water which has flowed down the tower walls rather than flowing through the fill.

3.2 Water System

Each type of fill can be operated within a certain range of acceptable air and water loadings per unit area. If the water loading is too low, water is distributed unevenly, and cooling performance suffers. If the water loading is too high, flooding occurs, resulting in higher air pressure losses and stifled airflow [3]. It has been argued, however, that standard water loading limits are more influenced by economic factors than by any physical phenomena within cooling towers [1]. The water flow rates for this experimental model were selected with the intention of testing the OF21MA fill across a range of water flow rates from 4 to 12 gpm/ft² (2.7 to 8.1 L/m²s).

The water system for this model is designed to allow for multiple modes of operation depending upon the water and heat demands of the experiment, as shown in Figure 3.2, where the water system components in use are highlighted in coral red. A set of quarter-turn on/off valves can be adjusted to achieve the desired operating mode.

Flow rates are controlled by two globe valves located downstream of each feed pump - one of these connects to a recirculation line leading back to the tank, and the second connects to the feed line (which goes to the cooling tower or heat exchanger). This arrangement allows a large range of possible flow rates, and keeps the water in the hot and cold water tanks well mixed.

One-tank mode is used when the heat being dissipated in the experiment is less than the maximum heat which can be added to the water in a single pass through the heat exchanger with the maximum steam flow rate. In this case, water at constant temperature is provided to the cooling tower directly from the heat exchanger. After cooled water exits the cooling tower and is returned to the cold water tank, it can be pumped with the cold water pump back through the heat exchanger and into the cooling tower once again.

It is also possible that the heat being dissipated in the experiment is greater than that which can be provided by a single pass through the heat exchanger. In this high water flow, high temperature drop case, the experiment can be operated in two-tank mode. In this mode, water is drawn from the hot water tank (pre-filled with hot water of the appropriate temperature) and sent to the cooling tower. The cooled water falls to the basin and is returned through the sump pump to the cold water tank. Water is pumped from the cold water tank through the heat exchanger to replace the water being lost from the hot water tank, but this flow rate will be less than that being drained, and the hot water tank will gradually empty over the course of the experiment. Unlike one-tank mode, this method of operation limits the duration of the experiment.

Preheat mode is used to warm the water in the hot water tank to the desired temperature before one- or two-tank operation. In this configuration, water is circulated through the heat

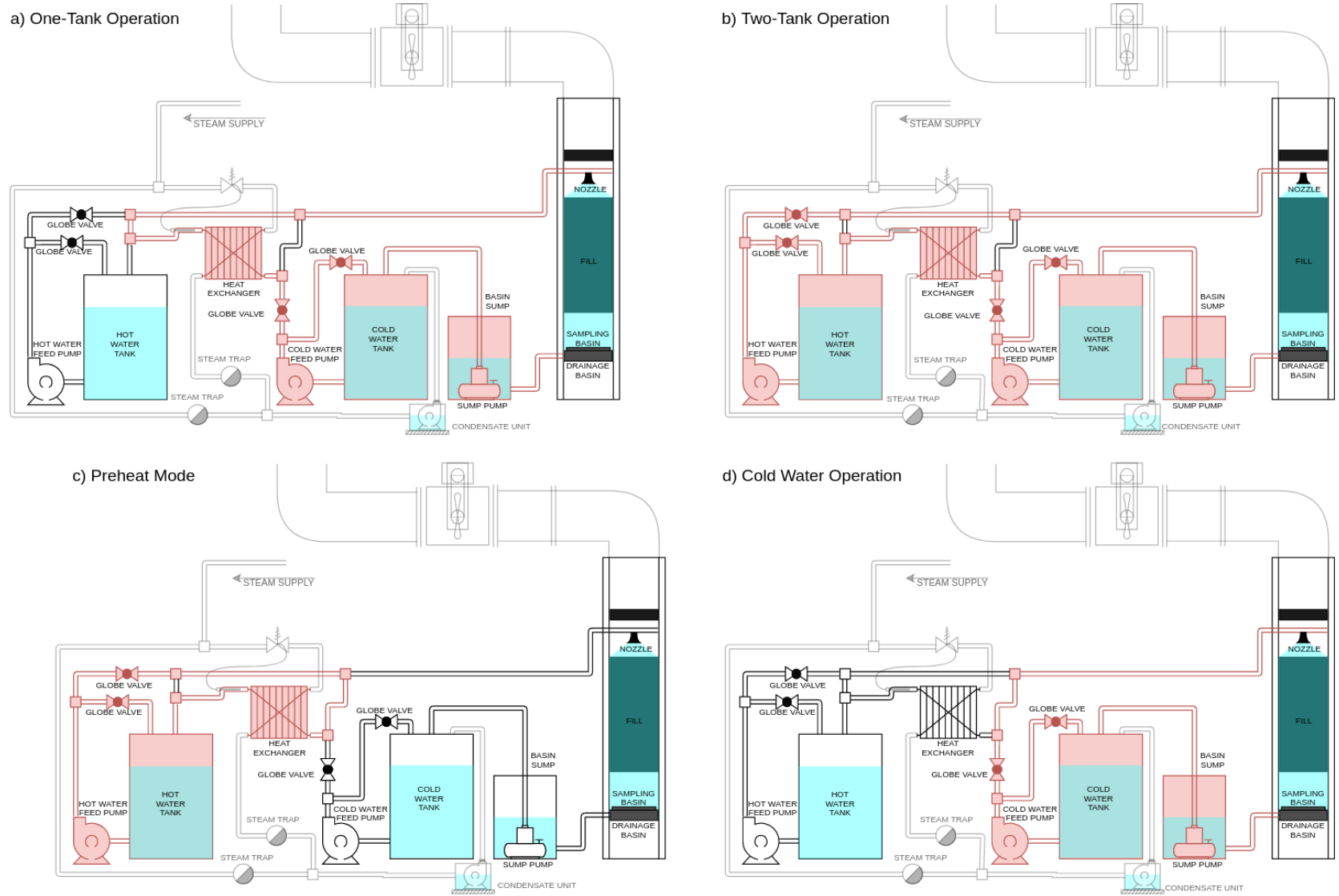


Figure 3.2 – Operating modes for water system
 Clockwise from top left: a) One-Tank, b) Two-Tank, c) Preheat, and d) Cold Water modes

exchanger and back to the hot water tank in a loop until the desired hot water temperature is reached.

In experiments where heat is not required, such as pressure drop characterization, cold water mode is used. Water is run from the cold water tank directly to the cooling tower, having no interaction with the heat exchanger or hot water tank.

3.3 Steam Heating System

For the purpose of bringing the system water up to the desired temperature, a plate-and-frame heat exchanger (Tranter SUPERCHANGER UXP-005-L-6-UI-28) is used with a supply of low-pressure steam. The steam flow rate is controlled by a temperature regulating valve (Spence 2030TG-GQE) whose sensing bulb is placed in the stream of hot water exiting the heat exchanger. This valve adjusts the flow rate of steam to achieve a desired output temperature in the heated water. Downstream of the heat exchanger, a float-and-thermostatic steam trap (Hoffman Specialty FT30H-6) serves to remove air and liquid condensate while preventing loss of steam, and a vented condensate unit including a receiver and pump (Hoffman Specialty Model WC6-20B) collects the hot condensate and returns it to the cold water tank as a source of make-up water. A drip line with its own float-and-thermostatic steam trap (Hoffman Specialty FT30H-3) keeps the supply of steam to the heat exchanger free of liquid water. Figure 3.3 shows the steam heating system as installed including each of these components connected by black steel pipe. The temperature regulating valve is shown on the right (its temperature sensing bulb is not installed in the hot water line in this image), along with the plate-and-frame heat exchanger on the left, and the two steam traps and the condensate unit are shown on the right. See Figure 3.4 for a schematic diagram of the overall steam system arrangement.

The maximum flow rate of steam is estimated at 206 kg/hr (454 lb/hr), which equates to 128 kW of latent heat. This flow rate was estimated by employing the Bernoulli equation using the flow coefficients provided for the temperature regulating valve, heat exchanger, strainers, and steam traps. Appendix C describes this calculation in full and provides additional design details such as component selection and layout. For a stream of water having a flow rate of 3 L/s, this system should be capable of raising the liquid water temperature by up to 10.2°C, i.e.,

$$\Delta T = \frac{\dot{Q}}{\dot{m}_w c_{pw}} = \frac{128 \text{ kW}}{3 \text{ kg/s} \times 4.18 \text{ kJ}/(\text{kg K})} = 10.2^\circ\text{C}, \quad (3.1)$$

with each water pass through the heat exchanger. For the same heat input (i.e. stream flow rate), a smaller flow of liquid water could be heated to still larger temperatures on each pass.



Figure 3.3 – Steam heating system as installed

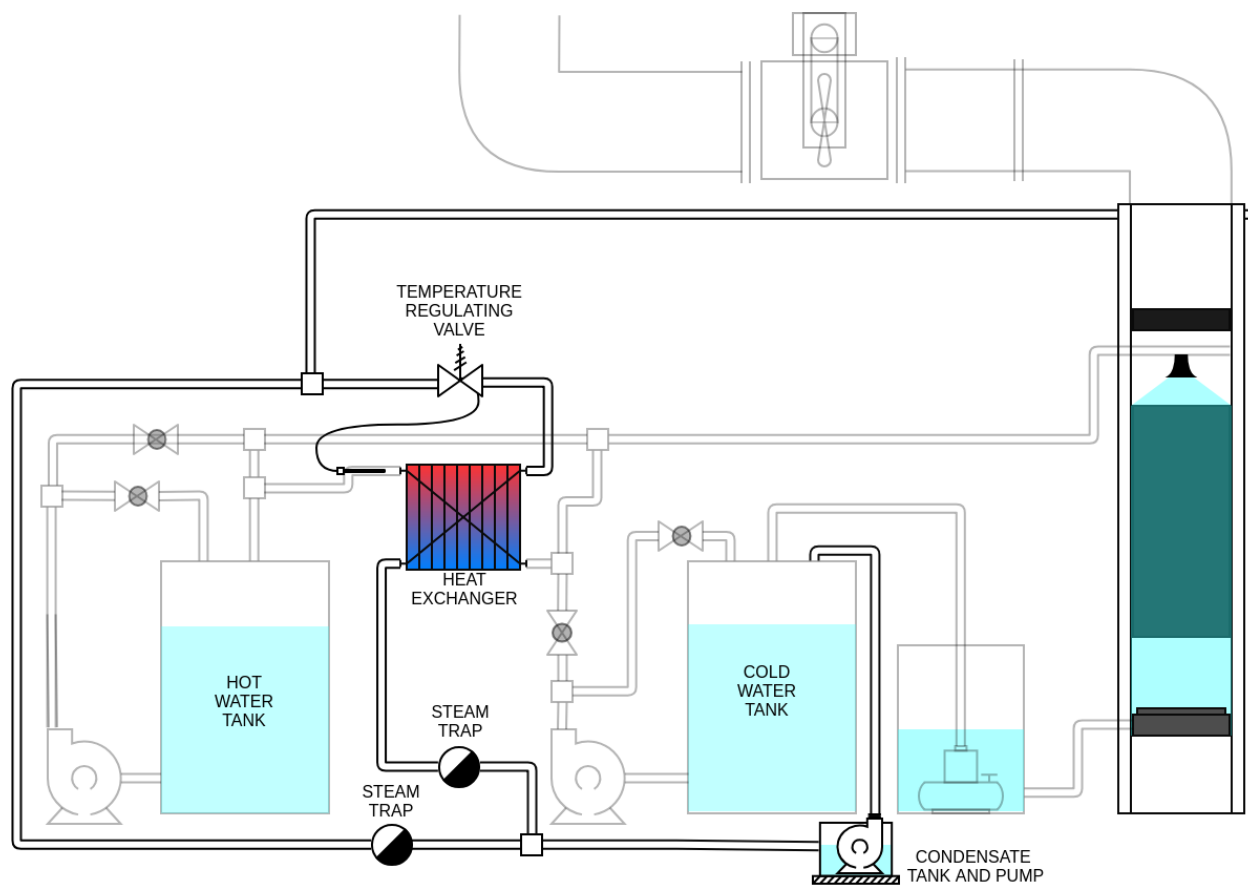


Figure 3.4 – Steam heating system schematic

If a single pass is insufficient for the required water flow rate and temperature of a particular experiment, the water must be preheated and used in two-tank operating mode as described in Section 3.2.

3.4 Air System

To ensure that the airflow in the lab-scale model represents the conditions in an induced-draft cooling tower, the fan (Greenheck BSQ 160 1½ hp) is located at the air outlet. Ductwork connects the top of the cooling tower to this fan, and provides a route for the moist exhaust air to pass through the laboratory roof to the outdoors as shown in Figure 3.5. The ductwork connecting the top of the model cooling tower to its fan takes several 90° bends in order to accommodate the ceiling geometry and the ambitious tower height of 3.7 m.

The design air flow range for the lab-scale model was 300 to 700 fpm (1.5 to 3.6 m/s). This desired flow rate and the corresponding expected maximum pressure drop from the cooling tower was provided to a third party who specified the fan and designed the connecting ductwork. The total static pressure drop considered in fan sizing was estimated as 435 Pa given the 23" × 23" ductwork and tower components (including the drift eliminator and wetted fill). This was a rough estimate due to the closely-spaced bends in the ductwork, the losses not specifically accounted for such as inlet effects, and the unusual geometry of the rooftop gooseneck vent. The fan was selected to provide up to 2800 CFM of airflow at this static pressure drop with the fill and drift eliminator in place with a maximum water loading.

Experiments found that the maximum airflow rate was approximately 2.7 m/s (2380 CFM) when the tower had no fill or drift eliminator installed and no water flowing through it. When the drift eliminator and 4 ft of OF21MA fill were installed, this flow rate reduced further to 1957 CFM, with a velocity of 2.2 m/s. Measurements suggest that this loss in airflow is likely due to a pressure drop larger than anticipated in the rooftop gooseneck vent.

3.5 Sensors and Data Collection

I selected all sensors used in this testing facility, but the microcontroller, breakout boards for the LMI sensors, and the LabVIEW program were all created by an electronics engineering tech in the Mechanical Engineering Department. The sensors are summarized schematically in Figure 3.6.

Entering and exiting water temperatures are measured with J-type thermocouples (Watlow 24DJFGF048A and Omega TJ36-ICSS-18U-12, respectively). The water flow rate is measured with a turbine flowmeter before entering the cooling tower (Omega FTB694-NPT-

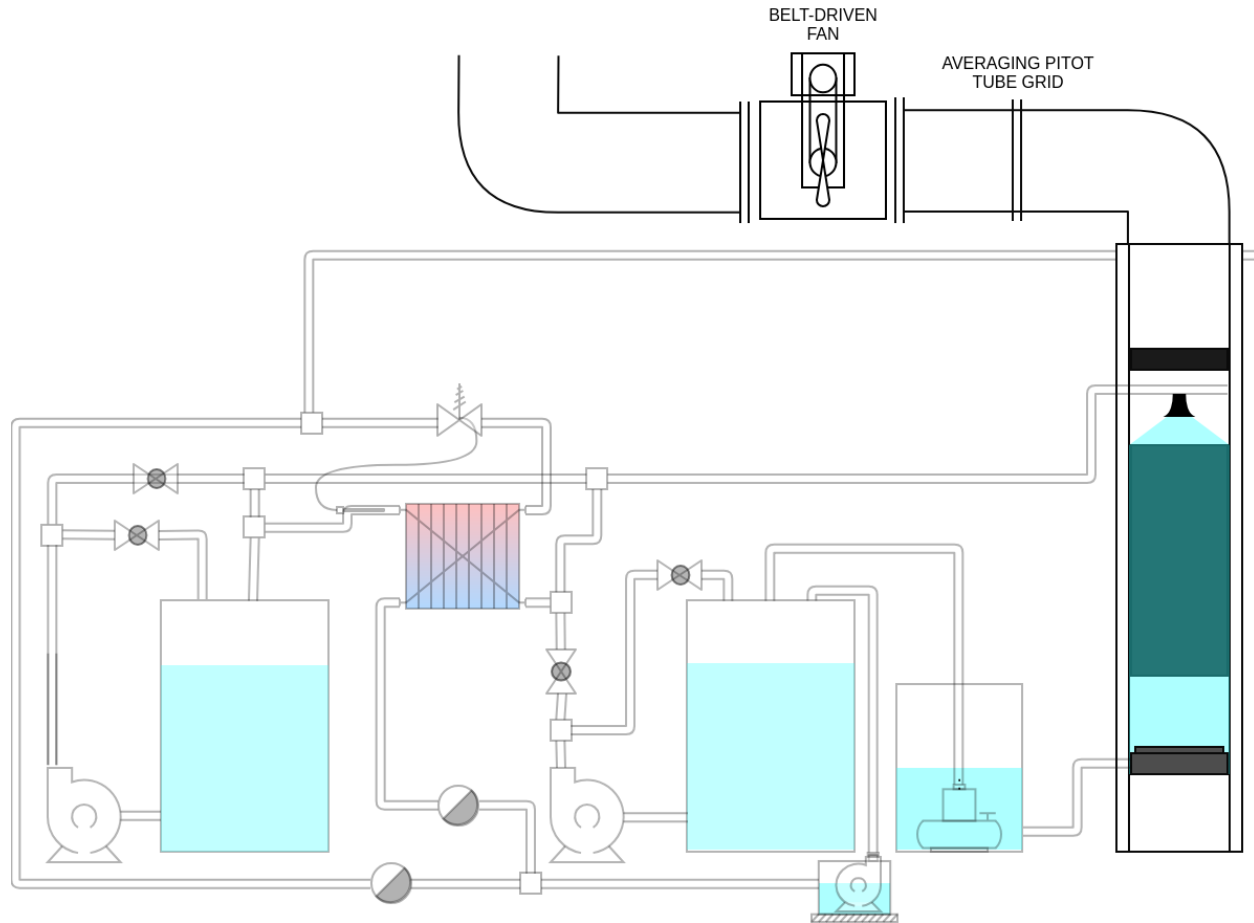


Figure 3.5 – Air system schematic

P). Chip-based sensors with Adafruit breakout boards are used to measure ambient air temperature and humidity (Sensiron SHT31-D with membrane) and ambient pressure (Bosch BME680). Total air flow rate is measured using a duct-mounted averaging pitot tube (Dwyer STRA-R22X22) coupled with a humidity-resistant thermal airflow measurement chip (First-Sensor LMIS025UB3S). The vertical component of the air velocity field inside the cooling tower is measured with a straight pitot tube (Dwyer 160F-24) which is inserted into the tower via pre-drilled holes, coupled again with the same humidity-resistant thermal airflow measurement chip.

The thermocouples are read by a thermocouple input DAQ module (National Instruments 9211), while the chip signals were interpreted by a microcontroller, both of which connected by USB to a computer where the results were displayed and recorded by LabVIEW program. The LabVIEW interface is shown in Figure 3.7, which displays live data and allows the experimentalist to record the required data into a CSV file.

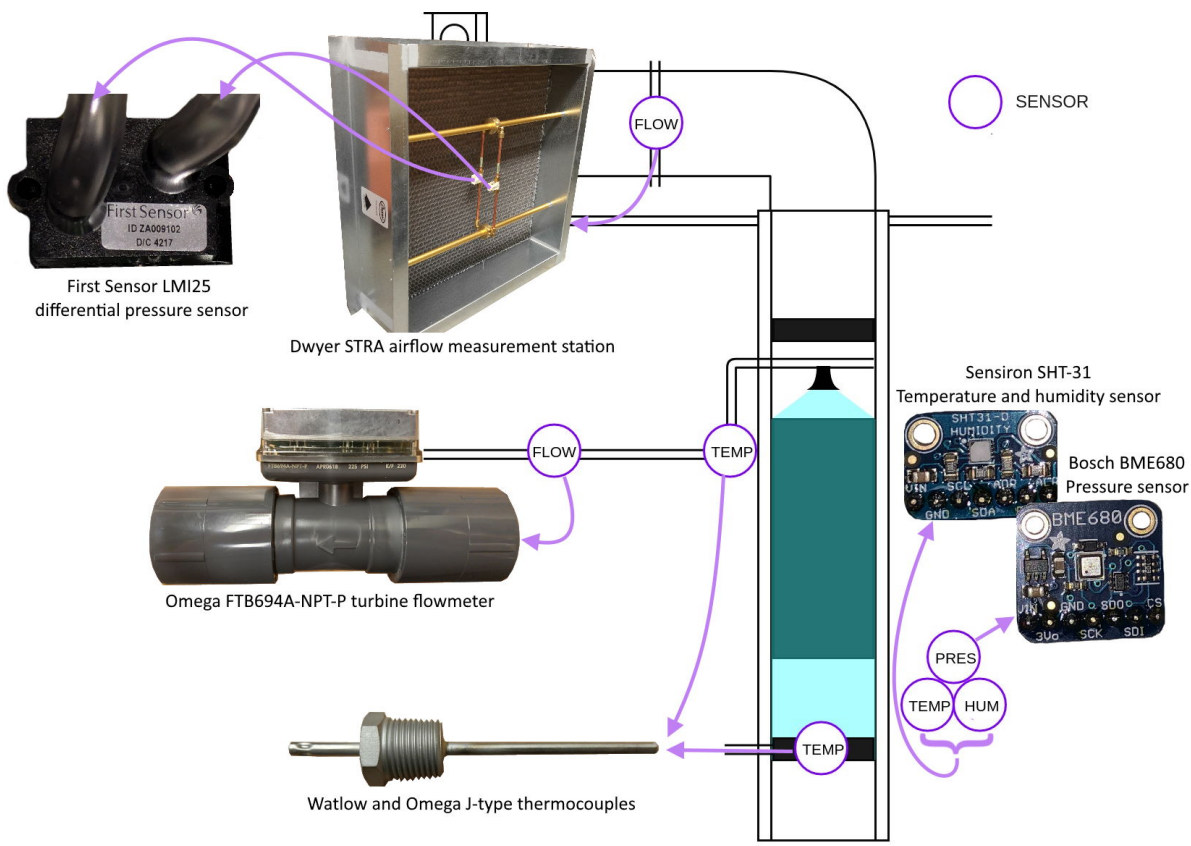


Figure 3.6 – Instruments used in the cooling tower test facility



Figure 3.7 – LabView GUI for collection of sensor data

Chapter 4

Results

4.1 Validation of Airflow Readings

The straight geometry of Dwyer's 160F pitot tube proved to be very useful in taking point measurements of velocity and static pressure drop inside the cooling tower; not only was it easy to insert through holes drilled through the side of the tower at the planes indicated in Figure 4.1, but this pitot tube also enabled measurements to be collected from the same height as that of the hole itself. A standard (L-shaped) pitot tube would sample at a location upstream of the insertion point, since the long protruding end must be inserted into the flow. However, the accuracy of this straight pitot tube was given by the manufacturer as $\pm 2\%$ full-scale, where full scale is 45 m/s. This gives an uncertainty of ± 0.9 m/s, which is substantial at the range of velocities in question (approximately 0 to 6 m/s). Therefore, the first experimental activities were chosen so as to investigate the reliability of this pitot tube and sensor combination as compared to other instruments.

4.1.1 Pitot Tube Comparison

Because of concerns related to the accuracy of the straight 160F pitot tube introduced above in Section 4.1, the 160F readings were compared against a standard L-shaped pitot tube to determine the accuracy and precision of the 160F. The L-shaped pitot tube selected for comparison has a reported accuracy of $\pm 2\%$ of reading, i.e. a much higher accuracy than the 160F, especially at low velocities.

Above the plenum traverse plane shown in Figure 4.1, a single hole was drilled so as to be large enough for the L-shaped pitot tube to be inserted. This hole was intentionally placed in such a position that the L-shaped pitot tube would sample the airflow in the same location as that sampled by the straight 160F pitot tube inserted into the center hole of the plenum traverse plane. Because there is a gap of several centimeters between the total and static pressure sampling points of the L-shaped pitot tube, while the same gap for the

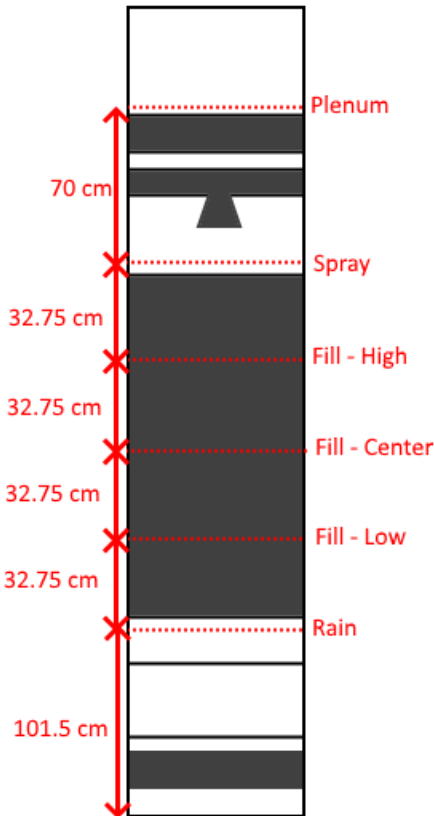


Figure 4.1 – Traverse locations and their respective labels

For empty tower tests, the grey areas are empty, but the naming convention for the planes is maintained.

160F is less than 1 cm, the two pitot tubes could not be expected to yield the same reading in an air flow stream with significant disturbances. With this fact in mind, measurements were made at a location near the top of the tower in an attempt to ensure a smooth (if not fully-developed) velocity profile. To this end, a single layer of 30 cm fill was added to the tower to smooth the velocity profile further.

Velocities were recorded at five locations with both pitot tubes. Each set was repeated five times and ensemble averaged for each of the five locations (shown on the left in Figure 4.2). The procedure was first performed with a high air speed, then repeated with a low air speed. Figure 4.3 summarizes these results together with error bars reflecting the combined uncertainty of the pitot tube and LMI, as reported by their manufacturers. The propagation of these errors is shown in Appendix E, Section E.3. The two pitot tubes yielded remarkably similar measurements, although the L-shaped pitot results tended to be slightly elevated with respect to the 160F results.

When reading these graphs and others in this section, Figures 4.3, 4.4, 4.5, 4.6, and

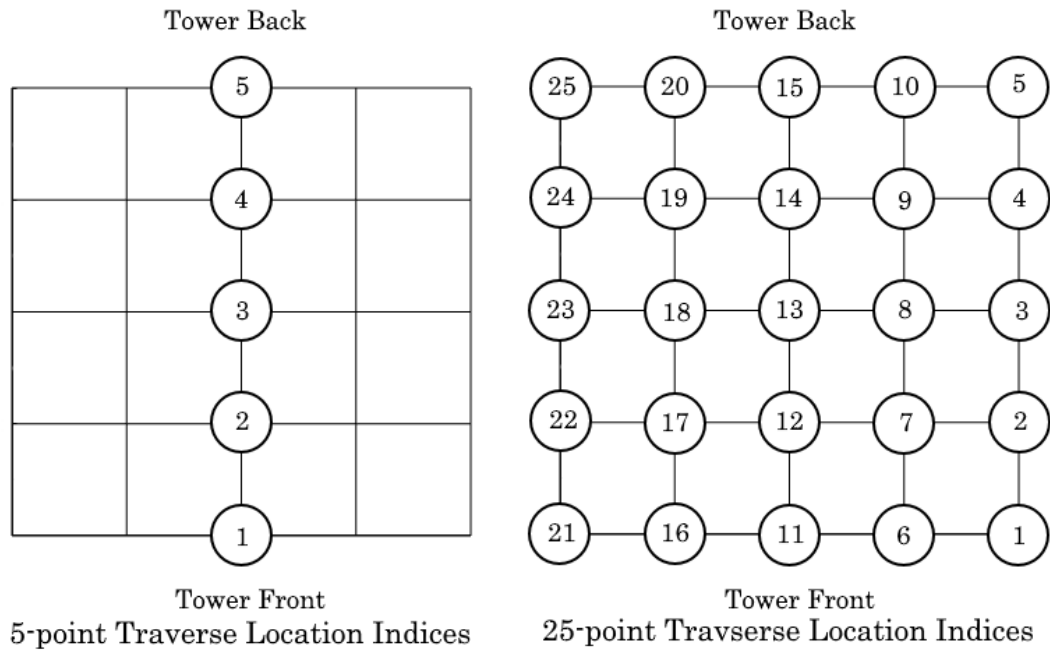


Figure 4.2 – 5-point Location indices used in Figures 4.3, 4.4 and 4.7, and 25-point location indices used in 4.4, 4.5, and 4.6

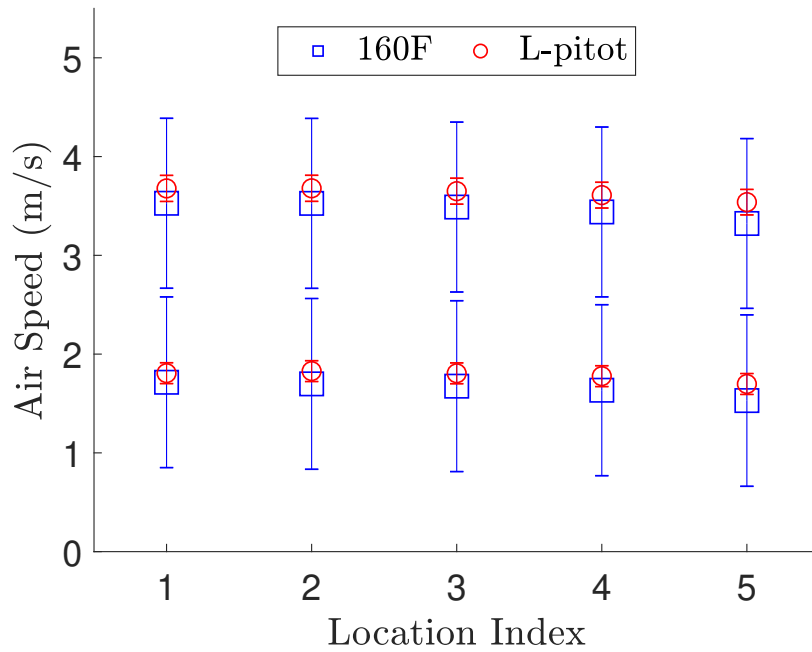


Figure 4.3 – Pitot tube and sensor comparison plotted with manufacturer-reported error

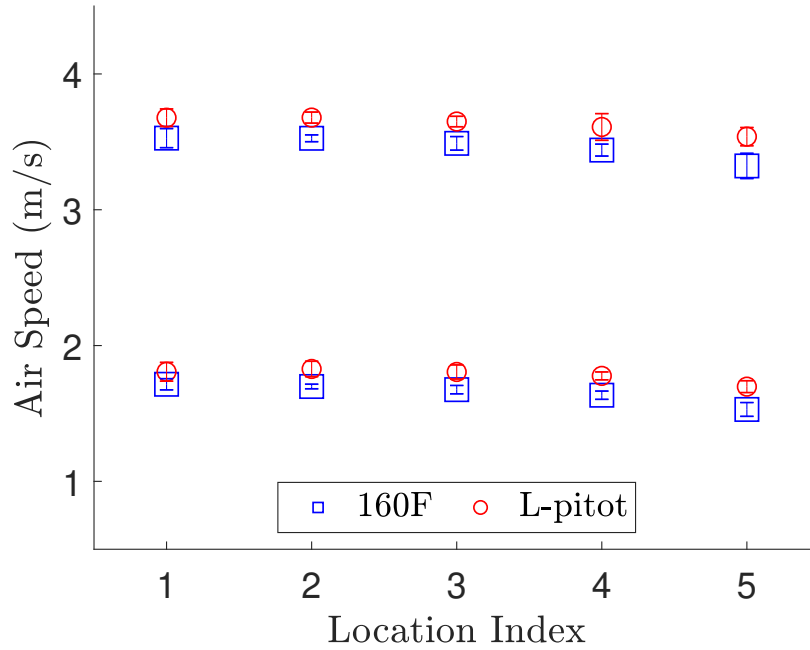


Figure 4.4 – Pitot tube comparison plotted with tested 95% confidence interval

4.7, note that instead of being arranged in two dimensional space, the different measurement locations have been assigned an index number according to Figure 4.2. This plotting method allows different readings in the same location to be compared more easily. The actual flow field is not interesting for these validation experiments, rather, it is the way that readings compare to one another at the same location that must be emphasized.

Figure 4.4 shows the same readings displayed together with error bars reflecting the 95% confidence interval of the measurement, considering the five measurements taken. The 160F pitot tube seems to yield measurements of much higher quality than the reported uncertainty of ± 0.9 m/s would suggest, comparing very well against results measured with a traditional L-shaped pitot tube. Therefore, the 160F readings can be said to yield velocity readings which are very close to those collected from the more accurate L-shaped pitot tube. Within the range of air velocities reported in Figure 4.4, the 160F pitot tube seems to introduce consistent bias of approximately -0.15 m/s with respect to the L-shaped pitot results. The readings obtained with the 160F system were very consistent however, with a 95% confidence interval of ± 0.03 from the mean for both high and low velocity cases. The accuracy of the 160F pitot tube relative to the L-pitot is ± 0.03 m/s with a bias of +0.15 m/s. Conservatively, and assuming the L-pitot results to be the true values, the uncertainty of the 160F used in this method could be estimated at ± 0.2 m/s. However, this uncertainty is very low compared to the precision error associated with velocity measurements inside the tower due to turbulence

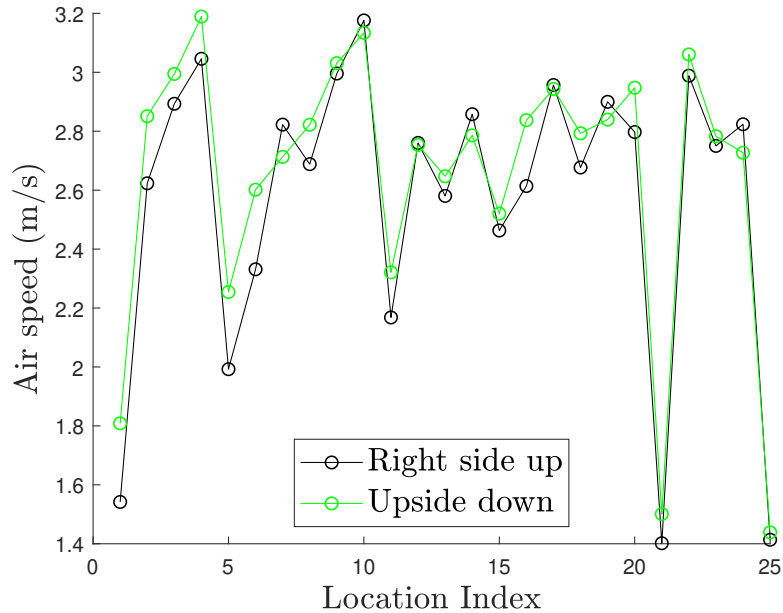


Figure 4.5 – Symmetry comparison of velocity measurements

(addressed in Section 4.1.5), and therefore is not the dominating term in uncertainty that will be considered in error analysis of the 160F.

4.1.2 Pitot Tube Asymmetry

In a standard L-shaped pitot tube, the static pressure sampling points would typically connect to the shell of the pitot tube and thereby connect to the larger take-off point. Conversely, the total pressure sampling point is typically connected to a tube that runs through the pitot tube’s shell and connects to a smaller take-off point. Unfortunately, it was easier for the experimentalist to accurately position the 160F pitot tube in this experimental model the other way around; when the 160F pitot tube’s wide take-off port faces downwards rather than upwards, a spirit level can easily be added to the top of the pitot tube to ensure that the pitot tube is held at the proper inclination in two planes. See Section E.6 for details regarding uncertainties with regards to pitot tube positioning.

Tests were performed for each configuration to confirm whether there was any systemic bias in measurements taken using the 160F pitot tube in this preferred orientation, which will be referred to as “right-side up”. To do this, a 25-point traverse was obtained at the plenum plane (see Figure 4.1) of an empty tower, measuring velocity and static pressure. This plane and tower configuration were chosen arbitrarily. The measurements were repeated, collecting three sets of data for both “right-side up” and “upside down” orientations. The measurements from all three tests have been averaged and are shown in Figures 4.5 and 4.6.

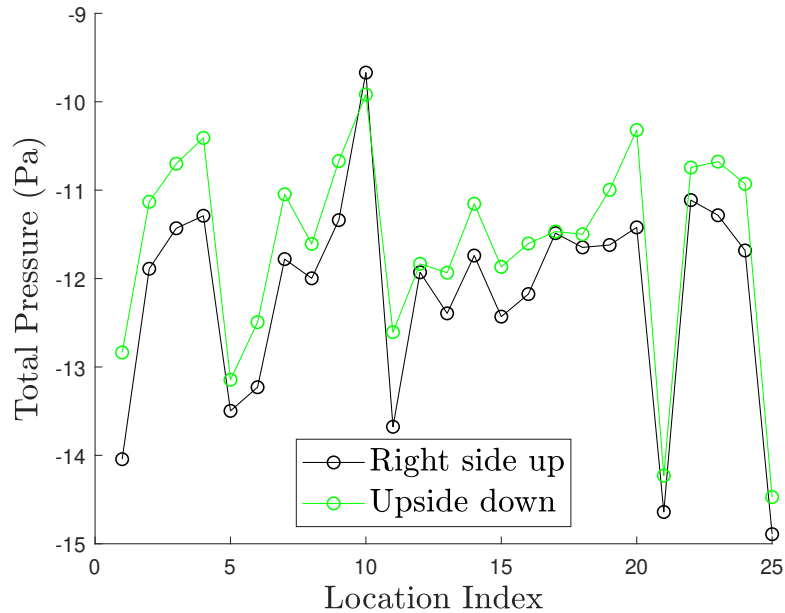


Figure 4.6 – Symmetry comparison of pressure measurements

On average, the velocity measurements in both orientations shown in Figure 4.5 are very similar, with a variation in the range of 0.2 m/s; typically the “upside-down” measurements yield slightly higher results. Considering the pitot tube’s precision accuracy (± 0.8 m/s from Section 4.1.5), this variation seems to be more than acceptable. On the other hand, Figure 4.6 shows that the total pressure drop measured “upside down” yields results that are consistently 0.5 to 1 Pa higher. Although such an offset is significant compared to the LMI uncertainty of $\pm 1.5\%$ of reading ± 0.1 Pa, the total uncertainty estimated for static pressure is 1 to 6 Pa based on the analysis in Appendix E, which is much more significant than this asymmetry effect. These differences, though important to highlight here, were considered minor enough that the remainder of experiments could confidently be performed in the “right-side up” configuration.

4.1.3 Differential Pressure Sensor Comparison

To compare readings provided by two differential pressure sensors while using the same pitot tube, a five by five grid of sampling points were measured by traverse across the plenum plane shown in Figure 4.1 while the lab-scale cooling tower was empty.

The measurements were taken with the 160F straight pitot tube using both the Fluke 922 and the LMI sensor so as to compare the two. The LMI sensor readings were recorded by LabVIEW, which collected readings every 30 ms for a 10 s interval at each location, averaged these readings at each location, and stored them in a text file. The Fluke 922 provided

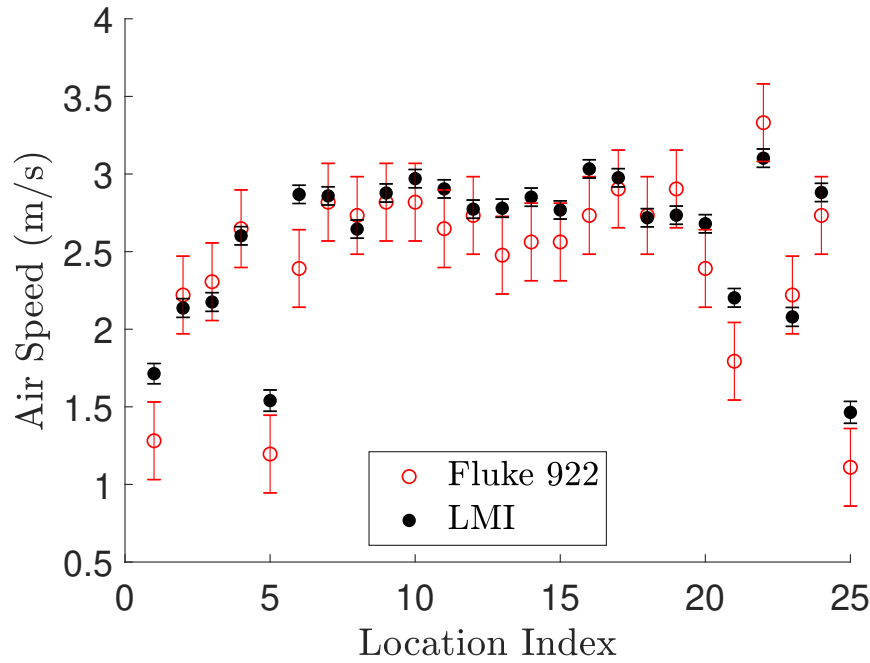


Figure 4.7 – Comparison of velocities measured with LMI and Fluke 922 differential pressure sensors

readings averaged over time on a digital display, which were recorded by hand.

The uncertainties associated with both data sets, denoted by error bars in Figure 4.7, are those reported by the sensor manufacturers, neglecting uncertainty contributed by the pitot tube used for this test. The LMI sensor uncertainty also includes uncertainties associated with the density term and pressure correction factor propagated from the SHT-31D (ambient temperature and humidity) and BME680 (ambient pressure) sensors as discussed in Section E, although this contribution is small.

The results align well, and the differences observed are within the confidence interval of both sensors in 20 out of 25 compared points. Generally, readings from the two sensors tend to disagree slightly in regions of higher velocity (locations 10 through 16), and in the tower’s corners (locations 1, 5, 21, and 25). Flow in the corners is likely disturbed due to the presence of brackets below, otherwise used to support the drift eliminator. In the remainder of this work, due to its high accuracy and convenient integration with LabVIEW, the LMI sensor is be used for all differential pressure measurements used for determining velocity. The LMI is also used for total pressure measurements - the difference between total pressure inside the tower and the ambient lab air - when this differential is sufficiently low. The choice of LMI or Fluke 922 will be stated for all total pressure measurements.

4.1.4 Sensitivity to Sampling Time

Due to the turbulent nature of the air flow within the experimental model, variation is expected in the instantaneous measurements of velocity and total pressure (of which, dynamic pressure is a component) by the LMI sensor. In order to obtain time-averaged results for velocity and pressure in individual locations, the ΔP measurements collected every 30 ms are averaged for the time over which they were collected. To ensure that the differential pressures measured by the LMI did not shift over time or vary with sampling time, an investigation was performed at the fill-low plane of an empty tower (see Figure 4.1); this plane experiences a wide range of velocities and an uneven static pressure profile, making it the most interesting for study with respect to varying turbulent flow effects.

Before being averaged, the readings from the LMI resemble those shown in Figure 4.8. A great deal of noise is apparent at each of the plotted locations. The magnitude of the variation increases with increasing mean velocity up until the mean velocity reaches approximately 5.2 m/s. At velocities higher than this, the maximum pressure drop which the LMI sensor can detect (27.31 Pa) limits the upper bound of noise which can be recorded. This results in erroneous results: a mean velocity which is slightly too low due to consideration of low-bound noise but not high-bound noise, and a deceptively small standard deviation from the mean. Fortunately, the number of locations that measure a velocity higher than 5.2 m/s (such as point C in Figure 4.8) are very few within the scope of this work. For future work in which such high velocities are expected, the median of the LMI readings or a new differential pressure sensor should be considered instead.

The total pressure readings taken with the LMI also experience a varying degree of noise, and these also seem to vary due to turbulence corresponding with mean velocity. Figure 4.8 shows an example of this: although the total pressure reading at point B is higher than that of point A, the noise at point A is notably more extreme than that at point B due to the increased velocity there. Variation at point C is artificially low due to the mean velocity being above 5.3 m/s in that location. The noise in these velocity and pressure readings and its relationship to the local velocity is illustrated by Figure 4.9. The best fit curves in Figure 4.9 were generated excluding the deviation in velocity and dynamic pressure at the two locations for which velocity exceeded 5.3 m/s - these excluded points are shown with red x's. Those best-fit curves are expressed by the following equations:

$$\delta_v = 1.72 \text{ m/s} + 0.125v - 0.06 \text{ s/m} \times v^2, \quad (4.1)$$

and

$$\delta_{\Delta P} = 3.30 \text{ Pa} + 1.38v \frac{\text{Pa} \cdot \text{s}}{\text{m}} - 0.171 \frac{\text{Pa} \cdot \text{s}^2}{\text{m}^2} v^2, \quad (4.2)$$

where δ_v and $\delta_{\Delta P}$ are respective estimates for the standard deviation of air velocity and

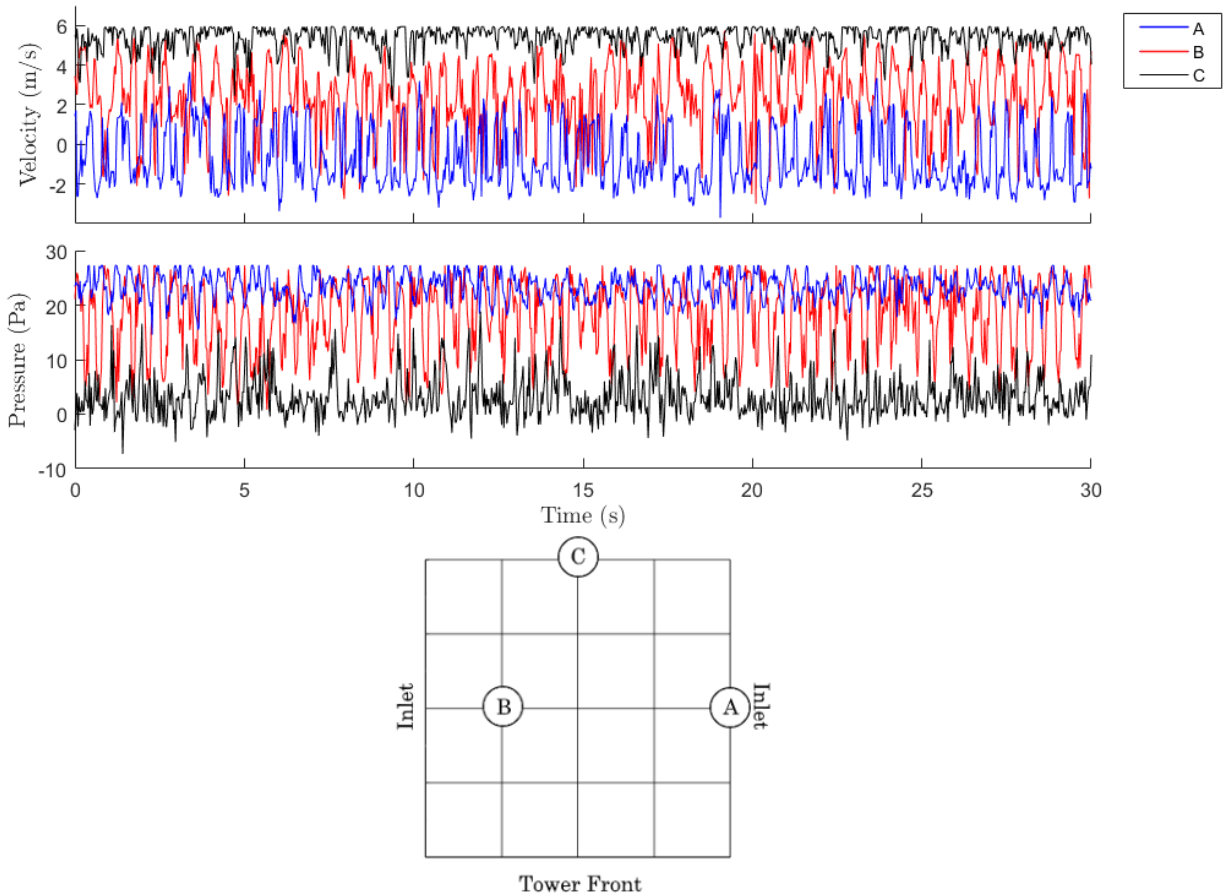


Figure 4.8 – Noise recorded from LMI in velocity and total pressure readings at three locations

measured differential pressure, and v is the mean air velocity. These relationships allow a means to estimate, roughly, the degree of turbulent fluctuation in a given measurement made at a single location. This noise is attributed to turbulence rather than the LMI sensor; the noise associated with the sensor is reported by the manufacturer as only ± 0.01 Pa [40]. The velocity and pressure maps in the sections to follow, namely Sections 4.2.1 and 4.2.2, discuss the mean velocity profiles and do not consider this turbulent fluctuation.

Sampling times over which results were averaged were then varied to ensure that the 5-second sampling time selected for general use in this study was large enough to yield sufficiently repeatable results without significant variation of the mean over time. The velocity and total pressure measured at each location was averaged over 1, 5, 10, and 30 seconds. Results are compared visually in Figure 4.10.

The 1-, 5-, and 10-second results can be compared against the 30-second results, assuming that the data averaged over 30 seconds would yield the most accurate results. A sample deviation can be calculated for each of the three sets, using the 30-second results as a

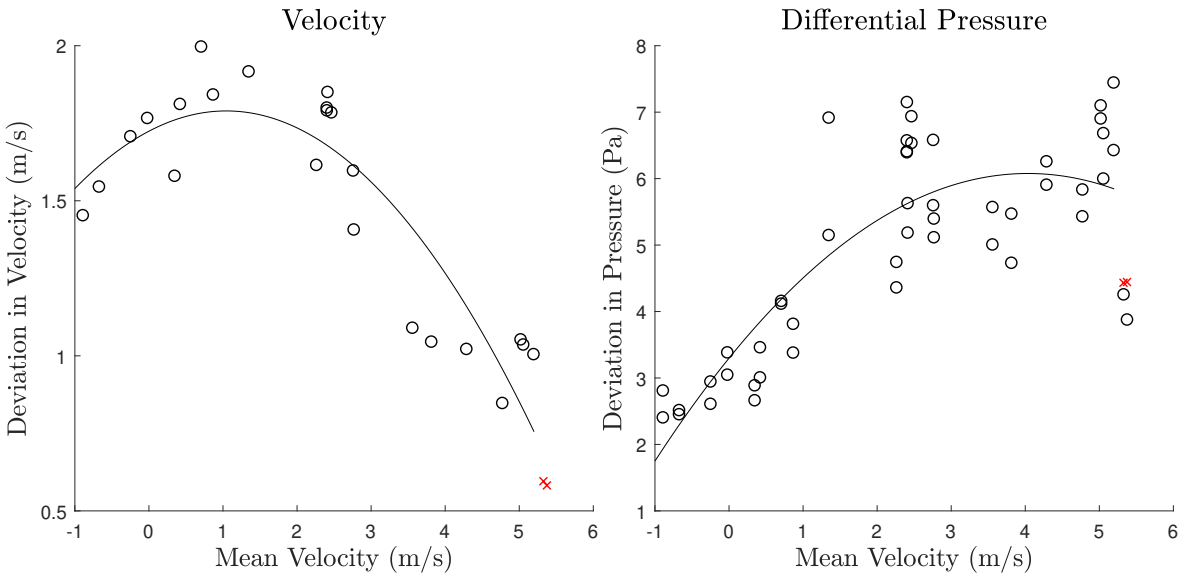


Figure 4.9 – Deviation of differential pressure and velocity with respect to mean velocity “Differential Pressure” includes both total pressure and dynamic pressure measurements taken for velocity measurements. Excluded points shown in red.

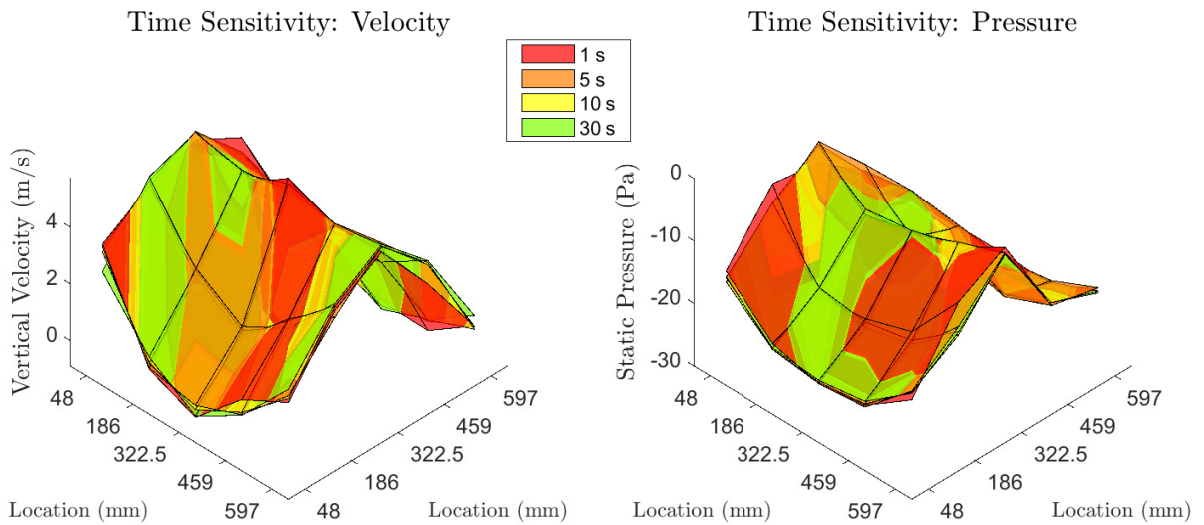


Figure 4.10 – Effect of varying sampling times for pitot tube measurements

Table 4.1 – Sample deviation from 30 s case for varying sampling time, calculated using (4.3)

Sample Deviation from 30 s	10 s	5 s	1 s
Vertical velocity deviation (m/s)	0.25	0.32	0.43
Static pressure deviation (Pa)	0.50	0.78	1.49

reference. This sample deviation is calculated as

$$s_{30} = \sqrt{\frac{1}{N-1} \sum_{i=1}^N (x_i - x_{i,30s})^2}, \quad (4.3)$$

where s_{30} is the deviation from the 30 s measurement, $N = 25$ is the number of measurement points, x is the measured quantity, i.e. either vertical velocity or static pressure, and i denotes different locations in the traverse grid. Results are summarized in Table 4.1.

From Table 4.1, it can be seen that an increase in sampling time improved the agreement of mean velocity and static pressure with the 30 s case slightly, although disagreement was small throughout. Although 30 s measurements may provide the most accurate readings, performing an experiment using this sampling time is very time-consuming and proved impractical. Ultimately, 5-second samples were selected as a compromise between precision and practicality for pitot tube measurements.

4.1.5 Repeatability

To quantify the precision of the 160F pitot tube traverse measurements taken under the same experimental conditions, a set of five repeatability experiments were conducted similar to those detailed in Section 4.1.4. A 5-second sampling time was used, and all experimental conditions were kept constant. Ambient conditions varied little, but were measured and accounted for in each case. Results are compared in Figure 4.11.

A sample standard deviation was computed for both vertical velocity and static pressure measurements using

$$s_{\text{mean}} = \sqrt{\frac{1}{MN-1} \sum_{j=1}^M \sum_{i=1}^N (x_{ij} - \bar{x}_i)^2}, \quad (4.4)$$

where s_{mean} is the deviation from the mean of the five measurements, M is the total number of identical experiments performed, and j is an index for each experiment. The sample deviation from the mean for vertical velocity was computed as 0.380 m/s, and for static pressure as 1.2 Pa. The standard deviations for each of the 25 sampling locations inside

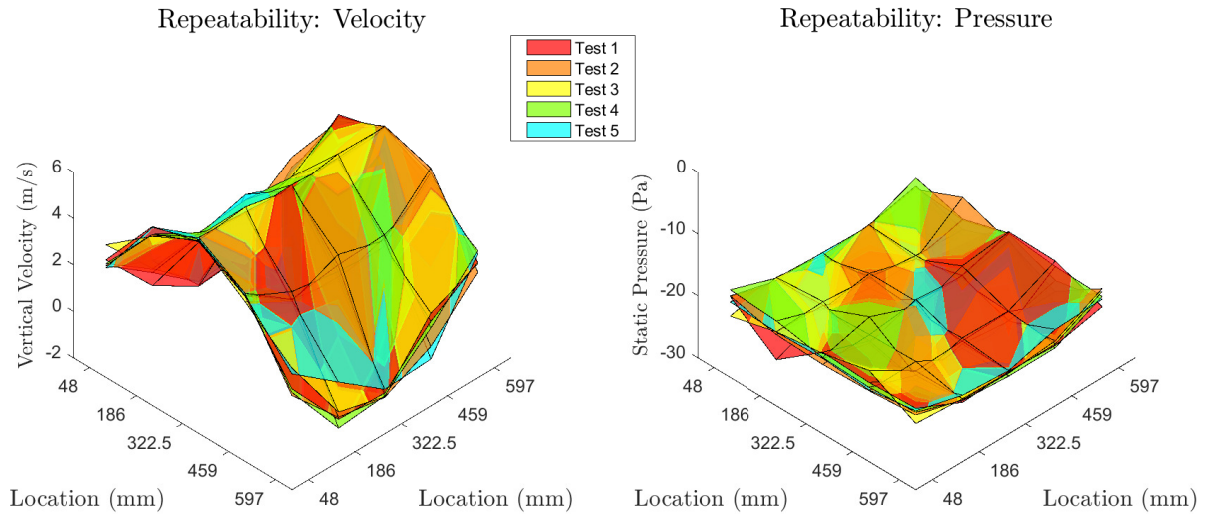


Figure 4.11 – Repeatability of pitot tube measurements

the tower are combined into one overall standard deviation because no relationship was apparent between deviation and location or velocity. Therefore, generally speaking, 68% of measured velocities will fall within ± 0.4 m/s of the mean velocity, and 68% of measured pressure drops will fall within ± 1 Pa of the mean static pressure. Taking two standard deviations, 95% of measured velocities will be within ± 0.8 m/s of the mean velocity - similar to Dwyer’s suggested accuracy of ± 0.9 m/s. Likewise, 95% of measured pressure drops will fall within ± 2 Pa of the mean measured static pressure. These precision errors are much more significant than the uncertainties presented relating to comparison between 160F and L-pitot tube, asymmetry, and sampling time. Therefore, it is these precision errors which will be applied as uncertainty in the results to follow, in particular, in velocity maps and pressure maps measured with the 160F pitot tube and LMI sensor.

4.1.6 K-Factor for Averaging Pitot Tube

The role of the STRA averaging pitot tube is to measure the overall air flow rate downstream in the ductwork, undisturbed by local disturbances in the cooling tower itself. Comparing the area-averaged 160F pitot tube results for air velocity in an empty tower with those collected from the STRA averaging pitot tube installed in the ductwork above the lab-scale cooling tower, the two air flow rates did not match, as shown in Figure 4.12. The manufacturer’s calibration factor was used for both the 160F and STRA pitot tubes in this comparison.

Because the 160F calibration factor was validated when it was used in comparison with the L-pitot tube in Section 4.1.1, the discrepancy is believed to come from flaws in the STRA averaging pitot tube setup:

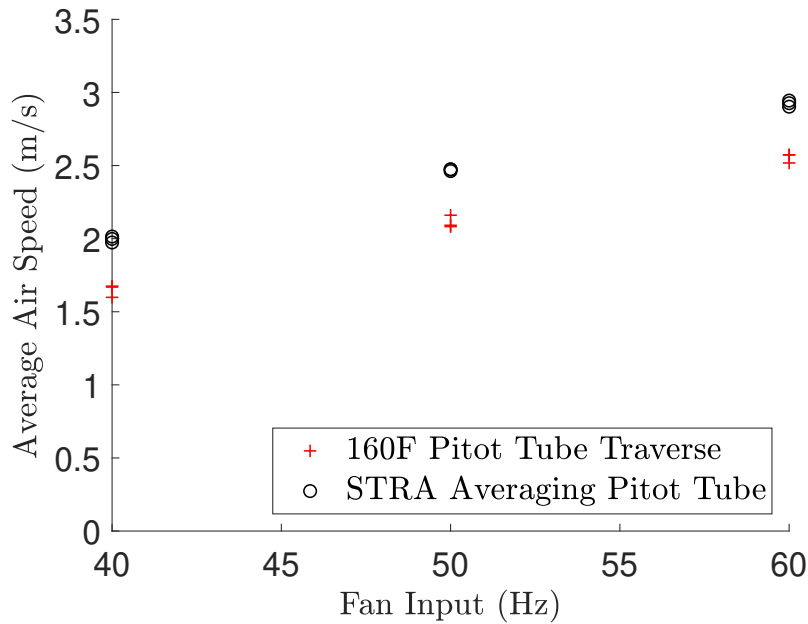


Figure 4.12 – Disagreement between STRA and 160F using manufacturer equations

- The averaging pitot tube assembly is installed in the best location available, but air flow may be unevenly distributed through the duct cross section despite the honeycomb grid upstream. In addition, the discrepancy between the STRA readings and traverse-measured velocities varies depending on how components such as fill are arranged inside the cooling tower.
- The standard arrangement for this averaging pitot tube has the take-off ports on the side. From these ports, tubing would connect to a differential pressure gauge. The STRA installed in this setup, by contrast, has these takeoff ports connecting to the centreline of the assembly at the centre of the duct, as shown in Figure 4.13. Averaging pitot tubes are criticized for over-representing the measurement points located closest to these takeoff points [41], in this case leading to a higher overall “average” velocity, which is consistent with the trends exhibited for all three fan speeds of Figure 4.12.

Therefore, the manufacturer’s equation and the calibration constant K , which is obtained for the arrangement with takeoff ports on the side, is likely unsuitable for this particular arrangement. In order to use the STRA readings as a good approximation of overall air flow rate regardless of the cooling tower configuration, a new empirical constant was determined by fitting the pressure drop measured in the STRA to the trusted velocity measured in the cooling tower using the 160F pitot tube.

To obtain a fitting constant which would yield satisfactory results for any experiment, the STRA ΔP and velocity traverse data were collected for a wide variety of cooling tower



Figure 4.13 – Dwyer STRA averaging pitot tube installed in experimental model
 Left: STRA interior, including sampling tubes, takeoff ports (taped-over), and honeycomb flow-straightener. Right: STRA as installed in ductwork, outlined in red.

configurations:

- Empty tower at five fan speeds, repeated three times each
- Full tower (120 cm of fill, nozzle assembly, and drift eliminator) at four speeds
- 120 cm of fill with drift eliminator directly on top at one speed
- 120 cm of fill at four speeds, with two traverses taken at two different planes
- 60 cm of fill at four speeds
- 60 cm of fill installed at a higher elevation at four speeds
- 90 cm of fill installed at a higher elevation at four speeds
- 30 cm of fill at four speeds

The average velocity is found using multiple pitot tube measurements following ASHRAE’s guidelines for a duct traverse. Using this method, the 25 points at which velocity readings are taken are distributed through the duct cross section using the Log-Tchebycheff rule, resulting in 25 velocity measurements which can be arithmetically averaged to yield the average velocity through the entire duct area [36]. Velocity traverses which included areas of negative velocity (recirculating, stagnant air) were rejected in the interest of including only high-quality average velocities in the determination of the STRA K factor.

Assuming the data conforms to the standard equation for dynamic pressure losses,

$$v = K \sqrt{\frac{2\Delta P_{\text{corr}}}{\rho}}, \quad (4.5)$$

where v is the average velocity in the tower measured by the traverse, K is a dimensionless fitting constant, ΔP_{corr} is the pressure drop across the STRA measured by the LMI corrected for ambient pressure (as per the sensor datasheet), and ρ is the density of air. The corrected ΔP_{corr} can be found as follows:

$$\Delta P_{\text{corr}} = \Delta P_{\text{measured}} \frac{100000 \text{ Pa}}{P_{\text{ambient}}}, \quad (4.6)$$

where $\Delta P_{\text{measured}}$ is the pressure drop measured directly by the LMI sensor, and P_{ambient} is the measured ambient pressure.

In this case, v is measured using the 160F pitot tube, $\Delta P_{\text{measured}}$ is measured from the STRA (both using the LMI), and the remaining ambient conditions are measured by the SHT and BME sensors. Note that the STRA and 160F measurements could not be taken simultaneously. In other words, a particular measurement point may be shown to yield $v = 1.1 \text{ m/s}$ for a $\Delta P_{\text{measured}}$ of 1.5 Pa , but these measurements were not taken simultaneously and do not necessarily correspond exactly, although they were collected at the same fan speed, and for the same cooling tower configuration.

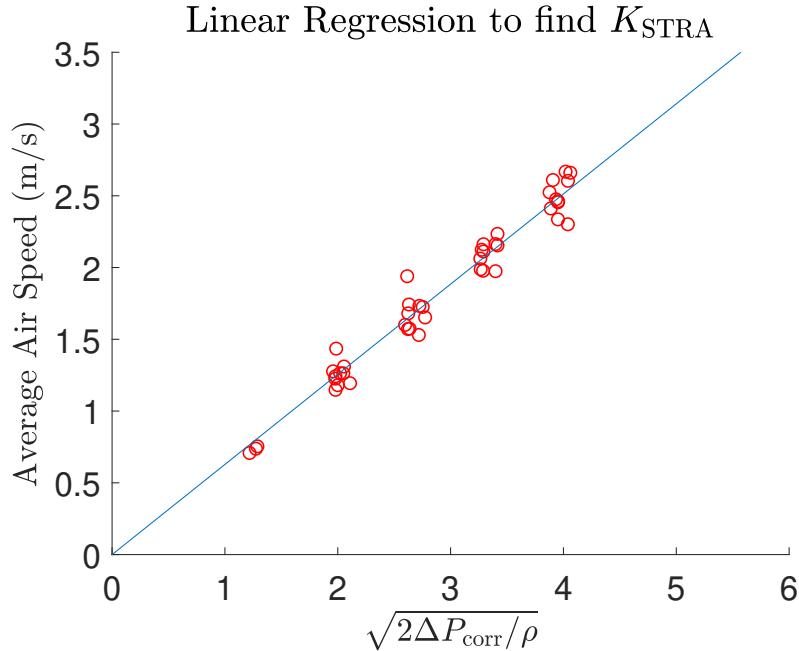


Figure 4.14 – K -factor ($K = 0.628$) fit to experimental data

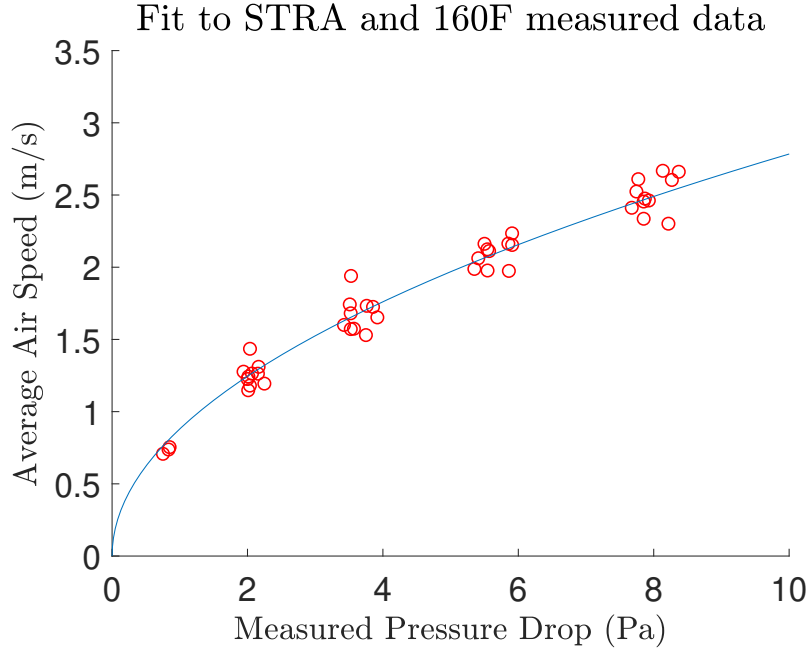


Figure 4.15 – Fit of 0.628 K -factor to experimental data

K was found from (4.5) using a simple linear regression approach making sure to intercept the origin. The slope of the line in Figure 4.14 was found to be 0.628. Therefore, expanding on (4.5),

$$v = 0.628 \sqrt{\frac{2\Delta P_{\text{corr}}}{\rho}}. \quad (4.7)$$

Applying this new K to a plot of v versus $\Delta P_{\text{measured}}$ in Figure 4.15 shows that this equation fits quite well with experimental data on average, but may over- or under-predict by up to 0.2 m/s (as explained below) depending upon the particulars of the tower configuration.

Using the same methodology but only including empty tower results, a K factor of 0.639 was found which could be used to obtain very reliable velocity measurements from the STRA, with much less scatter than shown in Figures 4.14 and 4.15. This K factor should be used only for empty tower tests.

Repeating the procedure again for the tower configurations in which at least one fill element is included yielded a K factor of 0.624, but with a similar amount of scatter as in Figures 4.14 and 4.15. Either 0.624 or 0.628 as a K factor will yield reasonable average air velocities for a cooling tower containing fill or similar elements, however this fitted value, and STRA-derived data more generally, should be used only as an approximation of the true average velocity when a high-quality traverse measurement of velocity is not possible.

The standard deviation of this set of data from the velocities predicted by (4.7) can be

computed using

$$\delta_K = \sqrt{\frac{1}{N-1} \sum_{i=1}^N \left| v_{\text{traverse},i} - K \sqrt{\frac{2\Delta P_{\text{measured},i} * 100000}{\rho_i P_{\text{ambient},i}}} \right|^2}. \quad (4.8)$$

A standard deviation of 0.1 m/s was computed from this relation with respect to the experimental data used to define its K value. Note that the experimental data used in this relation was not selected randomly, rather, it was a selection of data from 44 different dry cooling tower experiments conducted for various other purposes as listed above. The velocities measured with the STRA and interpreted using this relation can be trusted to ± 0.2 m/s with 95% confidence.

4.2 Velocity and Pressure Maps

Using the pitot tube and differential pressure sensors, the interior of the lab-scale cooling tower was mapped out in terms of static pressure and vertical air velocity. Constructing these maps for various cooling tower configurations revealed the locations of stagnant areas, local maxima and minima, and the static pressure loss generated across each major feature of the tower.

4.2.1 Empty Tower Maps

The first set of velocity and pressure maps were taken with a dry, empty tower. The experimental model had all of its internal components removed, save for support structures such as brackets. While not immediately applicable for comparison with a true cooling tower, this scenario allowed for

1. Measurement of data for comparison with results from a simple CFD simulation, and
2. Identification of the changes to the velocity and pressure profiles contributed by specific components once they were added back into the tower.

Velocity was found from dynamic pressure, which was measured using the Dwyer 160F pitot tube coupled with the LMI differential pressure sensor. The differential pressure reading was corrected, considering the local ambient pressure as shown in (4.6). LMI readings were taken for and averaged over five-second periods at each location in the 25-point grid shown in Figure 4.2. One experiment was performed for each fan speed. The velocity was calculated considering the air density determined from pressure, temperature, and humidity measured in the laboratory, and the equation provided by Dwyer:

$$v = C_p \sqrt{\frac{2P_d}{\rho}}, \quad (4.9)$$

where v is the air velocity, C_p is the pitot tube coefficient 0.81, P_d is the dynamic pressure, and ρ is the air density. Based on previous studies from Section 4.1.5, the uncertainty in v is believed to be ± 0.8 m/s, and the uncertainty in P_s is believed to be ± 2 m/s.

The static pressure was determined by measuring total pressure and subtracting the dynamic pressure from it at each of the 25 locations in each cross section. Note that hydrostatic pressure was not measured in this setup, and because it does not drive flow, it has not been added to the presented measurements and will not be considered further. Total pressure was found using the LMI sensor, measuring the pressure difference between the ambient lab air and the total pressure port of the 160F pitot tube. As was done with velocity measurements, total pressure measurements were taken in the 25-point grid shown in Figure 4.2. The cross sections sampled are shown in Figure 4.1, along with the labels by which they will be referred to in this chapter.

The velocity and static pressure maps are shown in Figures 4.16 through 4.20. Figure 4.16 shows vertical air velocity maps superimposed over a rendering of the experimental model in order to indicate their approximate location in three dimensional space. In Figure 4.16, zones of stagnant, recirculating air are seen to form above the two air inlets on opposite sides. In this empty-tower scenario, the recirculation zones begin immediately above the top edge of the inlet, then grow wider before they begin to disappear approximately 60 cm above the top of the inlet. In Figure 4.17, the upward-flowing air is clearly affected by these recirculation zones. Where the recirculation zones grow wider, the upward-flowing air is effectively confined to a smaller cross-section, and the maximum velocity is observed along the centerline. As the recirculation zones recede, the velocity profile begins to even out, and local maxima are observed not in the center but on the front and back faces. These elevated velocities on the front and back faces of the cooling tower continue upward, but even out with the rest of the bulk velocity by the time the air reaches the plenum plane.

As the fan speed is reduced, the airflow likewise decreases. Figures 4.18 through 4.20 show gradual reductions in the maximum air speed and maximum static pressure drop, relative to the local maxima observed in 4.17. A slight loss in air velocity in the plenum plane is observed in the corners in most of these figures, likely due to the presence of small brackets mounted upstream. The brackets which normally support the fill are located between the rain zone and fill-low planes, and these likely have an effect on the flow in those regions as well, i.e., by modifying the shape of the recirculation zone).

Static pressure is relatively uniform through each cross section except for the rain zone plane where lower magnitudes are observed along the centerline, while higher magnitudes are

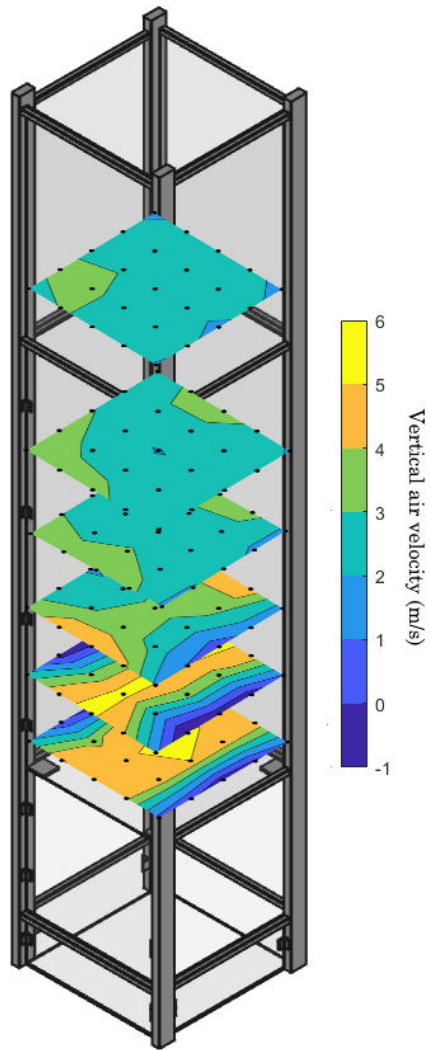


Figure 4.16 – Vertical velocity map in a 3D tower: empty tower, 60 Hz

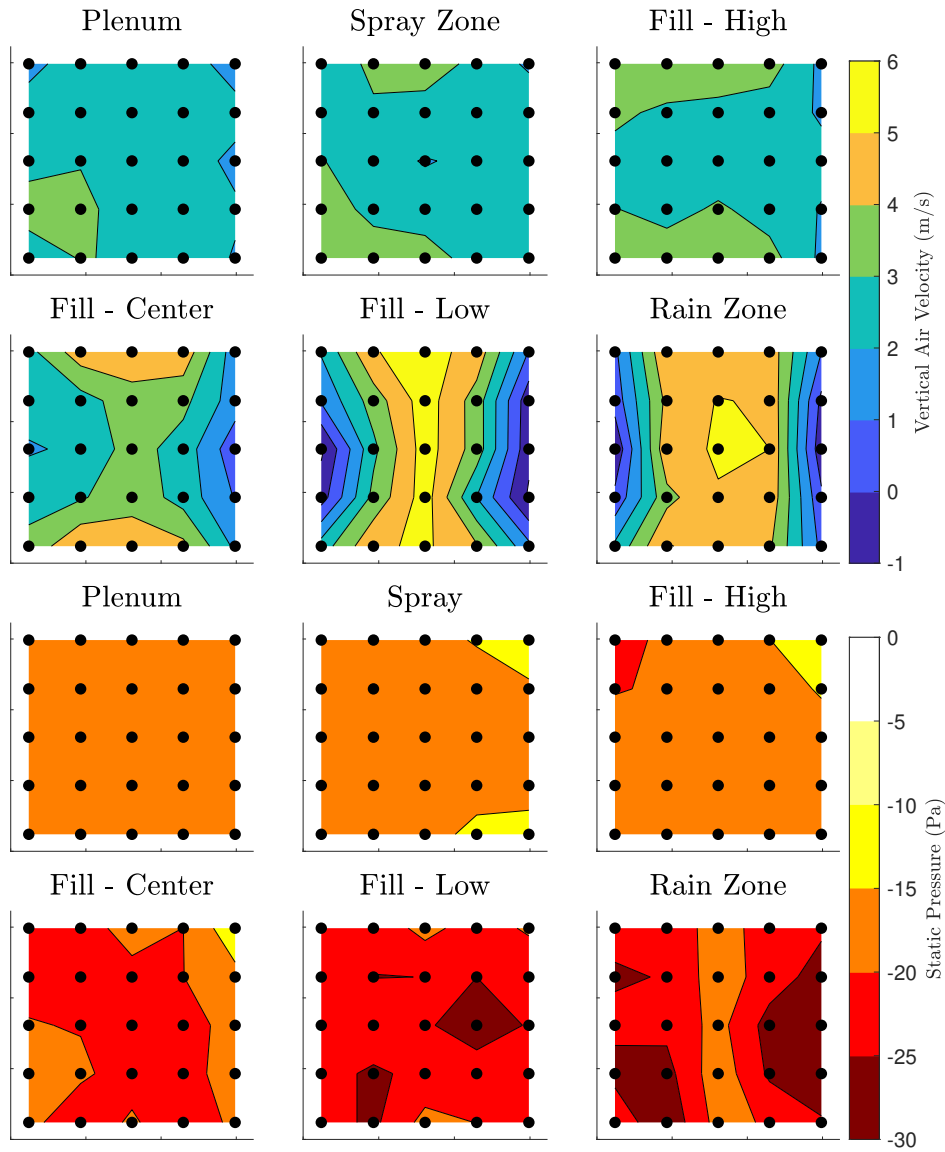


Figure 4.17 – Vertical velocity and static pressure map: empty tower, 60 Hz, $v_{av} = 2.7$ m/s

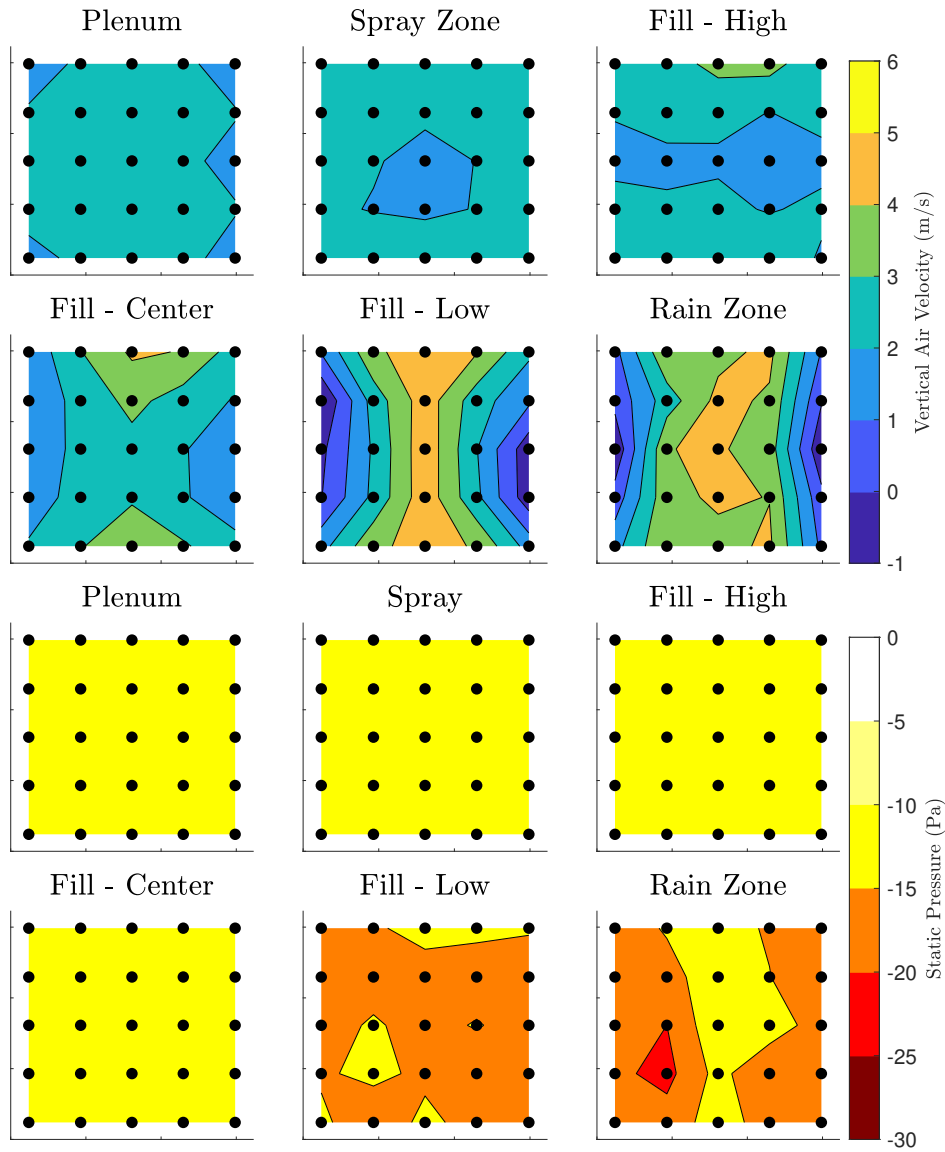


Figure 4.18 – Vertical velocity and static pressure map: empty tower, 50 Hz, $v_{av} = 2.3$ m/s

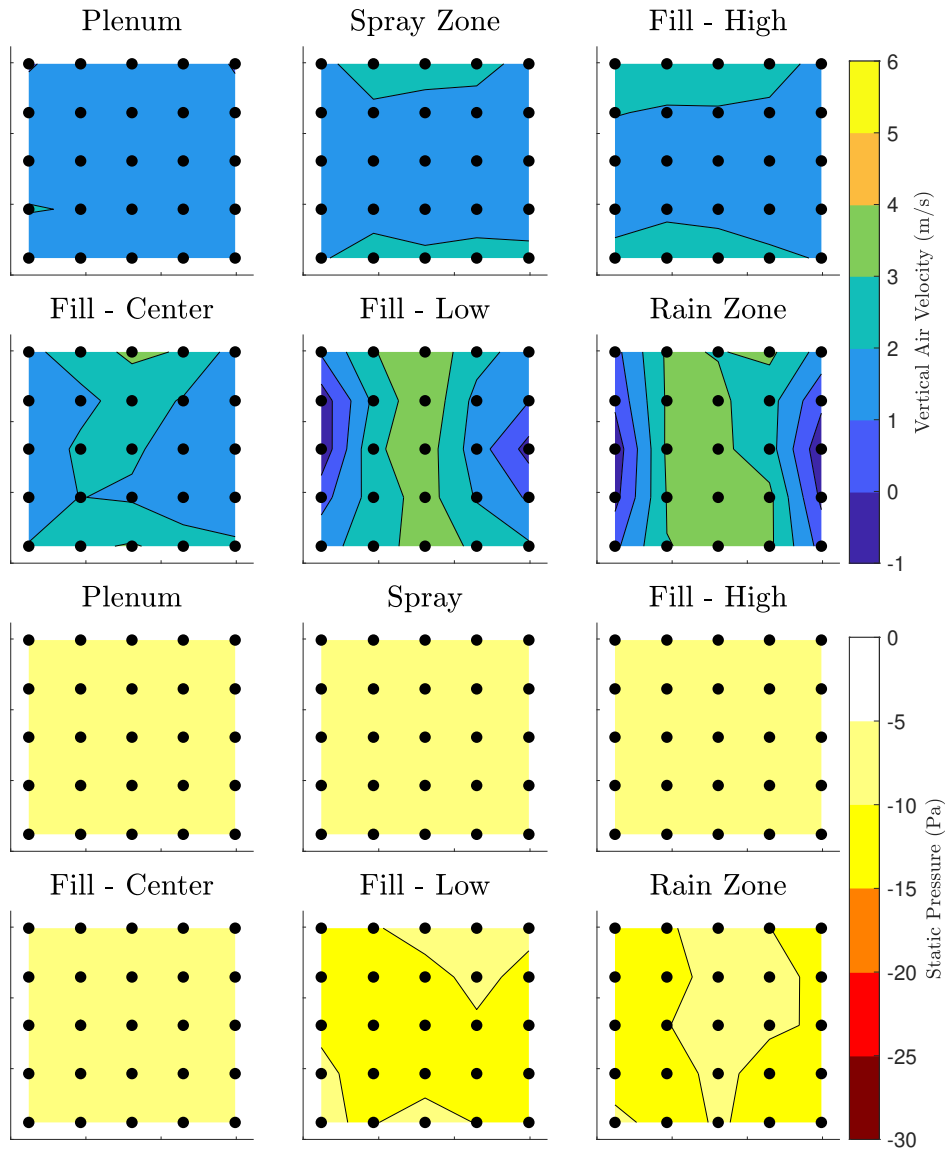


Figure 4.19 – Vertical velocity and static pressure map: empty tower, 40 Hz, $v_{av} = 1.8$ m/s

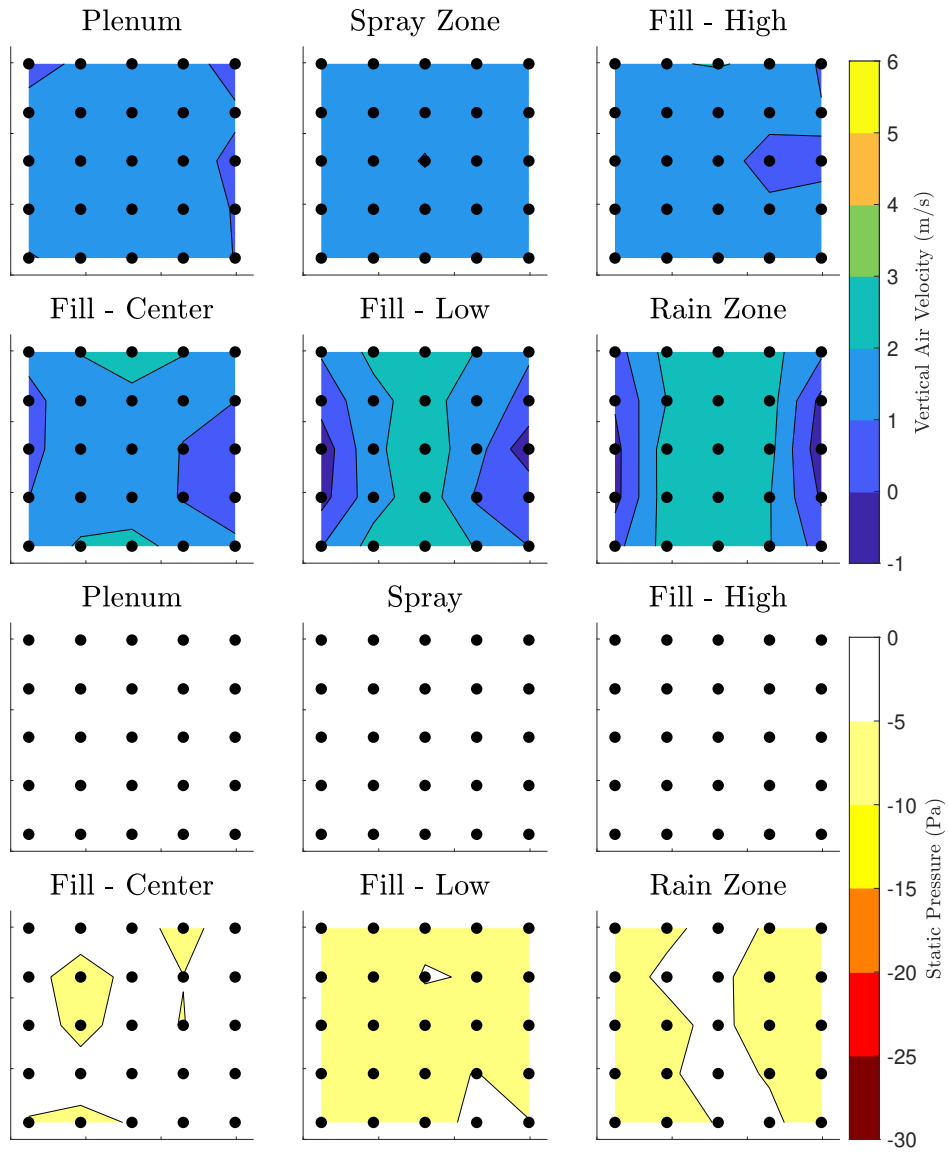


Figure 4.20 – Vertical velocity and static pressure map: empty tower, 30 Hz, $v_{av} = 1.4$ m/s

Table 4.2 – Empty tower flow rate and static pressure drop summary

Fan Input (Hz)	\dot{m}_{av} (kg/s)	v_{av} (m/s)	ΔP_s (Pa)
60	1.2	2.7	17
50	1.0	2.3	12
40	0.83	1.8	8
30	0.61	1.4	4

observed on the sides facing the inlets. In the rain zone and fill-low planes, the recirculation zones restrict the portion of the tower cross-section available to the upward-flowing air. Above these planes, the recirculation zones are not present, and the expanded effective area causes a small increase in static pressure akin to a diffuser. Above the fill-center plane, very little change in static pressure is observed, confirming that most static pressure losses in the empty tower are due to effects in the inlet region.

Table 4.2 summarizes the average air flow rates at each fan setting, along with the average static pressure measured at the plenum plane with reference to the ambient air in the laboratory. While empty, the maximum velocity of air within the tower is 2.7 m/s, producing a maximum pressure drop of 17 Pa overall (not including local maxima in the inlet region). This pressure drop is somewhat small in comparison with the pressure drops that will be expected from fill and other components, but is not negligible. Additionally, disturbance of airflow and losses created by inlet effects have been well illustrated in Figures 4.17 through 4.20, and will continue to be significant in other tower configurations.

4.2.2 Full Tower Maps

Another set of velocity and pressure maps were created for a dry tower including all of its standard components:

- Two layers of fill (4 ft or 120 cm in total)
- Spray nozzle assembly (the BETE NC 2065 nozzle, in this case)
- One layer of drift eliminator

The same procedure was followed as for the empty tower, although the traverse planes which are blocked by the presence of the fill (fill-low, fill-center, and fill-high) could not be sampled. In addition, the pressure drops generated in this configuration were large enough that the range of the LMI sensor was insufficient - therefore, the Fluke 922 airflow meter was used instead to measure pressure. Similar to what was done for the empty tower case, the total pressure drop between the ambient lab air and the grid point locations was measured with

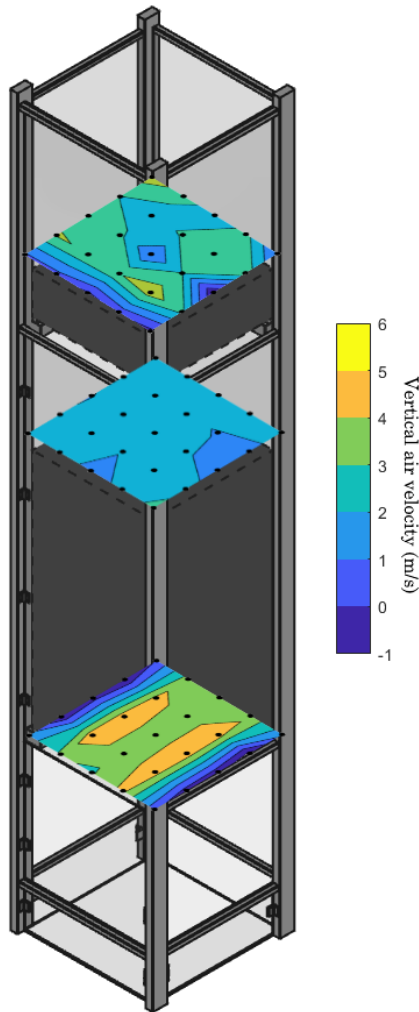


Figure 4.21 – Vertical velocity map in a 3D tower: full (dry) tower, 60 Hz, $v_{av} = 2.2$ m/s

the Fluke 922, and the dynamic pressure calculated from the velocity measured with the LMI sensor was subtracted from this to determine the static pressure at the same point. Figure 4.21 shows the velocity maps superimposed on a rendering of the experimental model to give an impression of where the measurements were taken in three dimensional space.

In contrast with the empty tower case, the rain zone plane traverse in Figure 4.21 shows two zones of peak velocity separated by a band of lower velocity in the center. The velocity map in the spray zone is remarkably even, lending credence to the idea of the fill as a homogenizing and flow-straightening element. Above the drift eliminator, the velocity map has a number of interesting features. The very center of the map includes a local minimum for velocity, due to the presence of the spray nozzle located under the drift eliminator in this location. Along the right-hand side, a stagnant zone of recirculating air forms where

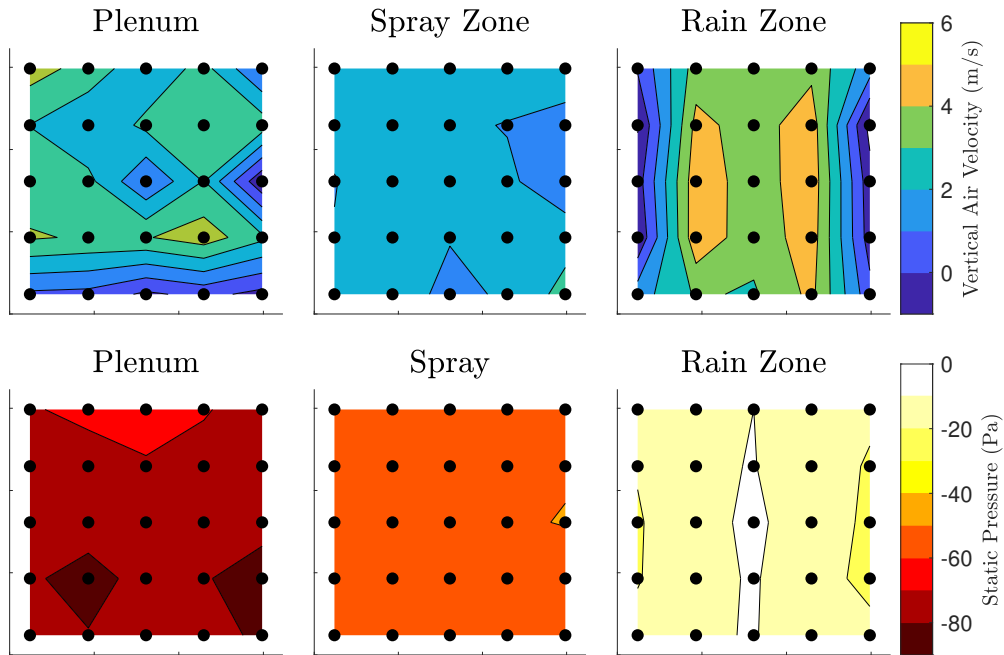


Figure 4.22 – Vertical velocity and static pressure map: full tower, 60 Hz, $v_{av} = 2.2$ m/s

the last curved sheet of plastic that comprises the drift eliminator meets the wall. Along the front face of the tower, another zone of stagnant air forms, due to the interior geometry of the drift eliminator. By design, air does not leave the drift eliminator in a purely vertical direction, and the angle of this airflow can generate small zones of recirculation where the drift eliminator meets a wall and directs air away from it.

The static pressure maps are again largely uniform across each section, except for in the rain zone where some systematic variation in the static pressure drop is evident from Figures 4.22 and 4.23. Accordingly, there is a slightly elevated static pressure drop along the sides facing the inlets, reducing towards the centerline. In this tower configuration, the most significant source of static pressure loss is the fill - this can be seen in Figure 4.26, which shows the increasing loss in static pressure as air passes through subsequent components. The error bars in Figure 4.26 are uncertainties in the average static pressure, calculated using (E.22) described in Appendix E Section E.5.

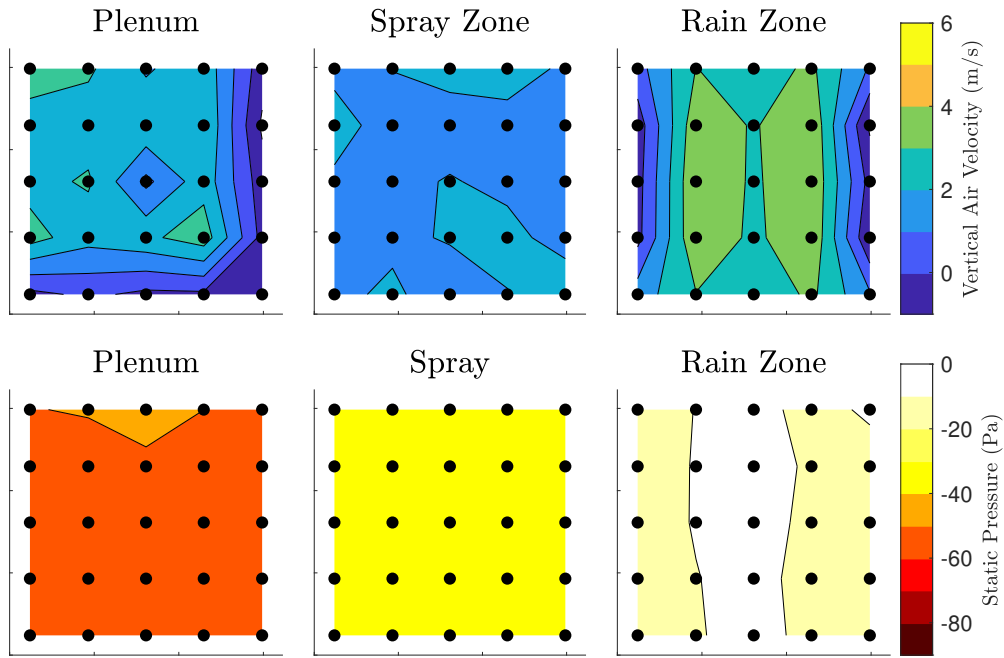


Figure 4.23 – Vertical velocity and static pressure map: full tower, 50 Hz, $v_{av} = 1.9$ m/s

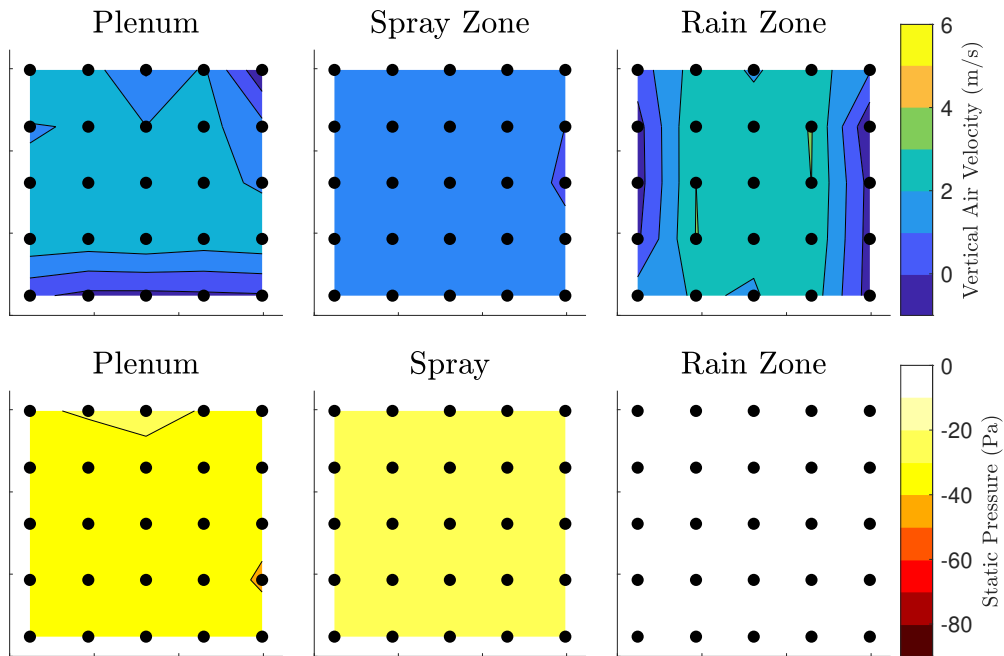


Figure 4.24 – Vertical velocity and static pressure map: full tower, 40 Hz, $v_{av} = 1.5$ m/s

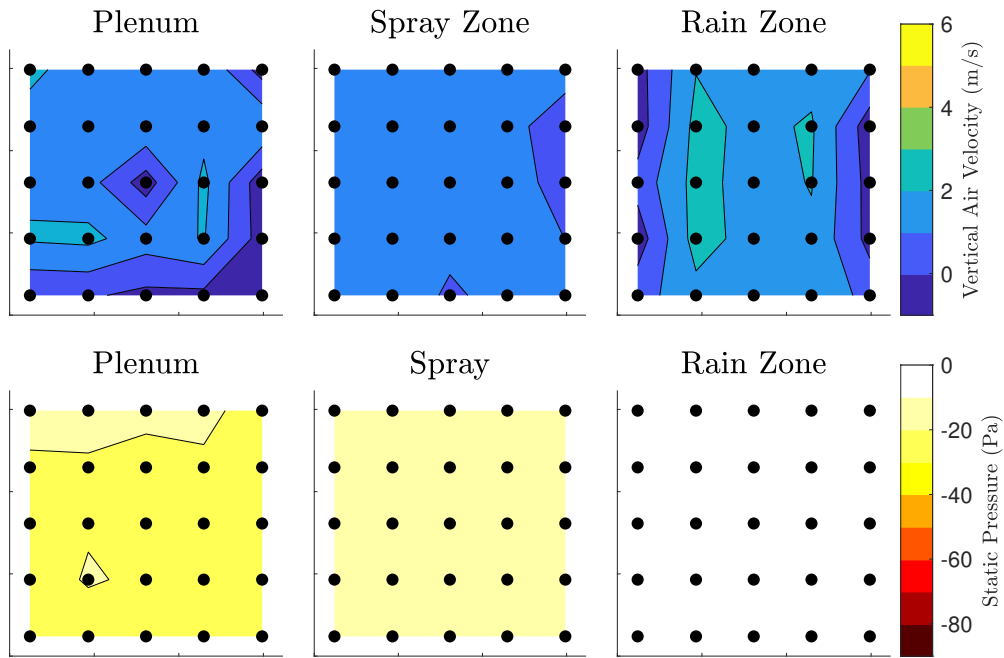


Figure 4.25 – Vertical velocity and static pressure map: full tower, 30 Hz, $v_{av} = 1.2$ m/s

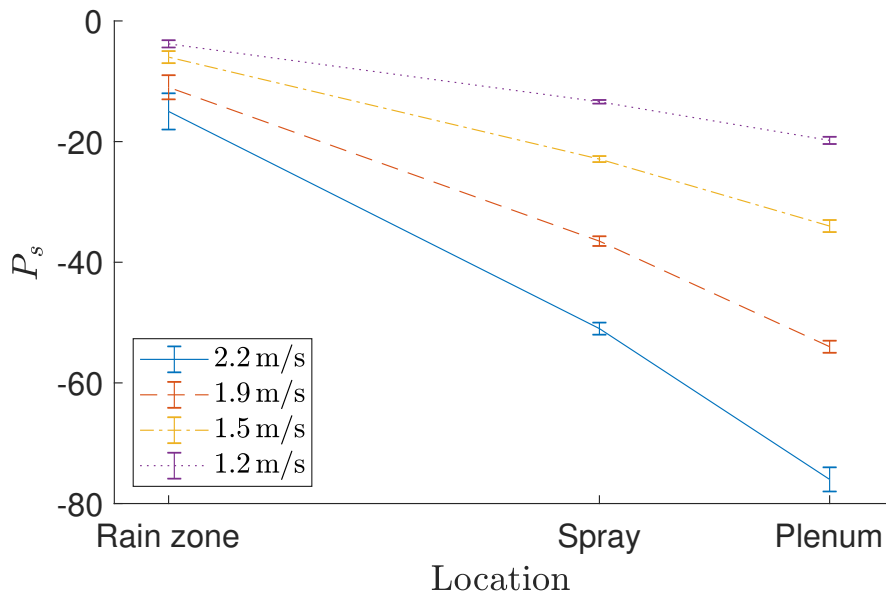


Figure 4.26 – Static pressure drop through a full, dry tower at varying air flow rates

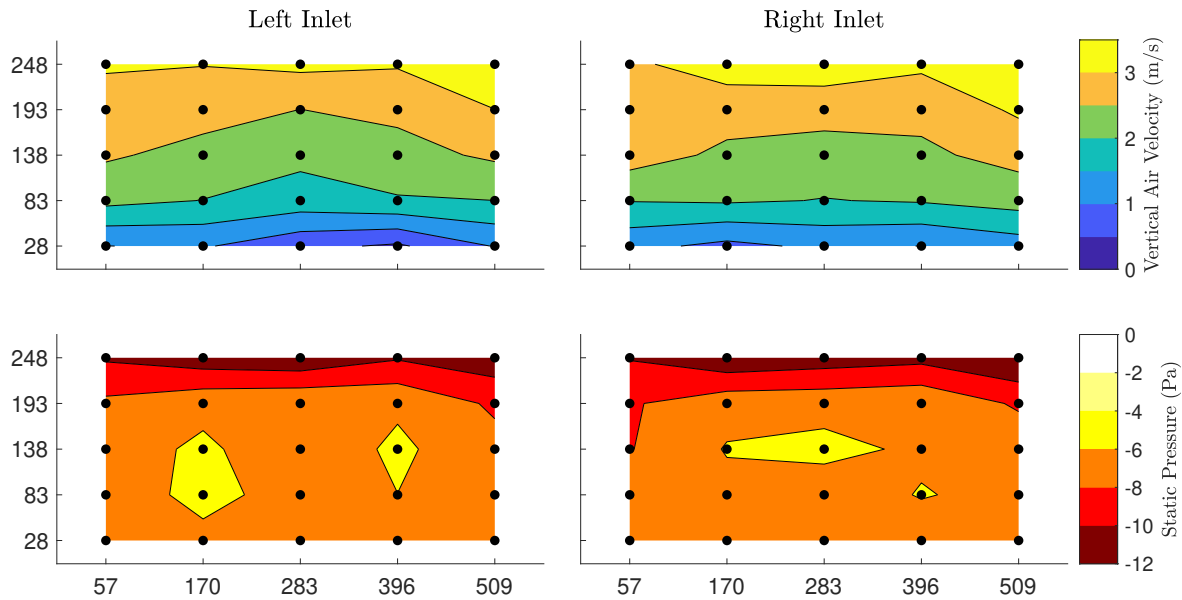


Figure 4.27 – Inlet normal velocity and static pressure map: full tower, 60 Hz

4.2.3 Inlet Maps

A traverse of the inlets to the left and right of the cooling tower was also performed with the full-tower configuration. The inlet area was broken down into 25 equal-area zones with a single measurement point at the center of each one, as opposed to the log-Tchebycheff rule distribution of traverse points used to distribute sampling points within the tower. The pitot tube was oriented so as to sample the flow entering the inlet normal to the inlet face. Results are shown in Figure 4.27.

The speed of the air is highest near the top of the inlet, and decreases gradually towards the bottom. By extension, the pressure map shows fairly uniform pressure across the inlet face except towards the top, where increased suction is observed. The two inlet faces are not identical, likely due to obstructions to the flow field a short distance away from the tower associated with, for example, the sump tank. The right inlet has an average face velocity of 2.71 m/s while the left inlet has an average face velocity of only 2.57 m/s.

4.3 Static Pressure Drop

The loss of static pressure contributed by each component in the cooling tower has a direct effect on the power required by the fan to drive airflow, and thus a direct effect on cooling efficiency. Static pressure loss is often measured experimentally by the manufacturers of major components such as the fill and drift eliminator. The experimental facility developed

in this thesis provides the opportunity to not only measure fill and drift eliminator losses independently, but to quantify losses associated with tower geometry (especially the inlet), and to make note of the cumulative (possibly nonlinear) pressure drop of multiple components and features.

4.3.1 Fill

In taking velocity and pressure maps of the full tower, it became apparent that the fill is not only a source of static pressure loss, but is also a flow-straightening and flow-homogenizing element with respect to air. Downstream of the fill, the air velocity profile is smooth and almost entirely uniform. The presence of the fill also alters the air flow patterns below it, resulting in a velocity profile in the rain zone with two peaks rather than a single peak along the centerline. Therefore, to characterize the static pressure drop associated with the fill, the pressure loss associated with the fill height must be considered in addition to end effects generated by the cooling tower geometry in the regions above and below the fill. Because of the dramatic effect of the fill's presence on the flow field exterior to it, these end effects are not equal to the empty tower's static pressure losses identified in Section 4.2.1.

Data was collected using a procedure similar to that described for the full tower pressure and velocity maps. Ambient conditions were recorded to determine air density, 25-point velocity traverses were performed above and below the tested fill section, and the total pressure difference between the same 25 traverse points and the ambient lab air were measured. The Fluke 922 and LMI sensors were both used to measure total pressure depending upon the magnitude expected in a particular experiment. Because total pressure is very uniform above the fill section (as shown from the results in Section 4.2), total pressure measurements above the fill were sometimes measured in a 5-point traverse through the centerline rather than the full 25-point array.

A general power relation shall be used to relate the measured pressure drop to air speed, i.e.,

$$\Delta P_s = av^b, \quad (4.10)$$

where ΔP_s is the static pressure, and v is air velocity. Figure 4.28 shows the measured pressure drop data along with best-fit lines of the form given in (4.10). Empirical constants a and b are determined by linear regression for each fill height as given in Table 4.3. The b constants are generally close to 2.0, which is expected given that such losses are generally regarded as proportional to dynamic pressure. The a constants clearly increase with H_{fi} , but not linearly.

The measured pressure drops varied from those reported by the fill manufacturer, although the discrepancy reduced with increased fill height. Brentwood's correlation for the

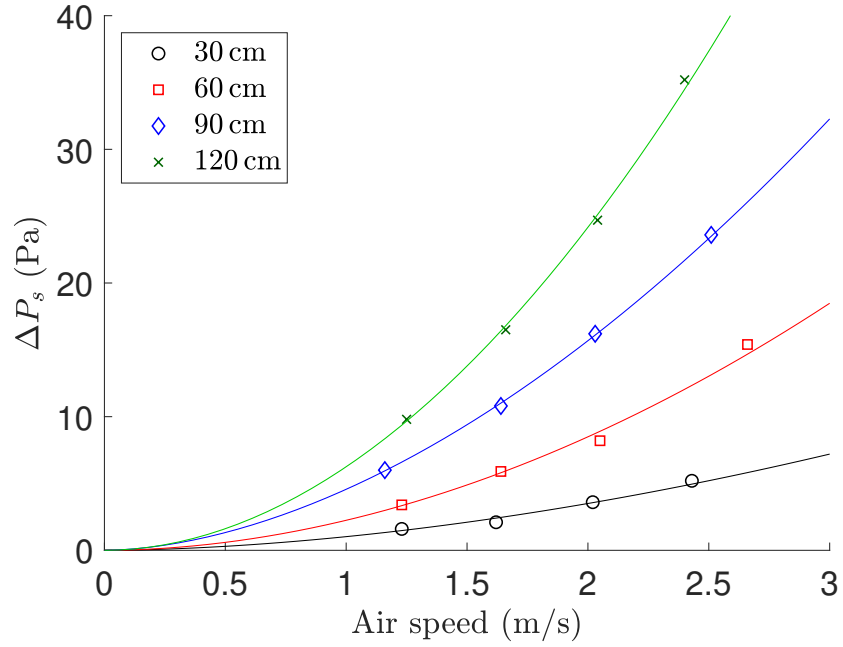


Figure 4.28 – Static pressure drop versus air speed for various fill heights

Table 4.3 – Fill pressure loss constants

Fill Height, H_{fi} (m)	a	b
0.30	1.02	1.78
0.60	2.25	1.92
0.90	4.56	1.78
1.20	6.25	1.95

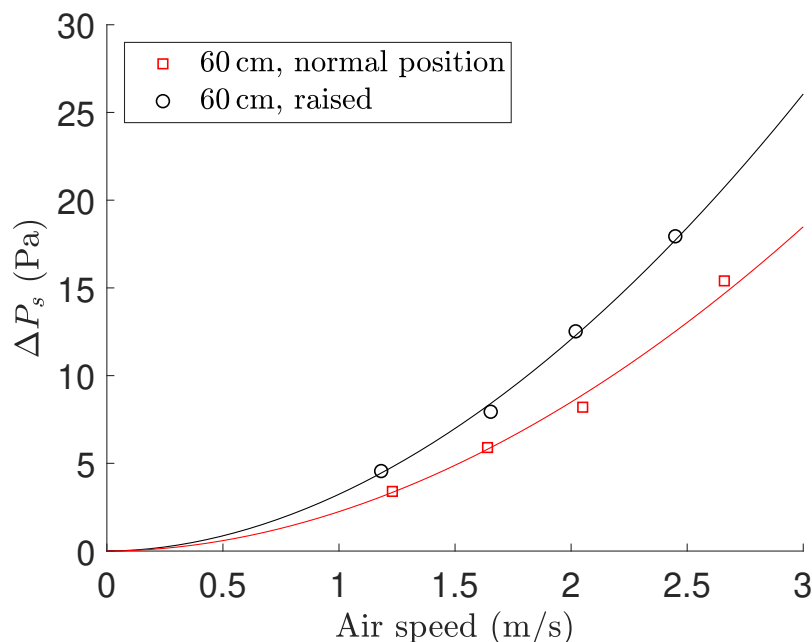


Figure 4.29 – Comparison of pressure drop across fills in standard case, raised case

pressure drop of the OF21MA fill is not shown within this work due to copyright, but can be accessed with authorization from Brentwood Industries through their Document Center [42]. The pressure at the entrance of the fill is affected by inlet effects, which contribute significantly to pressure drop at low fill thicknesses (especially when the fill is in close proximity to the inlet). Both the results shown here and Brentwood’s are likely influenced by such inlet effects, but as the fill thickness grows, i.e., fill losses start to dominate, the results become more similar to one another.

To test the hypothesis regarding interference from inlet effects, a set of experiments was performed on a 60 cm section of fill raised up beyond the recirculation zones which appear above the inlets. The same procedure was followed as for the previous set. A comparison between the raised fill and normal configuration is shown in Figure 4.29. The results measured for the raised section of fill are notably higher. Therefore, the proximity of the fill and the inlet has a significant effect on the pressure drop measured across it, and the disagreement is likely due to differences in inlet effects between the two testing facilities. These results confirm the notion that static pressure drops across different features in close proximity cannot be simply superposed, even for a configuration as simple as this one. For purposes of measuring the pressure drop across fill in isolation, it is recommended that increased height or a flow straightener be added between the air inlet and fill section.

Just as inlet effects alter the pressure loss across the fill, fill pressure loss likewise has an impact on inlet effects. The velocity maps in Section 4.2.1 and 4.2.2 show that the velocity

profile in an empty tower forms a single peak in the center of the rain zone, whereas two separate peaks are formed in the same plane of a full tower due to the presence of fill. Lindahl and Bugler [17] describe observations of increased pressure ratio (R_p) improving the distribution of air across the bottom of the fill, where R_p is the ratio between total system pressure drop and the dynamic pressure at the inlet. With this experimental model, this effect of pressure ratio on below-fill velocity profile can be examined.

Velocity maps in the rain zone plane were constructed to observe the distribution of airflow in this region below the fill. Figure 4.30 shows these velocity maps for the highest airflow cases, along with the value of R_p for each. Note that the inlet velocity from which dynamic pressure is calculated is larger than the air velocity within the cooling tower by a factor of 1.33 due to the ratio of the inlet area (0.312 m^2) to the tower's cross-sectional area (0.416 m^2). Although the differences between the profiles in Figure 4.30 seem minor, a few key observations can be made. An increase in fill height corresponds with a separation of the two velocity peaks. The size and severity of the recirculation zones appears to decrease with increasing fill height. In addition, the highest peak velocities seem to flatten out when 120 cm of fill is used.

To quantify and compare the maldistribution of air in this plane, a sample standard deviation can be computed for each case, using

$$\sigma_v = \sqrt{\frac{1}{25 - 1} \sum_{i=1}^{25} |v_i - v_{\text{mean}}|^2}, \quad (4.11)$$

where σ_v is the standard deviation in velocity, v_i is the velocity recorded at point i , and v_{mean} is the overall mean vertical air velocity for that cross section. This standard deviation decreases with increasing fill height for fill-only experiments, indicating more uniform distribution: 30 cm of fill yields $\sigma_v = 2.30\text{ m/s}$, 60 cm yields $\sigma_v = 2.10\text{ m/s}$, 90 cm yields $\sigma_v = 1.94\text{ m/s}$, and 120 cm of fill yields $\sigma_v = 1.91\text{ m/s}$.

However, when major components are added or removed from the system, the pattern is less clear. Compare this to the empty tower velocity map at the same location, which has $\sigma_v = 2.23\text{ m/s}$. Further, the standard deviation for the rain zone plane in the full tower configuration shown in Figure 4.22 (which has an R_p of 16), has $\sigma_v = 2.16$.

Regardless, the velocity profile below the fill clearly changes with varying pressure ratio. To examine this phenomenon further, testing with different inlet configurations or higher resolution of the velocity field is recommended.

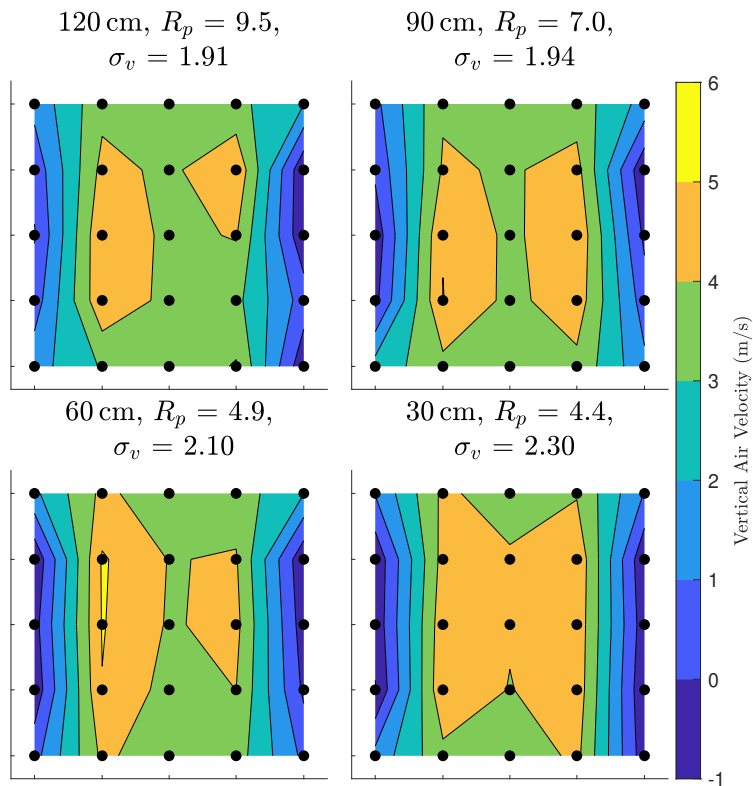


Figure 4.30 – Velocity maps in the rain zone plane for varying fill height. As a result, pressure ratio (R_p) is also varied. All four cases were tested with 60 Hz input to the fan, resulting in 2.4 - 2.7 m/s.

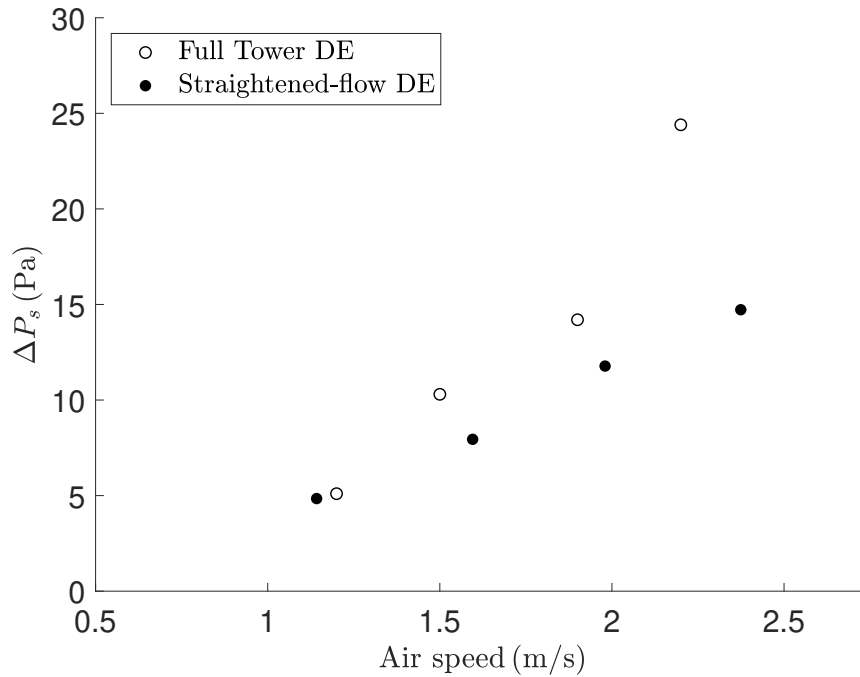


Figure 4.31 – Drift eliminator - static pressure drop

4.3.2 Drift Eliminator

The drift eliminator is another key component in cooling towers that creates a static pressure drop in the system. Similar to the fill, it is useful to characterize this pressure drop across a drift eliminator relative to air flow. Attempts to characterize the static pressure drop of the drift eliminator using dynamic losses (2.32) were unsuccessful; a consistent K factor could not be determined. Therefore, in this section, static pressure drop is simply examined with respect to air velocity.

For the first data set, the full tower test results (described in Section 4.2.2) were utilized. The calculated static pressure difference between the plenum and spray zone planes was used to estimate the pressure drop generated by the drift eliminator (and the spray nozzle, whose effect was found to be small in contrast). Figure 4.31 shows the measured pressure loss obtained for a full tower experiment as white points. These results compared poorly with the manufacturer’s predicted pressure loss for the same product. Brentwood’s correlation for the pressure drop of the CF150MAx drift eliminator is not shown within this work due to copyright, but can be accessed with authorization from Brentwood Industries through their Document Center [42].

In order to remove small liquid droplets, a drift eliminator must guide the airflow through multiple sharp turns. This results in an inevitable static pressure drop, and at this small scale, causes a significant disturbance in the air flow field. As described in Section 4.2.2,

zones of recirculating air appear on two adjacent sides of the cooling tower immediately above the drift eliminator due to the way in which its geometry forces airflow away from the wall in those regions. In a full-scale cooling tower, these recirculation zones would only appear along the walls or support structures where the drift eliminator guides air away from them - a potentially minor effect. In this lab-scale model, however, the size of the recirculation zones produced by the drift eliminator is very significant, as can be observed in the velocity maps of Figures 4.22 through 4.25, restricting the area available for upwards-flowing air significantly, and perhaps, inducing additional static pressure loss locally.

For application to full-scale cooling towers, it would be more useful to characterize the pressure drop of the drift eliminator disregarding these localized regions of stagnant air. Therefore, a second data set was collected for which the drift eliminator was laid between two fill sections which would, in this context, act as flow-straighteners. A 30 cm section was placed under the drift eliminator so as to isolate it from inlet effects, and a 60 cm section was placed above the drift eliminator to suppress the action of the recirculation zones formed by the drift eliminator itself. After static pressure drops were measured in this configuration, the static pressure drop contributed by 90 cm of fill in a similar configuration was subtracted to remove the fill and inlet pressure drops from the total, yielding an approximate pressure drop due to the drift eliminator alone.

The results from this “sandwich” configuration are shown by the black points in Figure 4.31 (Straightened-flow DE). A dramatic difference in the pressure drops can be observed between the cases with and without flow-straightening elements added. For a very large cooling tower, the pressure drop reported by the manufacturer (or the results from the “sandwich” configuration) can likely be used without concern. However, for smaller-scale cooling towers, these elevated static pressure losses above the drift eliminator may be a significant consideration in terms of design. It should be noted that, although the fill installed above and below the drift eliminator for the “sandwich” configuration acts as a flow-straightener to attempt to isolate the effect of the drift eliminator, the interaction of the flows through the fill and drift eliminator in sequence may be more complex than this treatment acknowledges, presupposing a linear superposition of pressure drops. Further research may be warranted with regards to characterizing the effect of drift eliminators on static pressure loss and the air flow field.

4.3.3 Static Pressure Loss of Multiple Components

The results of the preceding analysis show that static pressure drops observed for different tower elements cannot simply be added together to obtain the total static pressure drop for the cooling tower; the elements are too close together, and each has a distinct effect on the

flow field to which the other elements are subjected. This phenomenon has been explored in terms of duct fittings by numerous researchers, many of whom arrived at different conclusions regarding how the total static pressure drop is affected by such closely spaced elements. Some researchers observed that the total static pressure drop was always less than the sum of that predicted for each individual element [43, 44], while others found that pressure drop could be increased to more than the sum of that of the individual elements [45, 46]. Although these papers are comparing the effects of closely-coupled ductwork fittings such as elbows and branches, considering the same principle of interaction of airflow-disturbances causing a shift in overall static pressure loss, the interaction observed between the inlet and fill losses is hardly surprising.

When a 60 cm layer of fill was raised up in the tower beyond the recirculation zones formed above the air inlets, static pressure loss was found to increase across the fill. Therefore, in the case of fill-inlet interaction, lower pressure losses may be obtained for the same air flow rate when the fill is lower - closer to the inlet's top edge. Because the geometry of the experimental apparatus and the fill within it has a demonstrable effect on the measured results, it is perhaps more understandable that the results collected in this work do not match precisely those collected independently by the fill manufacturer due to differing inlet effects.

4.4 Wet Tower Tests

Although the dry tower experiments may be useful for full-tower airflow visualization, a cooling tower will rarely be run under dry conditions in practice. In terms of airflow, adding water to the system constricts the airflow channels in the fill and introduces droplets in the spray and rain zones. The overall effect is an increased static pressure drop across all wetted zones of the tower.

Although the pitot tube can be used in an area with water droplets present without damage, the sampling holes of the pitot tube become clogged with water almost immediately, leading to erroneous results. Therefore, pitot traverse measurements were collected only above the drift eliminator in order to visualize the air velocity profile and static pressure drop in the plenum chamber.

The water flow rate was measured with a turbine flowmeter and controlled using globe valves. A full-cone nozzle (BETE NC 2065) was used, its height adjusted so as to produce minimal wall water, although the corners of the cell were dry as a result. As was done previously for the dry tower experiments, a 25-point traverse above the drift eliminator was used to resolve the air velocity and static pressure fields at the plenum plane. Total pressure drop was measured with the Fluke 922 above the drift eliminator due to the larger pressure

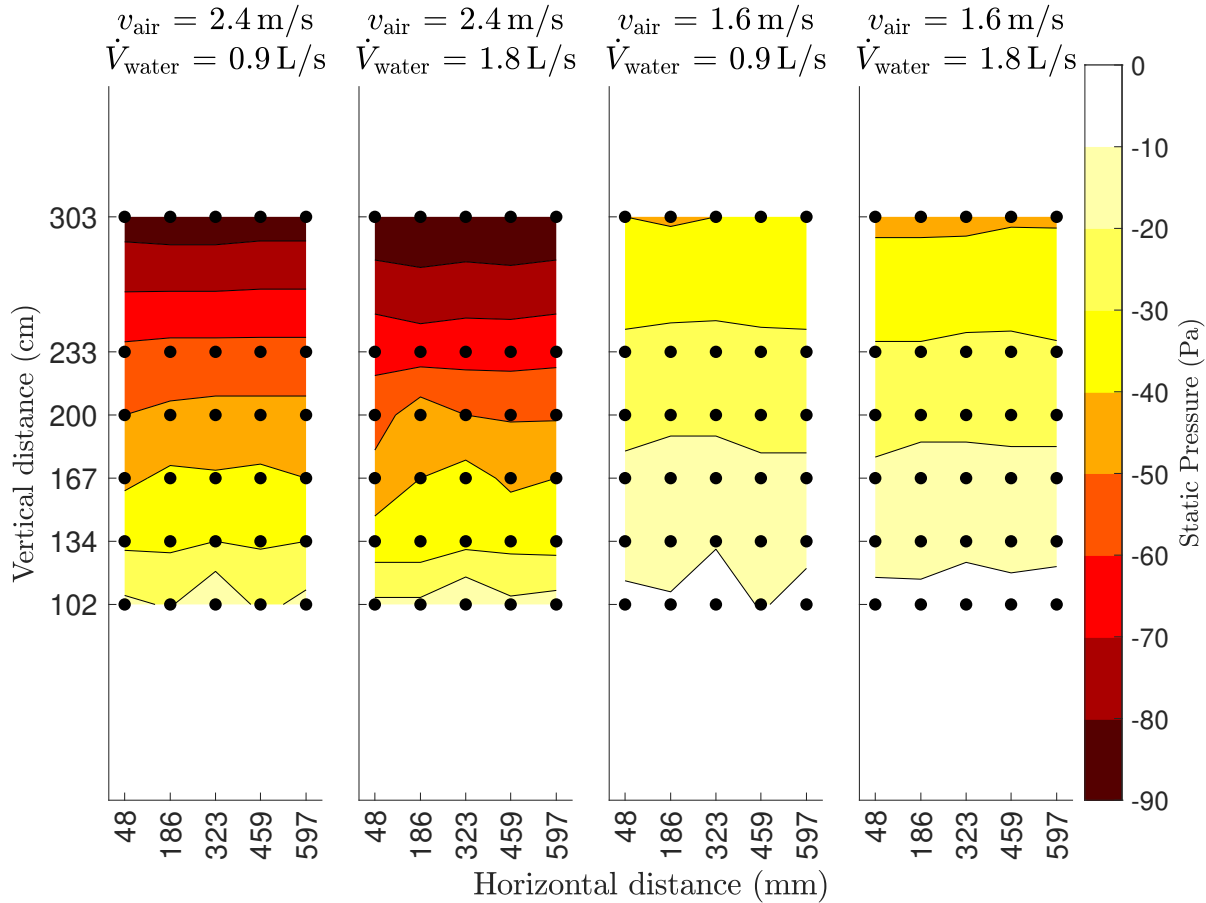


Figure 4.32 – Wet tower static pressure taps for two air speeds and two water flow rates

drops anticipated - therefore, all static pressures observed in this experiment reflect not only water addition, but also the combined effects of all cooling tower features, including inlet, rain zone, fill, spray zone, and drift eliminator losses.

Because of the significant recirculation zones above the drift eliminator, the air velocity traverse results could not be trusted to yield the overall air flow rate upon averaging [36]. Therefore, overall air flow rate was measured using the STRA averaging pitot tube and the relationship (4.7) established in Section 4.1.6.

Static pressure was measured by inserting a tube connected to the Fluke 922 pressure sensor into probe holes, perpendicular to the bulk air flow, acting as a static pressure tap at each tested location. The Fluke 922 measured the total pressure difference between the sampled location and the ambient, yielding a measurement of static pressure loss.

The static pressures recorded for the wet tower using the static tap procedure are summarized in Figure 4.32 with the sampled locations shown as black points. Except for the region below the fill, static pressure is observed to be generally uniform across each cross

Table 4.4 – Static pressure drop summary for wet fill with two air speeds and two water flow rates

Fan Input (Hz)	v_{av} (m/s)	\dot{V}_w (L/s)	$\Delta P_{s,\text{measured}}$ (Pa)
60	2.4	0.91	40
40	1.6	0.89	20
60	2.4	1.81	48
40	1.6	1.81	22

section. Using these results, the contribution of the fill to static pressure loss can be observed separately from that of the drift eliminator, nozzle, and the spray itself. Subtracting the average static pressure at the rain zone plane (102 cm elevation) from that at the spray zone plane (233 cm elevation), the static pressure drop across the fill was determined. These static pressure drops across the fill are summarized in Table 4.4. The disagreement between these measurements and the manufacturer’s prediction is similar to that observed for the dry fill in Section 4.3.1, again suggesting a systematic difference in the methods used by the manufacturer compared to those methods outlined in this work.

A full 25-point traverse of velocity and static pressure was also performed above the drift eliminator where no water droplets could flood or otherwise obstruct the pitot tube sampling ports. From these results, a set of pressure and static pressure maps were generated, shown in Figure 4.33. The traverse results show a relatively uniform static pressure across the plenum plane, agreeing with the static pressure tap results. As previously observed in the dry tower, regions of stagnant, recirculating air can be observed along two adjacent walls above the drift eliminator due to the direction of airflow away from the walls by the drift eliminator in those locations. The “shadow” of the spray nozzle and its feed pipe are less visible in the velocity maps of Figure 4.33 compared to the dry tower configuration of Figures 4.17, 4.18 and 4.20. This lack of a distinct local velocity minimum in the center of the tower’s cross section can be explained; in the dry tower, the nozzle interacted with air flow as a protruding, sharp-edged object, whereas in the wet tower, the spray emerging from the nozzle creates a wider and more diffuse obstruction to airflow. Doubling the water loading had little effect on the air velocity and static pressure above the drift eliminator. For this fill 1 L/s is considered a low water loading, while 2 L/s is considered a moderate loading.

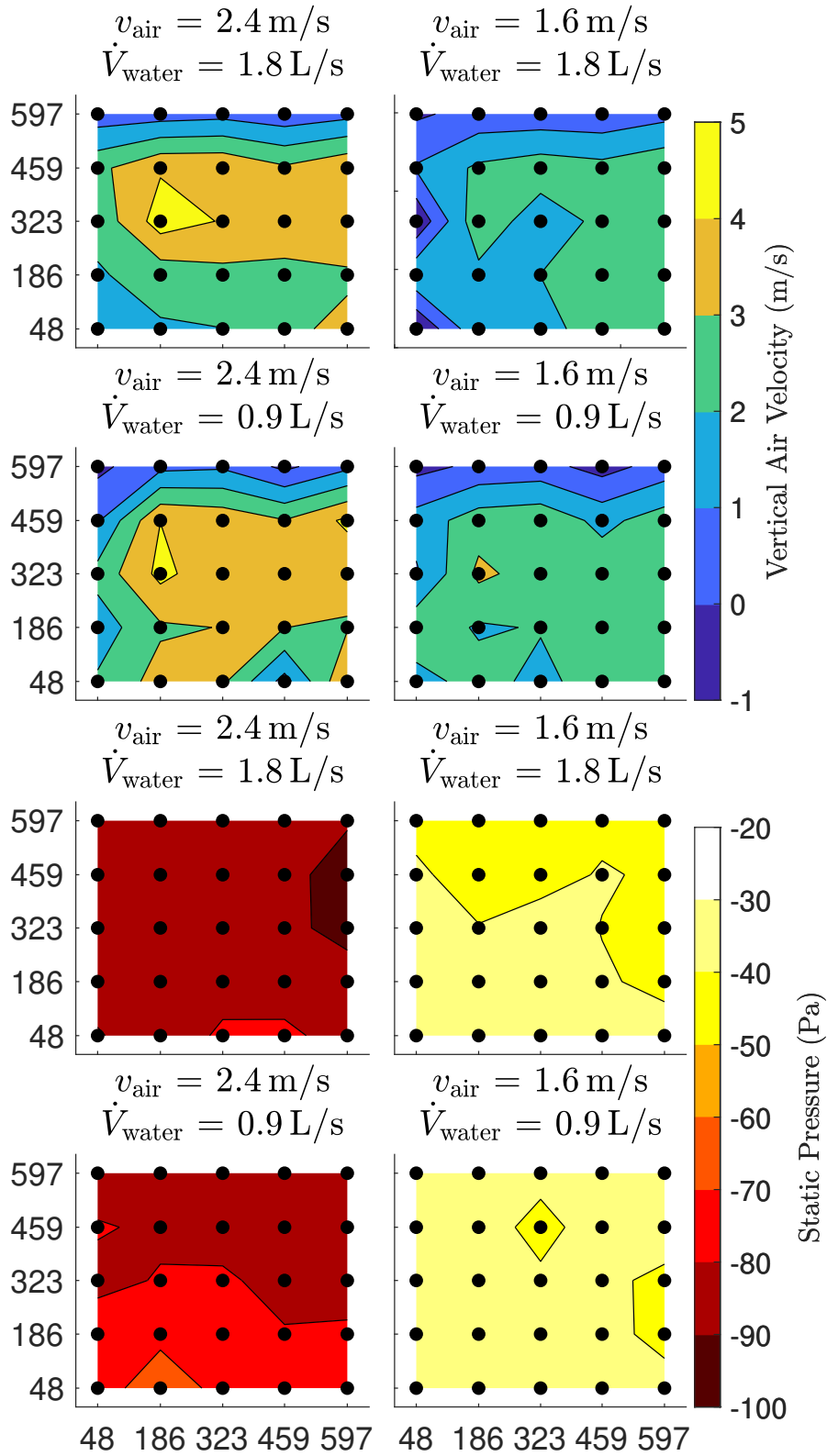


Figure 4.33 – Vertical velocity and static pressure maps at plenum plane

Chapter 5

Conclusions

A lab-scale experimental wet cooling tower model was designed and built to measure airflow and thermal performance. Unique from other experimental models in literature, this model allows for the measurement of air velocity and static pressure within the tower at multiple locations under dry conditions, allowing for a more detailed investigation of air flow patterns inside. A detailed validation and error analysis of air velocity measurements was performed.

This work first focused on the investigation of air flow in a dry cooling tower. Using the experimental model, complete maps of vertical air velocity and static pressure were generated under dry conditions from point measurements taken from inside the cooling tower. Static pressure drop across the drift eliminator and across fill of various heights were measured and compared with manufacturer data. As the tested fill section was moved above the air disturbances created by inlet effects, the static pressure drop across the fill increased. Significant differences between the results observed in this work and manufacturer's estimates are attributed to differences in the geometries of the experimental models used, particularly in the inlet region. Each element contributed to airflow disturbance and static pressure loss, and the interaction of these effects from elements installed closely in sequence was found to be nonlinear.

Static pressure drop was also investigated for a cooling tower under wet conditions. Static pressure was measured using taps located along the cooling tower wall, allowing for the visualization of static pressure losses throughout the tower. As with the dry tower, the measured wet tower static pressure drops varied from those predicted by the fill manufacturer. Air velocity and static pressure maps in the plenum chamber were also generated from traverse measurements taken above the drift eliminator. These maps illustrate the effect of water loading on the air distribution in the plenum chamber.

These results demonstrate the complexity of airflow phenomena within cooling towers which are neglected when utilizing 0D/1D analysis methods. The testing facility described in this thesis and the associated data can now be applied in the study of airflow within induced

draft counterflow cooling towers in various configurations, and applied in the development of analysis tools to characterize those phenomena. Suggestions for future work follow this theme.

Tests under wet conditions were only performed for four different air and water loading combinations. Significant differences were noted between pressure drops measured using this facility compared to those given by the fill manufacturer - hot water tests should likewise be performed to note any corresponding discrepancies in thermal performance and investigate their causes. An investigation regarding suitable nozzles and water distribution in this testing facility is recommended as a precursor to such a study.

The dramatic effect of inlet conditions has been noted throughout this work, although only one inlet configuration was investigated: two inlets on opposing sides. Because cooling towers may have inlets on as few as one or as many as four sides, it is reasonable to investigate the effect that each inlet configuration has on air distribution within the tower, and perhaps, on thermal performance.

Particular airflow-altering geometries could also be investigated using this testing facility. The effect of beneficial features such as air dams and deleterious features such as support beams can be visualised with velocity and pressure maps, and their contributions quantified for different arrangements.

Finally, and coming full-circle, the velocity and pressure map data collected in this work should be utilized in the validation of CFD models applied to cooling tower simulation so as to confirm or improve the reliability of such tools for cooling tower analysis and design.

References

- [1] Donald Baker. *Cooling Tower Performance*. Chemical Publishing Co., 1984.
- [2] F. Merkel. Verdunstungskühlung. *V. D. I. Forschungsarbeiten*, (275), 1925.
- [3] Kam W. Li and A. Paul Priddy. *Power Plant System Design*. John Wiley & Sons, 1985.
- [4] *HVAC Systems and Equipment*. ASHRAE, 2008.
- [5] J. Jackson. *Cooling Towers*. Butterworths Scientific Publications, 1951.
- [6] Nicholas P. Cheremisinoff and Paul N. Cheremisinoff. *Cooling Towers: Selection, Design and Practice*. Ann Arbor Science, 1981.
- [7] S. A. Cale. Development of evaporative cooling packing. Technical Report EUR 7709 EN, Commission of the European Communities, 1982.
- [8] A. K. M. Mohiuddin and K. Kant. Knowledge base for the systematic design of wet cooling towers. Part I: Selection and tower characteristics. *Int J. Refrig.*, 19(1):43–51, January 1996.
- [9] W. Stanford and G. B. Hill. *Cooling Towers: Principles and Practice*. Carter Thermal Engineering Ltd., 1967.
- [10] SPX Cooling Technologies Inc. *Cooling Tower Fundamentals*. SPX Cooling Technologies Inc., 2nd edition, 2009.
- [11] M. L. Moon. Environmental impact of salt drift from a natural draft cooling tower. *Johns Hopkins APL Technical Digest*, 1(2):120–128, April-June 1980.
- [12] *Legionellosis Guideline: Best Practices for Control of Legionella*. Cooling Technology Institute, July 2008.
- [13] S. C. Kranc. The effect of nonuniform water distribution on cooling tower performance. *Journal of Energy*, 7(6):636–639, November-December 1983.

- [14] J. E. Thacker. Design of medium pressure nozzles for cooling towers. Master's thesis, University of Stellenbosch, May 1997.
- [15] D. G. Kröger. *Air Cooled Heat Exchangers and Cooling Towers, Volume 1*. Penwell Corp, 2004.
- [16] A. Klimanek, R. A. Bialecki, and Z. Ostrowski. CFD two-scale model of a wet natural draft cooling tower. *Numerical Heat Transfer, Part A*, (57):119–137, 2010.
- [17] P. Lindahl Jr. and T. Bugler III. Counterflow cooling tower design with high energy evaluations. Technical Report TP87-04, Cooling Technology Institute, 1987.
- [18] H. C. R. Reuter and D. G. Kröger. Computational fluid dynamics analysis of cooling tower inlets. *Journal of Fluids Engineering, Transactions of the ASME*, 133(8):081104, 2011.
- [19] N. Milosavljevic and P. Heikkilä. A comprehensive approach to cooling tower design. *Applied Thermal Engineering*, 21:899–915, June 2001.
- [20] A. Klimanek, T. Musioł, and A. Stechman. Optimization of guide vane positions in bended inflow of mechanical draft wet-cooling tower. *Archives of thermodynamics*, 32(3):263–272, 2011.
- [21] A. Klimanek. Numerical modelling of natural draft wet-cooling towers. *Arch Comput Methods Eng*, (20):61–109, 2013.
- [22] A. K. Majumdar, A. K. Singhal, and D. B. Spalding. Numerical modeling of wet cooling towers - Part 2: Application to natural and mechanical draft towers. volume 105 of *Transactions of the ASME*, pages 736–743, 1983.
- [23] D. J. Benton and W. R. Waldrop. Computer simulation of transport phenomena in evaporative cooling towers. volume 110 of *Transactions of the ASME*, pages 190–196, 1988.
- [24] M. N. A. Hawlader and B. M. Liu. Numerical study of the thermal-hydraulic performance of evaporative natural draft cooling towers. *Applied Thermal Engineering*, (22): 41–59, 2002.
- [25] N. Williamson, S. Armfield, and M. Behina. Numerical simulation of flow in a natural draft wet cooling tower - the effect of radial thermofluid fields. *Applied Thermal Engineering*, (28):178–189, 2008.

- [26] R. Al-Waked and M. Behnia. CFD simulation of wet cooling towers. *Applied Thermal Engineering*, (26):382–395, 2006.
- [27] P. C. Oosthuizen. Performance characteristics of hybrid cooling towers. Master’s thesis, University of Stellenbosch, September 1995.
- [28] H. J. Lowe and D. G. Christie. Heat transfer and pressure drop data on cooling tower packings, and model studies of the resistance of natural-draught towers to airflow. Proceedings of the International Heat Transfer Conference, pages 933–950, 1961.
- [29] R. D. Fulkerson. Comparative evaluation of counterflow cooling tower fills. Technical Report TP-88-05, Cooling Technology Institute, 1988.
- [30] D. M. Bell, B. M. Johnson, E. V. Werry, P. B. Miller, D. E. Wheeler, K. R. Wilber, D. J. Benton, and J. A. Bartz. *Cooling Tower Performance Prediction and Improvement Volume 1: Applications Guide*. Electric Power Research Institute, 1990.
- [31] J. C. Kloppers and D. G. Kröger. A critical investigation into the heat and mass transfer analysis of counterflow wet-cooling towers. *International Journal of Heat and Mass Transfer*, 48:765–777, January 2005.
- [32] D. M. Bell, B. M. Johnson, E. V. Werry, P. B. Miller, D. E. Wheeler, K. R. Wilber, D. J. Benton, and J. A. Bartz. *Cooling Tower Performance Prediction and Improvement Volume 2: Knowledge Base*. Electric Power Research Institute, 1990.
- [33] ASHRAE. *Heating, Ventilating, and Air-Conditioning Systems and Equipment*. ASHRAE, 2016.
- [34] J. C. Kloppers and D. G. Kröger. The Lewis factor and its influence on the performance prediction of wet-cooling towers. *International Journal of Thermal Sciences*, (123):879–884, 2005.
- [35] Cooling Tower Institute. *Cooling Tower Performance Curves*. Millican Press, 1967.
- [36] *ASHRAE Handbook - Fundamentals*. ASHRAE, 2017.
- [37] W. Asvapoositkul and M. Kuansathan. Comparative evaluation of hybrid (dry/wet) cooling tower performance. *Applied Thermal Engineering*, 71:83–93, June 2014.
- [38] F. Gharagheizi, R. Hayati, and S. Fatemi. Experimental study on the performance of mechanical cooling tower with two types of film packing. *Energy Conversion and Management*, 48:277–280, June 2007.

- [39] M. Lucas, P. J. Martinez, and A. Viedma. Experimental study on the thermal performance of a mechanical cooling tower with different drift eliminators. *Energy Conversion and Management*, 50:490–497, January 2009.
- [40] First Sensor. LMI series – digital low differential pressure sensors. https://www.first-sensor.com/cms/upload/datasheets/DS_Standard-LMI_E_11823.pdf.
- [41] Béla G. Lipták. *Instrument Engineer’s Handbook - Process Measurement and Analysis*. CRC Press, 4th edition, 2003.
- [42] Brentwood Industries Inc. myBrentwood document center. <http://my.brentwoodindustries.com/mybrentwood/login.php>, 2019.
- [43] J. Rahmeyer. Pressure loss coefficients for close-coupled pipe ells. *ASHRAE Transactions*, 108(1):390–406, 2002.
- [44] S. Sami and J. Cui. Numerical study of pressure losses in close-coupled fittings. *HVAC&R Research*, 10(4):539–552, 2004.
- [45] N. K. Mylaram and S. Idem. Pressure loss coefficient measurements of two close-coupled HVAC elbows. *HVAC&R Research*, 11(1):133–146, 2004.
- [46] S. A. Mumma, T. A. Mahank, and Y. P. Ke. Analytical determination of duct fitting loss-coefficients. *Applied Energy*, 1997:229–247, 1997.
- [47] ASTM D1785-15. Standard specification for poly(vinyl chloride) (pvc) plastic pipe, schedules 40, 80, and 120. Standard, ASTM International, March 2018.
- [48] Y. Çengel and M. Boles. *Thermodynamics: An Engineering Approach*. McGraw Hill, 6th edition, 2008.
- [49] Frank M. White. *Fluid Mechanics*. McGraw-Hill, 6th edition, 2008.
- [50] Larry Bachus and Angel Custodio. *Know and Understand Centrifugal Pumps*. Elsevier, 2003.
- [51] *FAC Series End Suction Centrifugal Pump - Owner’s Manual*. Franklin Electric.
- [52] Dan Holohan. *The Lost Art of Steam Heating*. Dan Holohan Associates, Incorporated, special edition, 1992.
- [53] Incropera, DeWitt, Bergman, and Lavine. *Fundamentals of Heat and Mass Transfer*. Wiley, 2007.

- [54] Spence Engineering Company Inc. Series 2000 temperature regulator. Specification Sheet.
- [55] Xylem Inc. Hoffman Specialty general catalog. Specification Sheet, 2013.
- [56] Jon Monsen. Size matters: Control valve sizing 101. <http://www.valvemagazine.com/web-only/categories/education-training/4571-size-matters-control-valve-sizing-101.html>.
- [57] *ASHRAE Handbook - Fundamentals*. ASHRAE, 1997.
- [58] Chad Edmondson and Norman Hall. Steam basics part 15: Condensate return pump and receiver sizing. <http://jmpcoblog.com/hvac-blog/steam-basics-part-15-condensate-return-pump-and-receiver-sizing>, April 2017.
- [59] Bell & Gossett. Hoffman Specialty Watchman series WCS condensate units. Specification Sheet, 2012.
- [60] Fluke Corporation. Fluke 922 airflow meter users manual. http://assets.fluke.com/manuals/922_____umeng0100.pdf, November 2006.
- [61] J. R. Taylor. *An Introduction to Error Analysis - The study of Uncertainties in Physical Measurements*. University Science Books, 2nd edition, 1997.
- [62] Sensirion. Datasheet SHT3x-DIS humidity and temperature sensor. https://www.sensirion.com/fileadmin/user_upload/customers/sensirion/Dokumente/0_Datasheets/Humidity/Sensirion_Humidity_Sensors_SHT3x_Datasheet_digital.pdf, February 2019.
- [63] Bosch. BME680 - low power gas, pressure, temperature, and humidity sensor. https://ae-bst.resource.bosch.com/media/_tech/media/datasheets/BST-BME680-DS001.pdf, July 2019.

Appendices

Appendix A

Merkel Design Example

Below is described an example case of cooling tower design, in which a fill is selected to achieve a certain cooling performance. This example demonstrates how the Merkel theory outlined in Chapter 2 is utilized in practice. From such a design as a baseline, the pressure drop contributed by the water load and fill height selected can be analysed, and a fan sized to provide the required airflow.

Assume a water loading of $15,000 \text{ kg}/(\text{m}^2\text{h})$ is desired, with an L/G ratio of 1.5. The design air inlet wet bulb temperature is 25°C with an enthalpy of $50 \text{ kJ}/\text{kg}$ of dry air, and the desired range and approach are 20°C and 5°C , respectively. These give an inlet water temperature of 50°C , and an outlet water temperature of 30°C . With this information, the height of fill that would provide the requisite cooling can be estimated. For this example, consider an orthogonal grid of $25 \times 6 \text{ mm}$ timbers with 25 mm pitch (such as Cale's [7] Figure 6.42).

To determine the Merkel number demanded, (2.24) must be solved numerically. Since Cale's fill equation was determined using Chebyshev quadrature, the same method must be used in calculating the demand Merkel number to minimize error. To implement this method, the integral is expressed as follows:

$$\begin{aligned} \text{Me} &= \int_{T_{wo}}^{T_{wi}} \frac{c_{pw}}{(i_s - i_{av})} dT_w \\ &\approx \frac{c_{pw}(T_{wi} - T_{wo})}{4} \times \left[\frac{1}{i_{s1} - i_{av1}} + \frac{1}{i_{s2} - i_{av2}} + \frac{1}{i_{s3} - i_{av3}} + \frac{1}{i_{s4} - i_{av4}} \right], \end{aligned} \quad (\text{A.1})$$

where 1, 2, 3, and 4 are different points within the fill, corresponding to

$$T_{w1} = T_{wo} + (T_{wi} - T_{wo}) \times 0.1 = 50 + (50 - 30) \times 0.1 = 32^\circ\text{C},$$

$$T_{w2} = T_{wo} + (T_{wi} - T_{wo}) \times 0.4 = 50 + (50 - 30) \times 0.4 = 38^\circ\text{C},$$

$$T_{w3} = T_{wo} + (T_{wi} - T_{wo}) \times 0.6 = 50 + (50 - 30) \times 0.6 = 42^\circ\text{C}, \text{ and}$$

$$T_{w4} = T_{wo} + (T_{wi} - T_{wo}) \times 0.9 = 50 + (50 - 30) \times 0.9 = 48^\circ\text{C}.$$

In (A.1), the enthalpies of the saturated air film at each of the four points listed above and of the bulk air adjacent are required. The enthalpy of the saturated air film can be found either by employing an empirical relation or by use of tables. For simplicity, the saturated air enthalpies corresponding to these water temperatures will be looked up from tables. From ASHRAE Fundamentals [36] this gives $i_{s1} = 110.979$, $i_{s2} = 150.713$, $i_{s3} = 184.275$, and $i_{s4} = 248.955$ in kJ/kg of dry air.

The enthalpy of the bulk air can be determined by recalling that all energy lost by the bulk water must be absorbed by the bulk air, in the form of increased temperature and humidity. Knowing that the inlet air has an enthalpy of 50 kJ/kg, the enthalpies of the bulk air at points 1 through 4 can likewise be found:

$$\begin{aligned} i_{av1} &= i_{avi} + 0.1 \times c_{pw}(T_{wi} - T_{wo}) \times L/G = 50 + 0.1 \times (4.18)(20) \times (1.5) = 62.54 \text{ kJ/kg}, \\ i_{av2} &= i_{avi} + 0.4 \times c_{pw}(T_{wi} - T_{wo}) \times L/G = 50 + 0.4 \times (4.18)(20) \times (1.5) = 100.16 \text{ kJ/kg}, \\ i_{av3} &= i_{avi} + 0.6 \times c_{pw}(T_{wi} - T_{wo}) \times L/G = 50 + 0.6 \times (4.18)(20) \times (1.5) = 125.24 \text{ kJ/kg}, \text{ and} \\ i_{av4} &= i_{avi} + 0.9 \times c_{pw}(T_{wi} - T_{wo}) \times L/G = 50 + 0.9 \times (4.18)(20) \times (1.5) = 162.86 \text{ kJ/kg}, \end{aligned}$$

assuming c_{pw} of 4.18 kJ/(kg K) for liquid water, the specific heat of liquid water being relatively insensitive to temperature.

Now it is possible to evaluate the integral in (A.1), yielding

$$\begin{aligned} \text{Me} &= \frac{4.18(20)}{4} \times \left[\frac{1}{110.979 - 62.54} + \frac{1}{150.713 - 100.16} + \frac{1}{184.275 - 125.24} + \frac{1}{248.955 - 162.86} \right] \\ &= 1.44. \end{aligned}$$

This is the demand Merkel number expressing the cooling requirement of the system. This demand Merkel number can be used together with Cale's equation for the supplied Merkel number to determine how much fill would be needed in this case. Cale [7] gives the following equation for the fill in question, expressed per meter of height:

$$\frac{Ka}{L} = 1.17(L/G)^{-0.89}. \quad (\text{A.2})$$

Here, Ka/L can be regarded as the Merkel number divided by the fill height, Me/H_{fi} . Now H_{fi} can be solved, i.e.,

$$H_{fi} = \frac{Ka/L}{1.17(L/G)^{-0.89}} = \frac{1.44}{1.17(1.5)^{-0.89}} = 1.77 \text{ m}.$$

If the demand curve is calculated in the same way for a variety of other L/G ratios, and likewise, if the Merkel number supplied from 1.77 m of the same fill is calculated for these

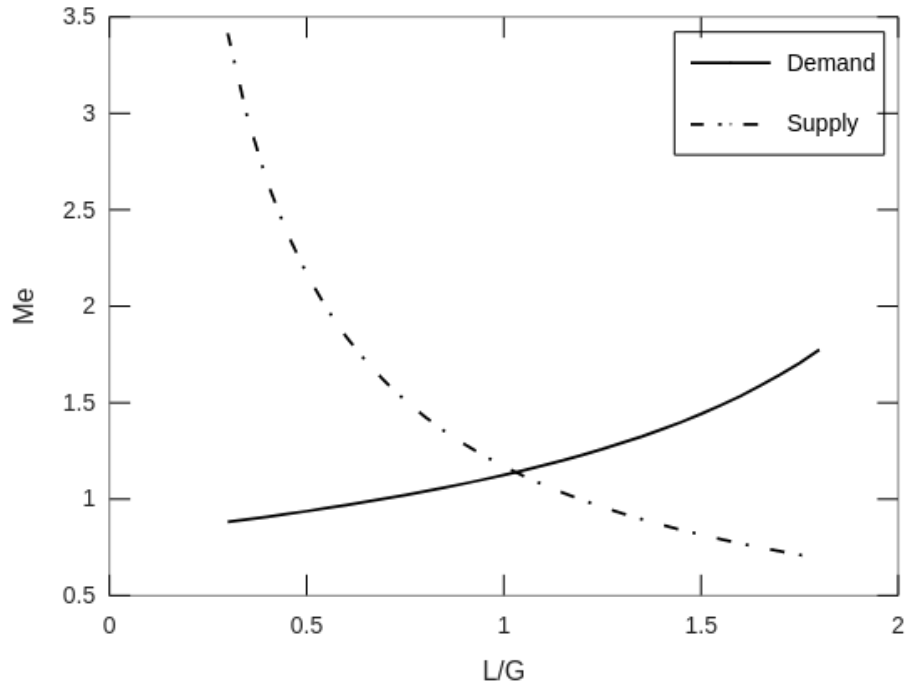


Figure A.1 – Supply and demand Merkel number curves for Section A example

same L/G ratios, they can plot them together as shown in Figure A.1. The point where the two curves intersect shows the design point.

Appendix B

Water System Design

B.1 Design Objectives

The water system was designed to achieve a flow range of 1 to 3 L/s, for a wide range of cooling tower water loadings. This water was to be delivered at a controlled temperature between room temperature and 50°C.

B.2 Pump and Valve Selection

A pump and two globe valves were selected as part of an iterative process so as to obtain the required flow rates, confirm that the selected valves provided adequate control of the flow rate, and that the pressure losses generated in the system were met by the pump. The hot water pump can be made to pump water either to the cooling tower or back to the heat exchanger so as to keep the tank water warm. The cold water pump can be made to pump a) directly to the cooling tower, b) through the heat exchanger to the hot water tank, or c) through the heat exchanger to the cooling tower.

The design example described below is for the hot water feed pump, considering the case where it feeds into the tower during an experiment - see Figure B.1. The hot water tank is open to atmosphere. The water level could be anywhere between 10 and 100 cm above the exiting pipe - this will be taken as 100 cm, the most typical case, in the design calculations to follow. The majority of the pipe is 2" PVC, with other details as indicated in Figure B.1. Because of the wide range of water flow rates required of the experiment, a parallel recirculation line has been included in the system. Therefore, analysing the system shown in Figure B.1 is not as straightforward as constructing a single system curve and comparing it against a pump curve. The feed line and recirculation line each have a globe valve to control their respective flow rates, and the open- or closedness of the valves affects the backpressure, P_T , experienced by both. Therefore a system of equations must be solved to compute the

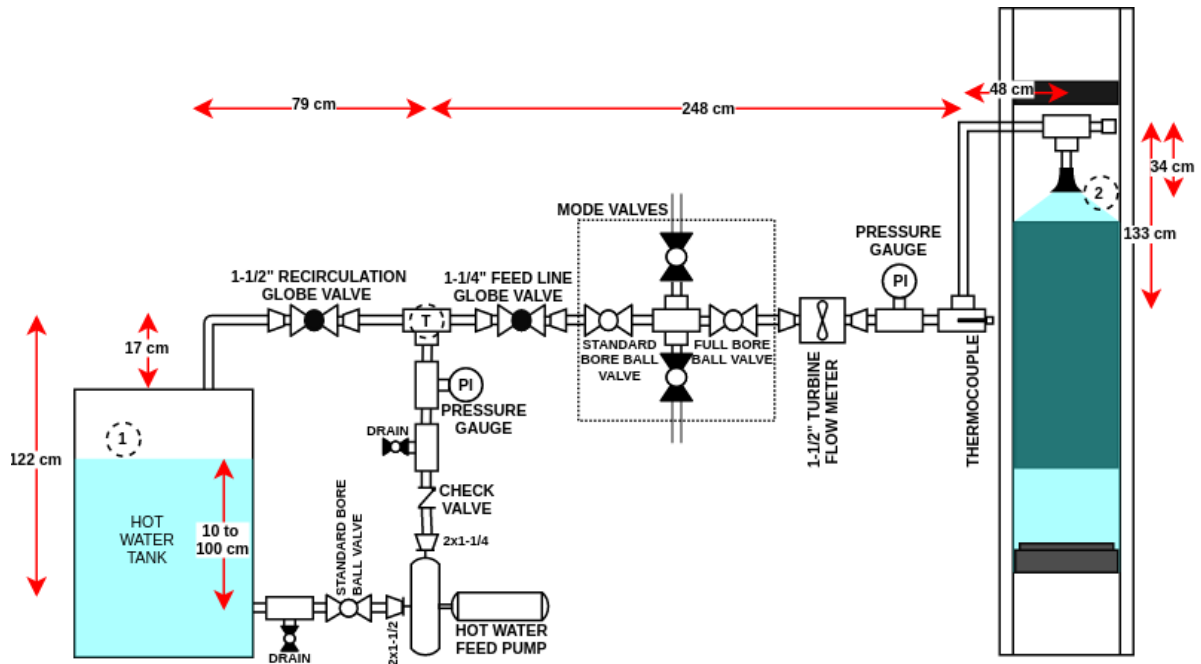


Figure B.1 – Schematic showing the equipment required to supply of hot water to the tower. This diagram forms the basis for constructing the Bernoulli equations for the system, making particular reference to the points labeled as “T”, “1” and “2” above.

unknown variables:

Q_0 = total flow rate in L/s,

Q_f = feed line flow rate in L/s,

Q_r = recirculation flow rate in L/s,

P_T = pressure at the tee in Pa, and

h_p = pump head in m.

To solve these five unknowns, the five equations (B.1), (B.3), (B.4), (B.7), and (B.9) are used. First, conservation of mass is considered. Noting that density changes in water due to temperature variation will be negligible, the sum of the feed line and recirculation line flow rates must be equal to the total flow rate through the pump, that is,

$$Q_0 = Q_f + Q_r. \quad (\text{B.1})$$

where Q_0 is the flow rate through the pump, Q_f is the flow rate in the feed line sent to the cooling tower, and Q_r is the flow rate through the recirculation line.

Knowing that the maximum desired flow rate is 3 L/s and that the NPS 2 pipe has an

inner diameter of 52.5 mm [47], the Reynolds number is

$$\text{Re} = \frac{4\rho Q}{\mu\pi D} = \frac{(4)(1000 \text{ kg/m}^3)(0.001 \text{ to } 0.003 \text{ m}^3/\text{s})}{(0.000546 \text{ Ns/m}^2)(0.0525 \text{ m})\pi} = 140000 \text{ to } 420000, \quad (\text{B.2})$$

where ρ is density, Q is flow rate in m^3/s , μ is the dynamic viscosity of water at 50°C (0.000546 Ns/m^2 interpolated from Çengel and Boles [48]), and D is the pipe inner diameter. On a Moody chart, these Reynolds numbers correspond to a regime of turbulence (but not complete turbulence), considering a characteristic roughness of 0.0015 mm for PVC pipe. However, for convenience, rough turbulent flow will be assumed for purposes of estimating the pressure losses in the pipe, acknowledging that major losses will be underestimated slightly. This simplification has only a slight effect on the calculated results because minor losses dominate in this system. The feed and recirculation flow rates can be found using

$$Q_f^2 R_f = \frac{P_T - P_{atm}}{\rho g} + (z_T - z_{nozzle}) - \Delta h_{nozzle}, \quad (\text{B.3})$$

and

$$Q_r^2 R_r = \frac{P_T - P_{atm}}{\rho g} + (z_T - z_{return}), \quad (\text{B.4})$$

where P_{atm} is the atmospheric pressure in the laboratory, usually 92000 Pa, ρ is the density of water, taken as 1000 kg/m^3 , g is the acceleration of gravity, taken as 9.81 m/s^2 , $(z_T - z_{nozzle})$ is the physical height difference between the spray nozzle in the cooling tower and the tee, which is taken as 0.99 m, h_{nozzle} is the exit loss at the nozzle expressed as head loss, measured in m (this depends on the nozzle design, the flow rate, and the size of any nozzle inserts added), $(z_T - z_{return})$ is the physical height difference between the outlet of the recirculation line's return to the tank and the tee, which is 17 cm, and R_f and R_r are the resistances of the feed and recirculation lines ($\text{m}\cdot\text{s}^2/\text{L}^2$). These are calculated using

$$R = \frac{8}{\pi^2 g} \times \left(\frac{fL}{D_p^5} + \sum_i \left(\frac{K_i}{D_i^4} \right) + \frac{K_v}{D_v^4} \right), \quad (\text{B.5})$$

where f is the friction factor of the pipe of length L , K_i and K_v are the loss coefficients for the system components and the globe valve, respectively, and D_p , D_i , and D_v are the diameters of the pipe, the various components, and the globe valve, respectively.

The K values of the many components included in the system must be summed together as shown in (B.5). K_v alone is added separately because this value will change as the user adjusts the setting of the globe valve. Haaland's equation is used to find f , i.e.,

$$f = \left(-1.8 \log_{10} \left(\frac{6.9}{\text{Re}} + \left(\frac{\epsilon/D}{3.7} \right)^{1.11} \right) \right)^{-2}, \quad (\text{B.6})$$

Table B.1 – Estimated loss coefficients used for pump sizing

R_f			R_r			R_0		
Item	K	Size	Item	K	Size	Item	K	Size
Reducer ¹	1.15	1-1/4 x 2	Reducer ¹	0.41	2 x 1-1/2	Entrance losses ¹	0.42	2
Globe valve ²	8.1+	1-1/4	Globe Valve ²	7.6+	1-1/2	Tee (straight) ⁴	0.90	2
Reducer ¹	1.55	2 x 1-1/4	Reducer ¹	0.46	1-1/2 x 2	Ball valve (STD bore) ³	1.4	2
Ball valve (STD bore) ³	1.4	2	Elbow ⁴	0.95	2	Reducer ¹	0.41	2 x 1-1/2
Cross ^{4,5}	0.90	2				Reducer ¹	1.15	1-1/4 x 2
Ball valve (full bore) ²	0.03	2				Check valve (swing) ⁴	2.1	2
Reducer ¹	0.41	2 x 1-1/2				Tee (straight) ⁴	0.9	2
Flowmeter ⁶	6	1-1/2				Tee (straight) ⁴	0.9	2
Reducer ¹	0.46	2 x 1-1/2				Tee (branch) ⁴	1.8	2
Elbow ⁴	0.95	2						
Tee (straight) ⁴	0.90	2						
Tee (branch) ⁴	1.8	2						
Elbow ⁴	0.95	2						
Tee (branch) ⁴	1.8	2						

For convenience, K -values for all parts except valves have been scaled to the inner diameter of NPS2 pipe.

¹ Assumed to be a sudden expansion or contraction using equations from White [49].

² Converted from open-valve C_v provided by manufacturer.

³ Assumed from manufacturer data for similar valves.

⁴ Using table from White [49] for threaded steel fittings; PVC fittings should have slightly lower resistance coefficients in general, due to smoothness.

⁵ Treated as line (straight) flow through a 2" screwed tee from White [49].

⁶ Assumed so as to provide a pressure drop similar to other turbine flowmeters.

	Low flow	High flow	Maximum flow
$K_{v,f}$	115	12	8.1
$K_{v,r}$	35	500	∞
Q_f (L/s)	1.0	3.0	3.7
Q_r (L/s)	3.0	0.86	0

Table B.2 – Summary of flow rates for globe valve closure represented by K_v

where ϵ is the roughness of the pipe, assumed to be 0.0015 mm for PVC pipe.

The total flow rate, Q_0 , in the pump suction and discharge lines (prior to the tee) is treated in a similar fashion:

$$Q_0^2 R_0 = \frac{P_{atm} - P_T}{\rho g} + (z_{tank} - z_T) + \Delta h_{pump}, \quad (\text{B.7})$$

where z_{tank} is the height of water in the tank above the suction line, Δh_{pump} is the head added by the pump, and R_0 is given by

$$R_0 = \frac{8}{\pi^2 g} \times \left(\frac{fL}{D_p^5} + \sum_i \left(\frac{K_i}{D_i^4} \right) + \frac{1}{D_v^4} \right). \quad (\text{B.8})$$

The term on the far right accounts for the dynamic head at the tee. To solve (B.5) for the feed and recirculation lines and (B.8) for the pump discharge, estimates for the K values of each loss-creating component are required. These estimates are summarized in Table B.1 below.

Finally, Δh_{pump} must be solved by performing a curve fit to manufacturer-provided pump performance data. In the case of the selected pump, FAC-100S (1 hp), the resulting equation is

$$h_{pump} = -0.17305 \text{ s}^2/\text{m}^5 \times Q_0^2 - 6.87807 \text{ m}^3/\text{s} \times Q_0 + 42.00936\text{m}, \quad (\text{B.9})$$

where h_{pump} is the pumping head in m. When comparing different pumps for use in this system, their associated pump curve equations were utilized.

The selection of the pump and two globe valves was an iterative process; the pump was selected to produce the required flow at the estimated head, and the globe valves were selected so as to adequately control the pump's flow within this range. The use of the recirculation line allows excess water flow to be diverted back into the tank, meaning that the feed line globe valve did not need to throttle the pump between extremes of flow and pressure. Q_0 , Q_f , and Q_r depend heavily upon the degree to which each of the globe valves have been opened. The K values for the two valves are increased to demonstrate the effect of closing the valves to varying extents; both valves are capable of complete shutoff, so in theory, their K values can be increased to infinity. Table B.1 shows a selection of flow rates

available for a variety of valve settings using this method, demonstrating that the desired flow range is possible using this combination of valves and the selected pump.

B.3 NPSH

The available net positive suction head (NPSHa) expresses the amount of potential energy available in the fluid on the suction side of the pump. If the NPSH available dips below the NPSH required by the pump, the pump will be starved of fluid, and vapourization of the liquid will lead to cavitation, vibration, and eventually damage to the equipment. Because the hot water tank may drain to a very low level in two-tank mode, an NPSHa check was performed for the centrifugal feed pumps. For this calculation, the hot water supply pump is considered, since its higher water temperature puts it more at risk of cavitation.

Bachus and Custodio [50] break down NPSHa into every contributing element:

$$\text{NPSH}_a = H_a + H_s - H_{vp} - H_f - H_i, \quad (\text{B.10})$$

where NPSHa is the net positive suction head provided by the system, H_a is the head provided by the atmospheric pressure for a vented system, H_s is the static pressure contributed by the column of fluid, H_{vp} is the vapour pressure of the liquid at the working temperature, H_f is the system friction on the suction side of the pump, H_i is the head loss due to the geometry of the suction inlet.

The barometric pressure in the laboratory is often close to 92 kPa. This gives $H_a = 9.4$ m, since the tank is vented to the room. The tank may drain very low, so H_s may be as low as, say, 0.1 m. At 50°C, the head corresponding to the vapour pressure of water is about 1.264 m [50].

To find H_f , the velocity head is needed. Using a 2" pipe, the maximum velocity is

$$v = \dot{V}/A = \frac{4\dot{V}}{\pi D^2} = \frac{4 \times 4 \text{ L/s}}{\pi (0.0525 \text{ m})^2} = 1.85 \text{ m/s}. \quad (\text{B.11})$$

Here, 4 L/s is used, since the sum of the flows in the feed and recirculation lines may approach this flow rate. Therefore, the velocity head is

$$\frac{v^2}{2g} = \frac{(1.85 \text{ m/s})^2}{2 * 9.81 \text{ m/s}^2} = 0.1744 \text{ m}. \quad (\text{B.12})$$

Assuming minor losses due to an open ball valve ($K = 0.07$) and a sudden contraction from the tank to the outlet ($K = 0.5$) [49], and taking a rough friction factor of 0.02 and a short 0.58 m section of PVC pipe between the tank and the pump suction nozzle, friction head is estimated as

$$H_f = \left(f \frac{L}{D} + \Sigma K \right) \frac{v^2}{2g} = \left(0.02 \frac{0.58 \text{ m}}{0.0525 \text{ m}} + 0.57 \right) 0.1744 \text{ m} = 0.1379 \text{ m}. \quad (\text{B.13})$$

H_i is often taken at 0.61 m when the exact value is unknown [50]. Applying the above values in (B.10), the, overall NPSHa is determined to be:

$$\text{NPSHa} = 9.4 \text{ m} + 0.1 \text{ m} - 1.264 \text{ m} - 0.1379 \text{ m} - 0.610 \text{ m} = 7.5 \text{ m}.$$

This is a generous NPSHa, chiefly due to the fact that the hot water tank is open to atmosphere. The cold water feed pump is set up in the same way, but at a lower operating temperature; the value of H_{vp} is therefore less, yielding a slightly higher NPSHa for that case.

The selected pump (1 hp FAC-100S from Franklin Electric) does not have a listed NPSHr, but is designed for applications where the pump may be located above the water surface by 7.5 m (including friction losses) [51]. For argument's sake, assuming that the manufacturer has the pump operating at sea level, that the outdoor well temperature is moderate at 15°C ($H_v = 0.1768$ [50]), and that 7.5 m includes the friction losses in the pipe and at the suction port, this would correspond to an NPSHr of approximately

$$\text{NPSHr} = H_a + H_s - H_f - H_i - H_{vp} = 10.33 \text{ m} + -7.5 \text{ m} - 0.1768 \text{ m} = 2.7 \text{ m}.$$

As a general rule, the pump is suitable from the perspective of net positive suction head if $\text{NPSHa} > (\text{NPSHr} + 1 \text{ m})$, so even with this rough estimate, it is evident that there is no threat of cavitation due to lack of NPSHa.

B.4 Basin Drainage

The water levels in the basin and the sump are not constant, which means that the flow rate between the two is also not constant. However, a maximum flow rate out of the basin can be found by taking the maximum height of the water column in the basin and performing a simplified analysis with the Bernoulli equation. Figure B.2 is used as a reference throughout this analysis.

Assume that the sump level (B) is at floor level, as it might be at the beginning of operation. Assume that the pump keeps the sump empty (which is not the case, but reflects the greatest height difference between the water level in the two vessels). The maximum flow rate for the cooling tower is 3 L/s, so this is the volumetric flow rate of water that must be able to drain from the drainage basin down to the sump. Given the 2" pipe size, this gives a desired water velocity in the connecting pipe of

$$v = \frac{4 \times 0.003 \text{ m}^3/\text{s}}{\pi(0.05244 \text{ m})^2} = 1.4 \text{ m/s}. \quad (\text{B.14})$$

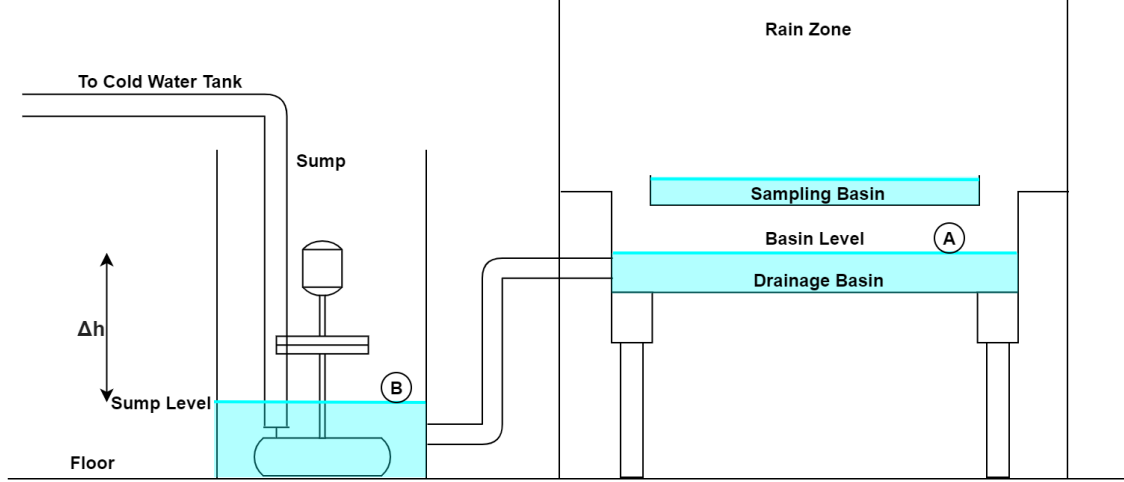


Figure B.2 – Basin and sump system

Assuming that the level of the water in the major basin remains constant and that atmospheric pressure is equal at free surfaces A and B, Bernoulli's equation reduces to

$$h = K \frac{v^2}{2g}, \quad (\text{B.15})$$

where h is the height of the drainage basin water level above that of the sump, and K is a minor loss coefficient. K is approximately equal to 2×0.95 (elbows) + 1 (sudden expansion) + 0.4 (sharp contraction) = 3.3 [49]. Pipe friction losses are ignored due to the generous pipe diameter and short length. Therefore, the maximum velocity of water through the pipe is

$$v = \dot{V}/A = \frac{4\dot{V}}{\pi D^2} = \frac{4 \times 0.003 \text{ m}^3/\text{s}}{\pi(0.0525 \text{ m})^2} = 1.4 \text{ m/s}. \quad (\text{B.16})$$

The height difference that would be needed for 3 L/s of flow would then be at least

$$h = \frac{3.3 \times (1.4 \text{ m/s})^2}{2 * 9.81 \text{ m/s}^2} = 0.33 \text{ m}. \quad (\text{B.17})$$

The current height of the top lip of the major basin is 45 cm, which suggests that the drainage basin will drain sufficiently for the range of flows in question. This analysis does not take into account how the height difference between the two vessels change as the sump fills; the sump pump switches on when the level switch reaches 20 - 28 cm. This setup is viable for most flow rates of interest, but may not drain quickly enough to keep up at the maximum flow rate of 3 L/s, depending upon the water level in the two vessels. If the tower must be used with a flow rate higher than this arrangement can drain, the basin can be raised further, although this reduces the amount of vertical space available in the cooling tower.

B.5 Sump Pump System

The sump pump's system curve is much simpler than that of the feed pump - it has only a single line that leads directly to the cold water tank, with no valves or branches included, as seen in Figure 3.2. Regardless of the flow rate of water added to the sump, the sump pump cycles on and off so as to discharge this water.

Although this system has the same transitional flow regime as the feed line, major losses are estimated assuming fully rough turbulent flow and $f = 0.02$. Minor losses at the sump pump discharge include a check valve ($K = 2.1$) and two elbows ($K = 2 \times 0.95$). The pipe length is approximately 3.5 m of NPS2 Sch 40 PVC, a relatively smooth material. Approximately this pipe includes a 1 m vertical column of water. Therefore, design head was calculated as

$$h = \left(f \frac{L}{D} + \sum K \right) \frac{v^2}{2g} + \Delta h = \left(0.02 \frac{3.5 \text{ m}}{0.0525 \text{ m}} + 4 \right) \frac{(1.4 \text{ m/s})^2}{2 \times 9.81 \text{ m/s}^2} + 1.0 \text{ m} = 1.5 \text{ m}.$$

A high-flow household sump pump such as the Little Giant 6EC easily met this requirement.

B.6 Cleanliness

The system water is a combination of domestic cold water and recycled condensate. Aside from Cortrol OS5300, which is included in the condensate as an oxygen scavenger (concentration on the order of parts per billion), no additives have been included in the water. To maintain relative cleanliness, the system water is drained every week.

Appendix C

Steam System Design

Steam heating was selected as the most practical and cost-effective means of warming the cooling tower feed water; a supply line of low pressure steam already existed in the laboratory. In the design of this system, the primary goals were:

- a) to minimize pressure loss where possible and maximize flow rate,
- b) to effectively drain and collect condensate formed at startup (as the pipes warm up) and during operation (from the heat exchanger), and
- c) to avoid water hammer and subsequent damage to the system, especially to steam traps and the heat exchanger.

An estimated 128 kW of heat is available from this system. The maximum flow rate of steam was estimated by employing the Bernoulli equation, similarly to Appendix B.

C.1 System Overview

In this heating arrangement, heat is transferred from a supply of steam to the cooling tower water by means of a heat exchanger. The condensed steam from the heat exchanger is collected and reused as makeup water at the cold water tank. A detailed sketch is shown in two parts in Figures C.1 and C.2. As-built details such as the pipe supports and geometry of the load trap drain and condensate receiver vent are slightly different than as drawn.

Steam is provided to the system by means of a 2" supply pipe. To ensure that the steam entering the thermostatic valve (TSV) and heat exchanger is dry, minimizing the risk of damage from water hammer, a drip line is installed in the supply line below the feed line. This allows liquid water to drain into the drip line, and prevents it from accumulating and entering the feed line. The drip line is affixed with a small float-and-thermostatic steam trap (Hoffman Specialty FT30H-3) to drain water but prevent the escape of steam. The steam trap's exit is piped to the receiver of a condensate unit (Hoffman Specialty Model

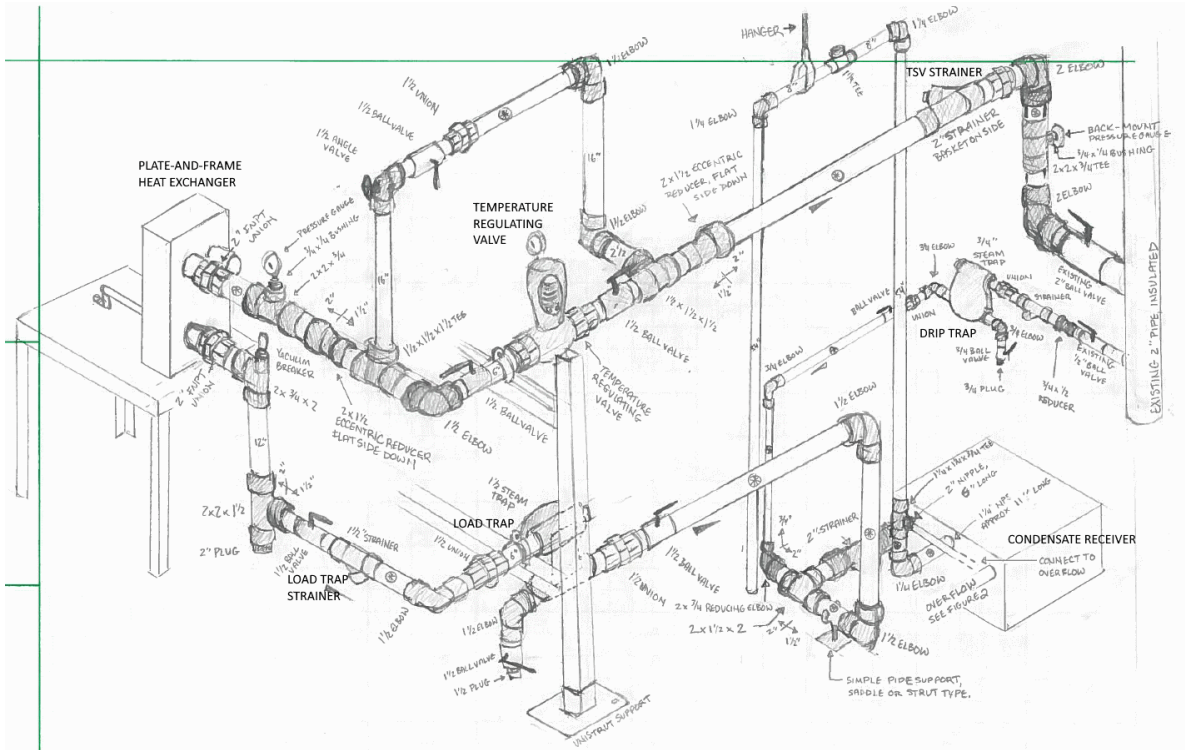


Figure C.1 – Steam system sketch: Steam and condensate arrangement

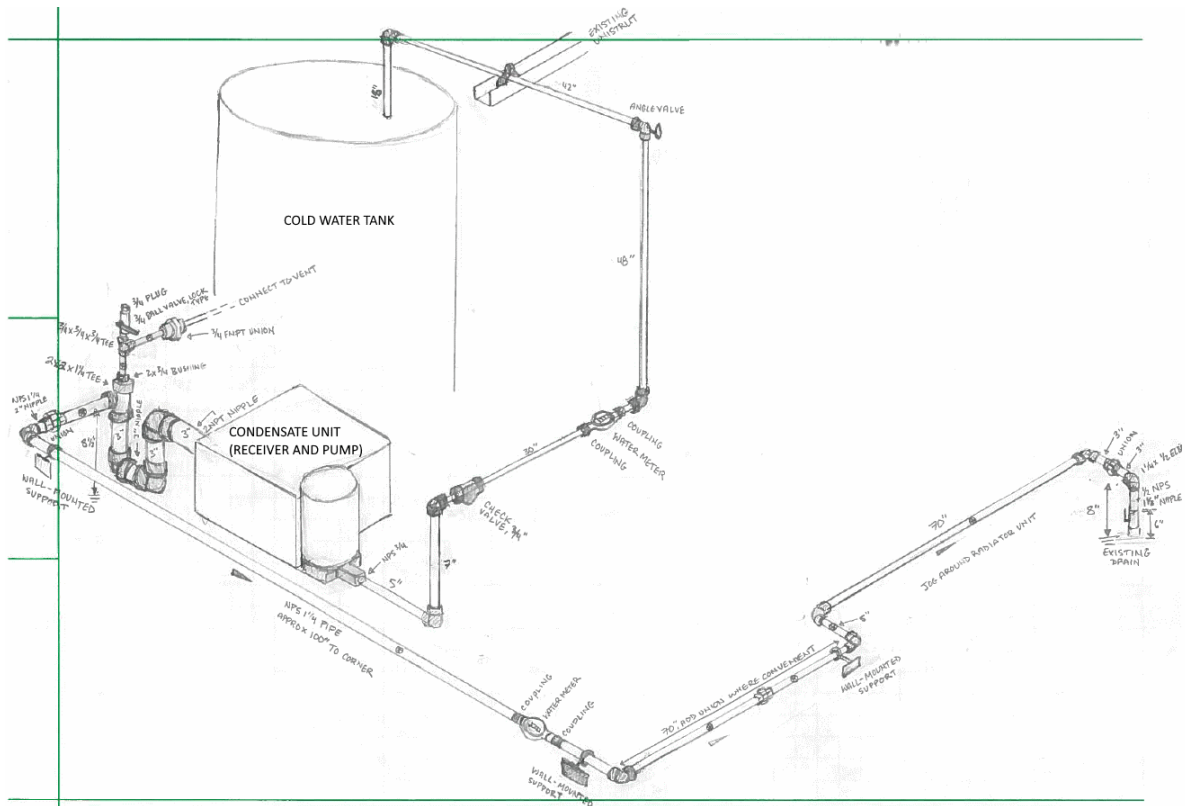


Figure C.2 – Steam system sketch: Condensate recycle and drain arrangement

WC6-20B), where the hot water is collected and pumped to the cold water tank for re-use. In the feed line, steam enters and passes through the TSV. This valve (Spence 2030TG-GQE) is adjusted based on the pressure produced in a temperature-sensing bulb inserted into the hot water exiting the heat exchanger. In this way, the TSV adjusts the amount of steam provided to the heat exchanger in order to maintain a certain hot water temperature. A bypass line is included in case the TSV needs service. Steam then travels to the plate-and-frame heat exchanger (Tranter SUPERCHANGER UXP-005-L-6-UI-28), where it loses heat and condenses. Immediately downstream of the heat exchanger, a vacuum breaker allows the steam trap downstream to drain condensate from the heat exchanger even when the on/off valve at the entrance of the feed line is closed. Without this vacuum breaker, there is a danger of creating a vacuum inside the heat exchanger which may pull water violently up and backwards through the steam trap, almost inevitably damaging equipment by means of water hammer. Downstream of the heat exchanger, a float-and-thermostatic steam trap (Hoffman Specialty FT30H-6) serves to remove air and liquid condensate while preventing loss of steam, and a vented condensate tank and pump (Hoffman Specialty Model WC6-20B) collects the hot condensate and returns it to the cold water tank as a source of make-up water. The vent line is raised above the height of the cold water tank and includes an opening at its high point to prevent back-siphoning of water from the cold water tank - a failsafe measure in addition to the check valve at the outlet of the condensate pump. In the unlikely event that hot condensate does travel up the vent, the vent line is piped downwards so that this hot water is discharged relatively safely towards the floor. An overflow line sends excess water from the condensate receiver and vent line to drain. Strainers are provided upstream of the TSV, both steam traps, and the condensate unit so as to keep these free of debris. Additional design details meant to reduce the likelihood of water hammer include the inclination of pipe so as to drain liquid water away from the heat exchanger, the installation of the steam strainer horizontally rather than with the basket facing downwards to avoid the collection of water in the basket, and the intentional use of eccentric reducers upstream and downstream of the TSV so as to provide no low point for water to accumulate.

C.2 Component Selection

The selection of major components in the steam system will be outlined in this section. Although each part is discussed in sequence, because the selection of certain components had an effect on the overall steam flow rate and pressure drop experienced by other components, the sizing of key components in the steam system was an intrinsically iterative process. The discussion below does not reflect this iteration, but does explain the criteria and equations which informed those selections.

2"	90° elbows	Tee branches
Estimated number	8	1
Eff. length/ea [52]	1.3 m	2.4 m
Added length	10.5 m	2.4 m
2-1/2"	90° elbows	Tee branches
Estimated number	2	1
Eff. length/ea [52]	1.5 m	3.4 m
Added length	3.0 m	3.4 m

Table C.1 – Effective lengths for steam line design

C.2.1 Valve Sizing

An estimate of steam flow rate is calculated by applying an expected pressure drop across the pipe system with known loss coefficients for its components. Because the supplied steam is provided at 5 psig and the system is ultimately vented to the ambient laboratory environment, the total pressure drop through the system must be 5 psig (34.5 kPa). This analysis will consider roughly 7.6 m of 2-1/2" pipe and 18.1 m of 2" pipe, and neglect losses from the much larger steam main upstream. If elbows and tees are expressed in terms of equivalent pipe length, these can be added to the previously stated pipe lengths to yield effective pipe lengths as shown in Table C.1. Sections of pipe which connect components near the heat exchanger are assumed to have negligible friction losses due to their short lengths.

The pressure drop across each piping section is calculated using a friction factor (calculated with Haaland's equation, assuming pipe roughness to be 0.045 mm) and the diameter of pipe used, employing the relationships

$$\Delta P_{p,i} = \frac{8f_i L_i \dot{m}^2}{\pi^2 \rho d_i^5}, \quad (\text{C.1})$$

and

$$\Delta P_p = \Delta P_{p,2-1/2''} + \Delta P_{p,2''}, \quad (\text{C.2})$$

where $\Delta P_{p,i}$ is the pressure drop experienced across a section of pipe with size i in Pa, ΔP_p is the total pressure drop due to piping in Pa, f_i is the Haaland friction factor for pipe i , L_i is the length of pipe i in m, \dot{m} is the mass flow rate of steam in kg/s, ρ is the density of steam in kg/m³ which can be found in Incropera's tables [53], and d_i is the inner diameter of pipe i in m.

If a thermostatic valve is added to the steam line, this valve will be responsible for another pressure drop as steam passes through it. Using the manufacturer's steam equation for the Series 2000 Temperature Regulator [54], which is expressed in imperial units,

$$\dot{m}_{lb/hr} = 3 \times C_v \sqrt{\Delta P_{psi} \times P_{o,psia}} \quad (\text{C.3})$$

where: $\dot{m}_{lb/hr}$ is the mass flow rate of steam in lb/hr, C_v is the flow coefficient, or the volume of water measured in US gpm at 60°F that will flow through a valve with a pressure drop of 1 psi,

$\Delta P_{TSV,psi}$ is the pressure drop across the thermostatic valve in psi,

$P_{o,psia}$ is the pressure at the valve outlet in psi (absolute).

For this analysis, it is more convenient to rearrange (C.3) and utilize the quadratic equation to solve for the pressure drop that the valve will cause, i.e.,

$$\Delta P_{TSV,psi} = \frac{P_{TSV,up,psia} - \sqrt{P_{TSV,up,psia}^2 - 4 \left(\frac{\dot{m}_{lb/hr}}{3C_v} \right)^2}}{2} \quad (C.4)$$

where:

$P_{TSV,up,psia}$ is the pressure upstream of the valve in psia ($P_{atm,psi} + P_{up,psi} - \Delta P_{pipe,psi} - \Delta P_{strainer,psi}$), and $P_{up,psi}$ is the supplied upstream pressure in psi (gauge).

A similar equation from the strainer manufacturer can be used to determine the pressure drop created by the addition of a strainer whose flow coefficient (C_v) is provided [55], i.e.,

$$\dot{m}_{lb/hr} = 2.1C_v \sqrt{\Delta P_{psi}(P_{strainer,up,psi} - P_{strainer,down,psi})}, \quad (C.5)$$

where $P_{strainer,up,psi}$ and $P_{strainer,down,psi}$ are the absolute pressures upstream and downstream of the strainer in psia. This expression can be used to calculate the pressure drop for the strainers upstream of the TSV and the load steam trap: their respective C_v values are approximately 89 and 63 [55]. To calculate the pressure drop across the strainer, the quadratic formula can be employed and reduced to the following:

$$\Delta P_{strainer,psi} = P_{strainer,up,psi} - \sqrt{P_{strainer,up,psi}^2 - \left(\frac{\dot{m}_{lb/hr}}{2.1C_v} \right)^2}. \quad (C.6)$$

The TSV and strainer pressure drops calculated in psi using imperial manufacturer equations are then converted to Pa.

The pressure drop through the heat exchanger is small. Using the pressure drop at two flow rates listed on the datasheet provided by the manufacturer, the pressure drop across the heat exchanger at any steam flow rate can be estimated as:

$$\Delta P_{HX} = 705718 \frac{1}{m} \times \dot{m}^2 \quad (C.7)$$

where ΔP_{HX} is the pressure drop across the heat exchanger in Pa.

The most accurate way to estimate the pressure drop across the steam trap downstream of the heat exchanger is to use the manufacturer’s tables that compare flow rate and differential pressure. This does not account for the sometimes-cyclical nature of the steam trap’s operation, but it should be a reasonable approximation. Using a recent datasheet for Hoffman Specialty Series H Float and Thermostatic Steam Traps [55], a curve was fit to the data for the 1-1/4” model, yielding:

$$\Delta P_{\text{trap},1-1/2} = (69.83 \frac{\text{s}^{0.344}}{\text{kg}^{0.672} \text{m}^{0.328}} \times \dot{m})^{3.049}, \quad (\text{C.8})$$

where ΔP_{trap} is the pressure drop across the steam trap in Pa. For better fit of the curve to data at low flow conditions, only data up to a ΔP of 5 psi was included in the curve fit.

The total pressure drop from source to vent (downstream of the steam traps) should be equal to the sum of all the pressure drops incurred along the way, i.e.,

$$P_{up} = \Delta P_p + \Delta P_{\text{strainer1}} + \Delta P_{\text{TSV}} + \Delta P_{\text{HX}} + \Delta P_{\text{strainer2}} + \Delta P_{\text{trap}}, \quad (\text{C.9})$$

where P_{up} is the upstream line pressure in Pa.

The steam flow rate \dot{m} is solved for using (C.9), making P_{up} equal to 5 psi (34.5 kPa). To compare different steam traps, different steam trap equations can be substituted in. To compare different thermostatic valves, the value of C_v in (C.4) can be altered. Oversizing the valve results in poor control, while undersizing restricts the maximum flow rate. For good performance, ASHRAE recommends that the control valve be sized to contribute at least 25 to 50% of the total available pressure drop - this is referred to as valve authority [33]. In Jon Monsen’s article, he presents these rules of thumb [56]:

- Valve should be 60 to 80% open at maximum required flow rate
- Valve should be not much less than 20% open at minimum flow rate
- Properly sized globe valves are usually one size smaller than the line

The TSV was sized by varying C_v , and by comparing authority and maximum flow rate, considering an inlet pressure of 5.0 psig and an atmospheric pressure of 13.5 psi (93 kPa), which corresponds to a steam density of 0.741 kg/m^3 [53].

A double-seated 1-1/2” valve was selected to provide a compromise, allowing a relatively high maximum steam flow rate while still offering excellent system authority. Using the Spence 2030TG-GQE temperature regulating valve, having a C_v of 24.8, the steam system described above can be solved to yield a total flowrate of $\dot{m} = 206 \text{ kg/hr} = 454 \text{ lb/hr}$, which

provides 128 kW of latent heat. Pressure drop across the valve is predicted to be $\Delta P_{TSV} = 18000 \text{ Pa} = 2.6 \text{ psi}$; compared to the total system pressure drop of 5 psi, this valve provides just over 50% authority in the system in accordance with ASHRAE's recommendations [33]. For comparison, the pressure loss due to pipe friction was 9900 Pa (1.4 psi), the pressure drop across the TSV strainer was 1200 Pa (0.2 psi), the pressure drop across the heat exchanger was 2300 Pa (0.3 psi), the pressure drop across the load trap strainer was 2960 Pa (0.4 psi) and the pressure drop across the steam trap was only 68 Pa.

C.2.2 Steam Traps

The role of a steam trap is to allow liquid water and air to pass through them, while simultaneously preventing the escape of steam. Float-and-thermostatic (F&T) steam traps were selected for both the drip line and heat exchanger. ASHRAE calls these the drip trap and the load trap, respectively [36]. These traps are designed specifically to allow liquid condensate to pass through them quickly without delay by means of a float mechanism. This is in contrast with a thermostatic radiator steam trap, which must wait for the condensate to cool before allowing it to be evacuated to the drain. In addition to the float mechanism which drains liquid water, F&T traps have a thermostat element which allows air to escape. The air and water are both discharged through the same port to leave the steam trap [52, 57]. Steam trap sizes are selected based on a) maximum flow rate of condensate and b) minimum ΔP expected across the trap.

Drip Trap Sizing

The role of the drip trap is to remove liquid water from the supply line and keep the feed line dry. Most liquid water will accumulate in the line during system warm-up; when the lines are opened, steam will rush into the cold pipes and will condense on their walls until the pipes reach the steam temperature. If this liquid water is able to travel into the feed line, it can inhibit heat transfer and cause water hammer. Therefore, the drip trap must be designed to eliminate the volume of liquid water generated at system start-up during the time it takes for the system to warm up.

Startup Condensate Volume: The mass of each size of pipe can simply be found in standard tables. Estimating the upstream lengths of steam-carrying pipe, the overall mass of pipe that must be warmed up can be determined.

From the main header, approximately 7.6 m of 2-1/2" pipe and 3.1 m of 2" pipe leads into the laboratory. Liquid water in this pipe will drain to the drip trap. In the laboratory itself, approximately 15 m of 2" pipe connects to the system pictured in Figures 3.4 and C.1. In the

Pipe Nominal Size	Weight/Length (kg/m)	Length (m)	Weight (kg)
Sch 40 1-1/2"	4.05	3.3	13.5
Sch 40 2"	5.44	2.1	11.4
Sch 80 2"	7.49	18.1	135.6
Sch 80 2-1/2"	11.41	7.6	86.7

Table C.2 – Mass contributed by different sizes of steam pipe

system itself, approximately 2.1 m of 2" pipe and 3.3 m of 1-1/2" pipe drains back towards the drip trap. The system piping is standard thickness (Schedule 40) while the supply pipe is extra strong (Schedule 80). Their respective weights are summarized in Table C.2.

Neglecting extra mass contributed by valves and fittings, the pipe amounts to a total mass of 247.3 kg. A specific heat capacity of 460.5 J/kg·K will be assumed the steel pipe, assuming plain carbon steel at 350 K [53]. Knowing that the temperature of steam provided at 5 psi will be close to 107°C, and assuming that the temperature of the laboratory is close to 22°C, this 247.3 kg of steel pipe will need to be warmed by 85°C to attain steady state, neglecting heat transfer through the pipe insulation. Knowing that the latent heat of steam is approximately 2239 kJ/kg, the amount of steam which will need to be condensed to warm these pipes up to operating temperature can be calculated as follows:

$$m_c = \frac{m_p c_p \Delta T}{h_{fg}} = \frac{(247.3 \text{ kg})(0.4605 \text{ kJ/kgK})(85 \text{ K})}{2239 \text{ kJ/kg}} = 4.32 \text{ kg}, \quad (\text{C.10})$$

where

m_c is the mass of startup condensate in kg,

m_p is the mass of pipe in kg,

c_p is the specific heat capacity of the pipe in kJ/kg·K,

ΔT is the expected temperature rise in K, and

h_{fg} is the latent heat of water in kJ/kg·K.

Using the density of saturated water at 380 K and 1.2869 bar (close to 5 psi) from Incropera of 0.953 kg/m³, m_c is found to be 4.53 L.

Warmup Time: The time it takes for the pipe to experience this heating will be approximated using the lumped capacitance method. For this analysis, warmup will be considered complete when the temperature difference between the pipe and the ambient air has been reduced by 99%. Since the heat transfer occurring will be dominated by the condensation of the steam on the pipe walls, temperature change over time can be estimated by using:

$$\frac{m_p c_p}{h A_p} \int_{\Theta_0}^{\Theta_{t_f}} \frac{d\Theta}{\Theta} = - \int_0^{t_f} dt, \quad (\text{C.11})$$

Pipe Nominal Size	ID (mm)	Length (m)	Area (m ²)
Sch 40 1-1/2"	40.9	3.3	0.43
Sch 40 2"	52.6	2.1	0.35
Sch 80 2"	49.3	18.1	2.80
Sch 80 2-1/2"	58.9	7.6	1.41

Table C.3 – Surface area inside steam pipe

where m_p is the mass of pipe in kg, c_p is the specific heat capacity of the pipe in J/kg-K, h is the convective heat transfer coefficient in W/m²K, A_p is the inner surface area of pipe in m², Θ is the temperature difference between the pipe and the ambient temperature in K, and t is time in seconds, t_f being the warmup time. Integration results in an expression for the warmup time, i.e.,

$$\frac{m_p c_p}{h A_p} \ln \frac{\Theta_0}{\Theta_{t_f}} = t_f. \quad (\text{C.12})$$

Because h is difficult to determine, the lowest convective heat transfer coefficient suggested by Incropera et al. [53] for convection with phase change will be assumed: 2500 W/m²K. Internal surface area is estimated using the known internal diameters and estimated lengths of the pipe, summarized in Table C.3. The total area available for heat transfer is 4.99 m². For the temperature difference between the pipe and ambient to be narrower by 99%, $\Theta_i/\Theta = 100$. The expression given in (C.12) can then be solved:

$$t_f = \frac{m_p c_p}{h A_p} \ln \frac{\Theta_0}{\Theta_{t_f}} = \frac{(247.26 \text{ kg})(460.5 \text{ J/kgK})}{(2500 \text{ W/m}^2\text{K})(4.99 \text{ m}^2)} \ln(100) = 42.06 \text{ s}.$$

Knowing now that condensate might accumulate as quickly as 42 s, ideally, the condensate should be drained away in that time, i.e.,

$$\dot{m}_c = \frac{4.32 \text{ kg}}{42 \text{ s}} \times \frac{3600 \text{ s}}{\text{hr}} = 370 \text{ kg/hr} = 816 \text{ lb/hr} \quad (\text{C.13})$$

Since 5 psi (34.5 kPa) is expected in the supply lines (minus some losses from travelling through narrow pipes), the pressure at the drip line can be conservatively estimated as 2 psi (13.8 kPa). The Hoffman FT030H-3 3/4" steam trap offers 870 lb/hr (394.6 kg/hr) at a differential pressure of 2 psi, so it is suitable for this purpose. Flow through this steam trap will likely exceed 870 lb/hr, since the pressure at the trap is likely to be closer to 5 psi.

Load Trap

The load trap is sized in a similar way, but in this case, the condensate produced by the heat exchanger is the main concern. From the valve sizing calculation, the flow rate of steam (and therefore, the accumulation of condensate) has been estimated to be a maximum

of 454 lb/hr (206 kg/hr). The load trap should be sized for a differential pressure of only 1/4 psi (1.7 kPa) - this is the pressure that the steam trap will experience due to static head alone when the control valve to the heat exchanger shuts off, halting the flow of steam. The vacuum breaker just after the heat exchanger's condensate outlet will let in air to prevent a vacuum from forming inside the heat exchanger, and the static pressure of the column of condensate sitting above the steam trap will provide some small pressure to allow the water to drain [52]. A vertical leg of pipe has been included between the heat exchanger and the steam trap so as to ensure a column of water to produce this differential pressure. The mass flow rate of 454 lb/hr can be met with a FT030H-6 1-1/2" F&T trap, which provides 580 lb/hr at a differential pressure of 1/4 psi.

C.2.3 Condensate Receiver and Pump

According to Edmondson and Hall [58], condensate receivers are normally sized to hold the condensate produced in 1 min. Assuming 202 kg/hr of steam flow as calculated above, 3.6 L of condensate would accumulate in 1 min, which is equivalent to 0.8 gallons. Including a safety factor of 1.5, the condensate receiver need only be 1.2 gallons large.

Condensate pumps are selected to handle twice the expected condensing rate; 1.6 gpm in this case. The pumping head required by the condensate pump is only enough to get into the cold water tank, only 115 cm, but Edmondson and Hall [58] recommend 5 psig on top of this. With a design point of 1.6 gpm at about 7 psi discharge pressure, only a small pump is needed. The smallest of the cast iron Watchman series condensate units from Bell & Gossett, the WC6-20B, has a receiver capacity of 6 gallons, and a pumping capacity of 8 gpm at 22 psi [59], and was selected for use in this steam heating system. The provided pump was larger than required, so a small valve was installed on the discharge piping to throttle the flow back to a reasonable rate.

Appendix D

Instrumentation

D.1 Instruments

Water Flow: For the measurement of water flow rate, a turbine flowmeter was used (Omega FTB694-NPT-P). It was selected as a cost-effective option to measure total water flow with $\pm 3\%$ reading accuracy while incurring a minimal pressure loss to the system.

Pitot Tube: For point measurements of air velocity, a pitot tube was selected (Dwyer 160F Straight Pitot Tube). The straight shape of this particular model was convenient for locating the probe at different locations within the cooling tower. Although the pitot tube could become clogged with water spray, it is not otherwise vulnerable to deleterious effects of water droplets. Its accuracy is reported as ± 0.9 m/s.

Air Flow and Differential Pressure: A thermal flow measurement chip (FirstSensor LMIS025UB3S) was selected to measure the pressure differential experienced by the pitot tube (up to a maximum of 25 Pa). This particular model was selected due to its low range, good accuracy, and resistance to humid conditions. The chip signals were interpreted by an Arduino, which connected to a computer running LabView to display and record the readings. The manufacturer rates the accuracy of the LMI25 at $\pm 1.5\%$ of reading ± 0.1 Pa. In Section 4.1.3, the Fluke 922 is also used to measure velocity. This sensor's rated accuracy is ± 0.25 m/s for velocity measurements [60].

Differential Pressure: For cases where differential pressure was to be measured in excess of 25 Pa, the Fluke 922 airflow meter was used. This unit has an accuracy of $\pm 1\% + 1$ Pa, and resolution of 1 Pa [60]. Because it could not record and export data, measurements from the Fluke 922 were recorded by hand. In each case, the built-in averaging function of the Fluke 922 was used to obtain average pressure readings over a period of at least five seconds.

Averaging Pitot Tube Grid: An averaging pitot tube grid (Dwyer STRA-R22X22) was selected for total airflow measurement. Multiple openings throughout the duct cross section connect to a total- and static-pressure manifold, and the difference in pressure between these two manifolds gives a total flow rate, averaged “mechanically” rather than mathematically. The LMI airflow sensor is used to measure this minute pressure difference and to calculate the total airflow. This device includes a honeycomb-grid flow straightener immediately upstream in order to reduce the requisite length of straight ductwork on the upstream side. Critics of such devices point out that the “mechanical average” applies more weight to the openings closest to the measurement port [41]. In this case, the measurement ports to which the LMI sensor are connected are attached to the averaging tubes in the duct’s center, as shown in Figure 4.13 and discussed in Section 4.1.6. This averaging pitot tube is reported to have an accuracy of $\pm 2\%$ of reading.

Thermocouples: For measurement of water temperature, J-type thermocouples are used. For a standard grade, J type thermocouple, Lipták gives these as $\pm 4^\circ\text{F}$ ($\pm 2.2^\circ\text{C}$) or 0.75%, whichever is greater [41]. The thermocouples are connected to a DAQ card from National Instruments connected by USB to a computer where the readings are displayed and recorded.

Appendix E

Error Analysis

Using the uncertainties given in Appendix D, the uncertainties associated with each individual measurement and each value calculated from those measurements can be determined by error propagation. These uncertainties will be calculated in detail here, using Taylor's text on error analysis as a guide [61].

When a calculated quantity q is a function of several variables ($x \dots z$) whose uncertainties are independent and random, the uncertainty in q is

$$\delta q = \sqrt{\left(\frac{\partial q}{\partial x} \delta x\right)^2 + \dots + \left(\frac{\partial q}{\partial z} \delta z\right)^2}. \quad (\text{E.1})$$

If the uncertainties are not independent and random, the uncertainties must be simply summed as

$$\delta q = \left|\frac{\partial q}{\partial x}\right| \delta x + \dots + \left|\frac{\partial q}{\partial z}\right| \delta z. \quad (\text{E.2})$$

E.1 Total Pressure

LMI: FirstSensor provides a typical and a maximum error associated with this sensor. For purposes of error analysis, the maximum errors have been assumed. These include a bias error of ± 0.1 Pa and a span accuracy of $\pm 1.5\%$ of reading [40]. Thermal effects have been neglected for the dry and cold water tests included in this thesis because of the consistency of air temperature.

Fluke: When differential pressures are in excess of 25 Pa, a Fluke 922 airflow sensor is used instead. This device can measure much larger pressure drops, and has a listed accuracy $\pm 1\% + 1$ Pa and a resolution of 1 Pa [60]

When total pressure traverses are performed inside the cooling tower, the 160F pitot tube is used. The effect of the pitot tube on such pressure measurements has not been provided by the manufacturer, and so is not considered in the uncertainty of total pressure measurements. Therefore, the uncertainties associated with total pressure readings are

- LMI: $\pm 1.5\%$ of reading ± 0.1 Pa, and
- Fluke: $\pm 1\%$ of reading ± 1 Pa.

E.2 Air Density

Ambient conditions are used to calculate the saturation vapour pressure, ambient vapour pressure, humidity ratio, and ultimately, the density of air.

SHT31: The manufacturer lists typical and maximum errors from this sensor for temperature and humidity across a range of operating conditions. Air temperature is measured with a typical error of $\pm 0.2^\circ\text{C}$ and a maximum error of $\pm 0.4^\circ\text{C}$ (between 0 and 85°C). Relative humidity is measured with a typical error of $\pm 2.0\%$, and a maximum error of $\pm 2.5\%$ (up to an RH of 90%) [62]. The maximum errors have been assumed for purposes of propagation.

BME680: Best accuracy for this pressure sensor is attained between 30 and 110 kPa and between 0 and 65°C . Under these operating conditions (which are always met for this experiment), the accuracy of this sensor is given as ± 60 Pa [63]. Because the ambient temperature is very consistent in the laboratory, drift of pressure readings with changes in ambient temperature has been neglected.

The saturation vapour pressure is calculated based on the Hyland-Wexler method outlined by ASHRAE [36], i.e.,

$$P_{ws} = e^{C_1/T + C_2 + C_3T + C_4T^2 + C_5T^3 + C_6\log(T)}, \quad (\text{E.3})$$

where P_{ws} is the saturation vapour pressure (in Pa) at temperature T (in K), and C_1 through C_6 are constants:

$$C_1 = -5800.2206,$$

$$C_2 = 1.3914993,$$

$$C_3 = -0.048640239,$$

$$C_4 = 0.000041764768,$$

$$C_5 = -0.000000014452093, \text{ and}$$

$$C_6 = 6.5459673.$$

The error associated with the ambient temperature measurement must be propagated through this complex relation term-by-term. Taking the uncertainty of the equation itself as negligible,

$$\delta_1 = C_1 \frac{\delta_T}{T^2}, \quad (\text{E.4})$$

$$\delta_2 = 0, \quad (\text{E.5})$$

$$\delta_3 = C_3 \delta_T, \quad (\text{E.6})$$

$$\delta_4 = 2C_4 \delta_T T, \quad (\text{E.7})$$

$$\delta_5 = 3C_5 \delta_T T^2, \quad (\text{E.8})$$

and

$$\delta_6 = C_6 \frac{\delta_T}{T}. \quad (\text{E.9})$$

Because each of these terms includes T , none are independent from one another. Therefore, the errors associated with each term are added, yielding

$$\delta_{\text{exponent}} = |\delta_1| + |\delta_2| + |\delta_3| + |\delta_4| + |\delta_5| + |\delta_6|. \quad (\text{E.10})$$

The uncertainty in P_{ws} due to uncertainty in T is therefore

$$\delta_{P_{ws}} = P_{ws}(\delta_{\text{exponent}}) = P_{ws}(|\delta_1| + |\delta_2| + |\delta_3| + |\delta_4| + |\delta_5| + |\delta_6|). \quad (\text{E.11})$$

For the very consistent ambient temperature in the laboratory, this uncertainty in saturation vapour pressure amounts to 12%. The ambient vapour pressure is determined from this saturation vapour pressure and the measured ambient humidity, using

$$P_w = RH \times P_{ws}, \quad (\text{E.12})$$

where P_w is the ambient vapour pressure and RH is the relative humidity. The uncertainty in P_{ws} depends only on the uncertainty in ambient temperature, which is independent from the uncertainty in relative humidity. Therefore, the uncertainty in this calculated vapour pressure can be found as

$$\delta_{P_w} = P_w \sqrt{\left(\frac{\delta_{RH}}{RH}\right)^2 + \left(\frac{\delta_{P_{ws}}}{P_{ws}}\right)^2}, \quad (\text{E.13})$$

where δ_{RH} is equal to the error in the humidity measurement by the SHT-31 sensor, and $\delta_{P_{ws}}$ is defined in (E.11). The ambient humidity ratio is calculated using vapour pressure and total ambient pressure, using

$$w = \frac{0.62198P_w}{P - P_w}, \quad (\text{E.14})$$

where w is the humidity ratio in kg/kg, P_w is vapour pressure in Pa, and P is the total ambient pressure in Pa. P is measured independently from T and RH, so it is again independent from P_w . The uncertainty of w can therefore be quantified using

$$\delta_w = \sqrt{\left(\left|\frac{0.62198P}{(P - P_w)^2}\right|\delta_{P_w}\right)^2 + \left(\left|\frac{0.62198P_w}{(P - P_w)^2}\right|\delta_P\right)^2}, \quad (\text{E.15})$$

where δ_{P_w} is defined in (E.13), and δ_P is the error in the ambient pressure measurement associated with the BME680 sensor. The overall density of the air-vapour mixture is then calculated using

$$\rho = \frac{(1 + w)P}{RT(1 + 1.6078w)}, \quad (\text{E.16})$$

where ρ is the density of air, and R is the gas constant of dry air, 287.08 J/kgK. Although T and P are independent of one another, w depends on both, so the uncertainties here must be simply added rather than using the Euclidean norm.

$$\delta_\rho = \left|\frac{0.6078P}{RT(1 + 1.6078w)^2}\right|\delta_w + \left|\frac{1 + w}{RT(1 + 1.6078w)}\right|\delta_P + \left|\frac{(1 + w)P}{RT^2(1 + 1.6078w)}\right|\delta_T, \quad (\text{E.17})$$

where δ_w is defined in (E.15), δ_P is the error in the ambient pressure measurement by the BME680 sensor, and δ_T is the error in the ambient air temperature measurement by the SHT-31 sensor. Typical values of δ_ρ for the ambient conditions observed in the laboratory range from 0.0025 to 0.0029 kg/m³, suggesting good accuracy in the measurement of density for this combination of sensors.

E.3 Velocity

The uncertainty in velocity measurements is due to the combined uncertainties of the differential pressure sensor, the pitot tube, and the computed air density.

The LMI differential pressure sensor is used to take measurements used to determine velocities at point locations. The accuracy of the LMI sensor is given by the manufacturer as $\pm 1.5\%$ of reading ± 0.1 Pa. The manufacturer also instructs the user to apply an ambient pressure correction to these readings, as shown in (4.6). This correction introduces an additional error to the differential pressure reading due to uncertainty of the ambient pressure sensor, i.e.,

$$\delta_{\Delta P, \text{corr}} = \Delta P_{\text{corr}} \sqrt{\left(\frac{\delta_{\Delta P}}{\Delta P}\right)^2 + \left(\frac{\delta_P}{P}\right)^2}, \quad (\text{E.18})$$

where $\delta_{\Delta P}$ is the uncertainty in the differential pressure measurement associated with the LMI sensor, and δ_P is the uncertainty in the ambient pressure associated with the BME680 sensor.

When velocity is calculated using (4.9), this error from the corrected differential pressure must be compounded with that of the density and of the pitot tube. The pitot tube precision was estimated as ± 0.8 m/s in Section 4.1.5. Because of the pressure correction applied to ΔP , its term is not regarded as independent from the density term, so the uncertainty in velocity is the simple sum of the three uncertainties listed, that is,

$$\delta_v = \left| \frac{1}{\sqrt{2\rho\Delta P}} \right| \delta_P + \left| \frac{\sqrt{\Delta P}}{\sqrt{2\rho^3}} \right| \delta_\rho + \delta_{\text{pitot}}, \quad (\text{E.19})$$

where δ_P is the uncertainty in P from the BME680 sensor, δ_ρ is as given in (E.17), and δ_{pitot} is ± 0.8 m/s. In regions where the measured dynamic pressure is very low (below 1 m/s), the error in the $\delta_{\Delta P, \text{corr}}$ term can be significant. However, the error in δ_v is dominated by δ_{pitot} in all cases. Typical values for δ_v are around ± 1.0 m/s, dominated by the pitot tube precision error.

E.4 Static Pressure

E.4.1 Static Pressure Maps

The extra constant applied to the standard pitot tube equation shown in (4.9) implies that the pressure difference measured between the two ports is somewhat larger than the dynamic pressure - the total pressure port facing the flow should still be measuring total pressure, but the static pressure port downstream must be measuring a pressure slightly less than the true static pressure due to the geometry of the pitot tube. Therefore, the “static” port was not used to measure static pressure - instead, total pressure was measured, and the dynamic pressure calculated from the measured velocity was subtracted from this to ascertain the static pressure at any given point, i.e.,

$$P_{\text{static}} = P_{\text{total}} - \frac{\rho v^2}{2}. \quad (\text{E.20})$$

Therefore, the uncertainties in the measured total pressure, the calculated air density, and the calculated air speed must be propagated to determine the accuracy of the static pressure.

$$\delta P_{\text{static}} = \delta P_{\text{total}} + \left| \frac{v^2}{2} \right| \delta \rho + |\rho v| \delta v, \quad (\text{E.21})$$

where δP_{total} is the error in total pressure measurement associated with the LMI or Fluke 922 sensor (whichever is used), δ_{ρ} is as given in (E.17), and δ_v is as given in (E.19). Because

total pressure was sometimes measured with the Fluke 922 and sometimes measured with the LMI, the uncertainties in the resulting static pressure will be slightly different. In either case, the uncertainty in the static pressure is dominated by the uncertainty in the air velocity measurement, unless the air velocity is nearly zero. Regardless of whether the LMI or Fluke 922 sensor is used, static pressure uncertainties range from 1 to 6 Pa depending upon local air velocity.

E.4.2 Static Pressure Taps

These readings are subject to the same error associated with Total Pressure Drop measurements from Section E.1 depending upon which differential pressure sensor is used. However, systematic error cannot be easily quantified; the arrangement of PVC sheets comprising the fill and the spare fill sheet padding the space between the fill and the cooling tower wall may prevent static pressure from equalizing throughout the fill cross section. For the fill-high, fill-center, and fill-low locations, this effect may prevent the sampling of a static pressure representative of the fill cross section.

E.5 Static Pressure Drop

Static pressure drop is measured by taking the difference of two computed static pressures, $\delta P_{s,1}$ and $\delta P_{s,2}$, typically across a key component. Since the static pressures are averages over the 25-point field, $\delta P_{s,1}$ and $\delta P_{s,2}$ are the result of

$$\delta P_{\text{static}} = \frac{1}{25} \sqrt{\sum_{i=1}^{25} \delta P_{\text{static},i}^2}, \quad (\text{E.22})$$

where $\delta P_{s,i}$ is calculated using (E.21). Because δP_{static} is dominated by the velocity term defined by precision error, the uncertainties are considered independent and random. The dominance of the velocity term also means that the highest error in static pressure drop will likely be in a plane with the largest peak velocities. Therefore, as an example, consider the fill-low plane of an empty tower from Figure 4.18. For this plane, uncertainty in static pressure varies from 0.6 to 6 Pa depending on the local velocity. The error in the static pressure averaged across this plane, using (E.22), is 3.5 Pa.

If the difference is taken between the average static pressure for two different planes, the uncertainties of the two must be propagated together. Although the static pressures are measured using the same set of instruments in the same fashion, because they are measured separately, random and systemic uncertainties in the two sets of measurements have the opportunity to cancel one another out. Therefore, the difference between the two static

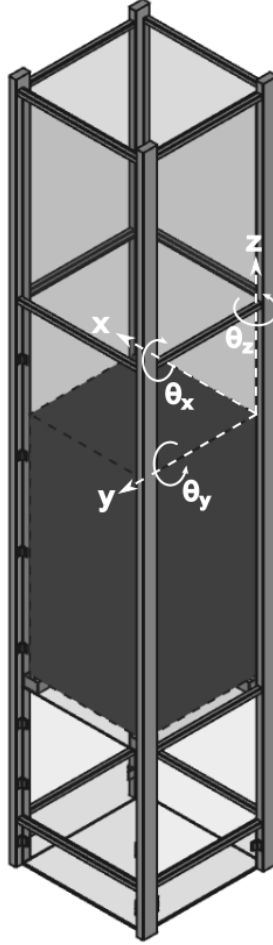


Figure E.1 – Coordinate system for analysis of spatial errors

pressures should be treated as that between independent variables, i.e.,

$$\delta\Delta P_{\text{static}} = \sqrt{(\delta P_{\text{static},1})^2 + (\delta P_{\text{static},2})^2}. \quad (\text{E.23})$$

Using the example of the fill-low plane as a case with higher uncertainty in static pressure, (E.23) can be used to show that the uncertainty of the difference between two average static pressures with uncertainty of 3.5 Pa is 5 Pa. As a result, all static pressure differences discussed in this work can be considered to be within ± 5 Pa or better.

E.6 Spatial Coordinates inside the Cooling Tower

The spatial coordinates of the point measurements taken inside the cooling tower with the pitot tube are also subject to uncertainty. Referring to Figure E.1, each traverse measurement point will be broken down into its components in the x , y , and z directions.

x refers to the distance through the width of the tower - five holes are drilled into the

Table E.1 – Summary of components of spatial error

Component	$\delta_{\text{,drilled}}$ (mm)	$\delta_{\text{,insertion}}$ (mm)	δ_{Θ_z} (degrees)
x	3		0.3
y		8	0.3
z	3		5

tower wall along the back face at numerous height intervals, and the pitot tube is inserted through the hole at the desired width. Errors in x arise from inaccuracies in the drilling of these holes, and from the angle of the pitot tube across the horizontal plane, Θ_z , which is not accounted for by the spirit level. Uncertainties in the location of the drilled hole are bias errors, estimated at 3 mm, whereas uncertainties in the angle of the pitot tube are random, estimated at $\pm 4^\circ$.

y refers to the distance through the depth of the tower - the pitot tube is inserted to the desired depth. The $\delta_{y,\text{insertion}}$ uncertainty includes both the errors in locating the markings on the pitot tube to allow the experimentalist to quickly and easily adjust the pitot tube to the correct insertion depth (a bias), and the random human error of the experimentalist lining these marks up with the wall of the cooling tower. The acrylic wall of the cooling tower is 6 mm thick, and although it is transparent, the walls of the probe holes drilled through it are cloudy from abrasion. Therefore, the experimentalist has the opportunity to line up the markings slightly differently each time. Combined, the error of the marking locations and the experimentalist's placement of the tube is estimated as ± 8 mm.

z refers to the distance along the height of the tower, and is controlled by selection of the probe holes the pitot tube is inserted into. Errors in z arise from inaccuracies in the drilling of these holes, and from the angle of the pitot tube across the horizontal plane, Θ_x . Uncertainties in the location of the drilled hole are bias errors, estimated at 3 mm, whereas uncertainties in the angle of the pitot tube are random, estimated at $\pm 0.3^\circ$ due to the use of a spirit level.

From the uncertainties summarized in Table E.1, the total uncertainties in x , y , and z can be evaluated from trigonometric relations, i.e.,

$$\delta_x = \delta_{x,\text{drilled}} + L \cos(\delta_{\Theta_x}) \sin(\delta_{\Theta_z}), \quad (\text{E.24})$$

$$\delta_y = \delta_{y,\text{insertion}} + L(1 - \cos(\delta_{\Theta_x}) \cos(\delta_{\Theta_z})), \quad (\text{E.25})$$

and

$$\delta_z = \delta_{z,\text{drilled}} + L \sin(\delta_{\Theta_x}) \cos(\delta_{\Theta_z}), \quad (\text{E.26})$$

Table E.2 – Summary of spatial uncertainties

L (mm)	δ_x (mm)	δ_y (mm)	δ_z (mm)
48	6	8	3
186	16	8	4
323	26	9	5
459	35	9	5
597	45	9	6

where L is the inserted length in mm. The second term in (E.25), the error in y due to angling of the pitot tube, can only decrease y ; this term will only be applied to the lower bound of uncertainty in y . The uncertainty in each dimension is affected by insertion length, and so will be summarized with respect to L in Table E.2 and Figure E.2. The greatest errors are in δ_x , due to the lack of a means to accurately measure or control Θ_z . To reduce spatial uncertainties in the future, steps should be taken to reduce δ_{Θ_z} .

The vertical air velocity measured with the pitot tube may be subject to some error due to the uncertainty in the pitot tube’s angle with respect to true vertical. This uncertainty can be estimated as

$$1 - \cos(\delta_{\Theta_y})\cos(\delta_{\Theta_z}) = 0.0024\%. \quad (\text{E.27})$$

Because of the very small magnitude of this uncertainty, it has been neglected in the error analysis of velocity measurements in Section E.3.

E.7 Water Flow Rate

The manufacturer of the turbine flowmeter rates its accuracy at $\pm 3\%$, but recommends field calibration of the value used to convert pulses per second to L/s. This field calibration was performed by measuring the change in level of the hot water tank as it drained, the feed pump transferring water from the hot water tank to the cooling tower to ultimately be collected in the sump tank.

First, the inside diameter of the hot water tank was determined with a measuring tape, yielding $D = 76.0$ cm with an estimated uncertainty of ± 0.5 cm due to positioning of the measuring tape and imperfections in the tank’s shape. The pump was switched on, and the globe valves were adjusted so as to deliver a flow rate of 1.0 L/s as reported Labview, which used the original factory pulses-to-litres factor. This reading wandered slightly as the level in the tank fluctuated over the course of the test, yielding 0.99 ± 0.04 L/s. Adding this drift to the $\pm 3\%$ accuracy associated with the flowmeter, the flow rate reported from the flowmeter

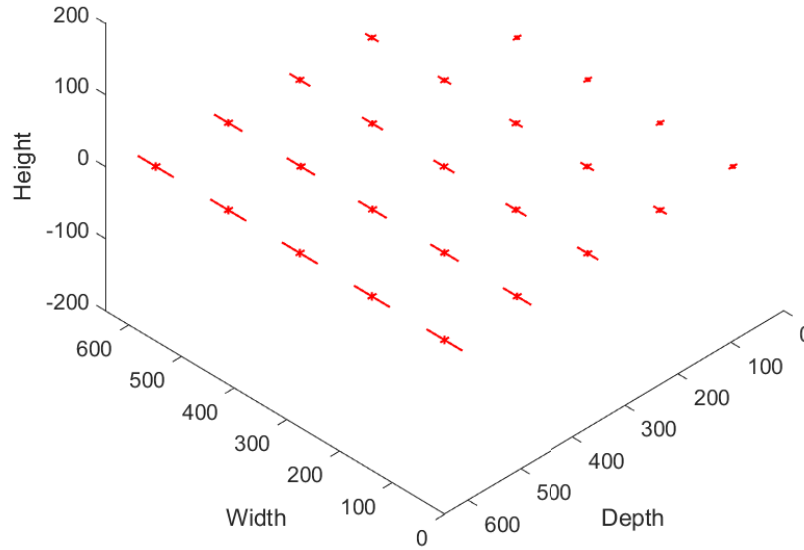


Figure E.2 – Uncertainty in spatial error for individual traverse points (mm)

could be given as 0.99 ± 0.07 L/s.

The outside wall of the hot water tank was marked at the water level as a stopwatch was started. After a period of time, the level in the hot water tank was marked again and the stopwatch stopped. The procedure was repeated five times.

The markings on the hot water tank are estimated to be correct within ± 0.5 cm due to the width of the marker, inaccuracies in drawing, and disturbance of the water level. Therefore, the difference in height between markings are accurate to ± 0.7 cm (square root of the squares of the error of each marking). The error in the stopwatch-recorded times is estimated to be ± 1 s due to lag between the drawing of the mark and the starting/stopping of the stopwatch.

With this information, the flow rate can be calculated from these manual measurements as follows:

$$\frac{\Delta \text{Volume}}{t} = \sum_{i=1}^5 \frac{\pi D^2 \Delta H_i}{4t_i N} = \frac{\pi(0.76)^2}{4(5)} \left(\frac{0.145}{70} + \frac{0.125}{67} + \frac{0.137}{68} + \frac{0.148}{72} + \frac{0.138}{69} \right) = 0.908 \text{ L/s.}$$

Before this result is judged against the turbine flowmeter's reading, the uncertainty in the

manual measurement must be estimated. This can be computed as:

$$\frac{\sigma_{\dot{v}}}{|\dot{v}|} = \sqrt{\left(\frac{\sigma_H}{\Delta H}\right)^2 + \left(\frac{2\sigma_D}{D}\right)^2 + \left(\frac{\sigma_t}{t}\right)^2}.$$

Therefore,

$$\sigma_{\dot{v}} = 0.908 \text{ L/s} \sqrt{\left(\frac{0.7}{13.9}\right)^2 + \left(\frac{2(0.5)}{76}\right)^2 + \left(\frac{1}{69}\right)^2} = 0.05 \text{ L/s}.$$

Comparing the flowmeter reading of 0.99 ± 0.07 L/s with the manually-measured value of 0.908 ± 0.05 L/s, the original flowmeter calibration is 9% too high. All water flow rates in the main body of this thesis have been adjusted to reflect this field calibration. Taking the square root of squares of the calibration error ($0.05/0.908$) and the innate sensor error (3%), these readings can be considered accurate to $\pm 6\%$ of reading.